Full-Color Holographic Near-Eye Displays

by

Seyedmahdi Kazempourradi

A Dissertation Submitted to the Graduate School
of Sciences and Engineering in Partial Fulfillment
of the Requirements for

the Degree of

Doctor of Philosophy

in

Electrical and Electronics Engineering

KOÇ ÜNİVERSİTESİ

January, 2021

Full-Color Holographic Near-Eye Displays

Koç University

Graduate School of Sciences and Engineering

This is to certify that I have examined this copy of a doctoral dissertation by

Seyedmahdi Kazempourradi

and have found that it is complete and satisfactory in all respects,
and that any and all revisions required by the final
examining committee have been made.

Committee Members:

____

Prof. Dr. Hakan Ürey (Advisor)

____

Asst. Prof. Mehmet Cengiz Onbaşlı

____

Asst. Prof. Fatih Toy

____

Assoc. Prof. Onur Ferhanoğlu

____

Assoc. Prof. Kaan Akşit

Date: ________________________________

To my beloved mother and the memory of my father.

ABSTRACT

Full-Color Holographic Near-Eye Displays

Seyedmahdi Kazempourradi

Doctor of Philosophy in Electrical and Electronics Engineering

January, 2021

Near-eye displays (NEDs) for augmented reality (AR) applications are expected to be the next computing paradigm. NEDs offer to combine computer-generated visuals with our physical world in a seamless fashion. Depth cues and natural blurring of images are all critical for a comfortable 3D experience with near-eye displays. Holography for NEDs is a commonly accepted strong candidate in meeting the human visual system's demands by offering natural depth cues. Holographic near-eye displays (HNEDs) deliver virtual images using computer-generated holograms (CGHs) displayed on spatial light modulators (SLMs). Holographic displays allow for a vast range of optical architectures that are not possible with conventional microdisplay-based designs. However, due to the current technological limitations of SLMs, most existing HNEDs have a limited field of view (FOV) and viewing region around the eye pupil (i.e., eyebox size). However, improving SLMs have a positive impact on improving FOV and eyebox size in HNED design.

In this thesis, we propose various solutions for overcoming the current technological limitations of SLMs and HNEDs. We start by offering a paraxial matrix optics-based analysis of a conventional HNED design to formulate the relation between eyebox, FOV, and SLM characteristics. We developed a CGH computation procedure that applies to arbitrary paraxial optical architectures, where the SLM illumination beam can be collimated, converging, or diverging. The virtual or real SLM image as seen by the eyebox plane may form at an arbitrary location. Using this approach, we designed full-color HNEDs with varying FOV and resolution characteristics and proper depth control.

We demonstrated a lensless HNED architecture with diverging beam illumination, which provides 3D images within a wide FOV (70°) at retinal resolution (30 cycles-per-degree), exceeding 4,000 resolvable pixels on a line. The experiments using binary holograms imprinted on masks prove that the proposed CGH computation procedure eliminates chromatic aberrations and speckle noise observed in all other laser-based displays. We also designed two systems with 10° and 20° FOV using dynamic SLM. While the first design has a uniform resolution, the second design demonstrates a foveated display, which has gradually degrading resolution across the FOV.

To further explore HNED architectures, we analyzed the light source coherence requirements and investigated HNED designs utilizing light-emitting diodes (LEDs). While laser light sources have the highest degree of spatial and temporal coherence, lasers' usage in

direct contact with a human may cause health hazards. We show that under certain design restrictions, it is possible to utilize LEDs instead of lasers and get better quality holographic images. We analyzed the effect of LED emission areas on image resolution, quality, and depth perception. Lastly, we designed micro-mirror array (MMA) based thin components and demonstrated that those could be used as off-axis thin lenses in AR displays to reduce size and volume.

ÖZETÇE

Göze Yakın Yerleştirilen Tam Renkli Holografik Ekranlar

Seyedmahdi Kazempourradi

Elektrik ve Elektronik Mühendisliği, Doktora

Ocak, 2021

Artırılmış gerçeklik (AR) teknolojisi, sürükleyici teknolojilerin bir sonraki dalgası olmak için merkezi bir rol üstlenmektedir. Başa takılan ekranlar (HWD), bilgisayar tarafından oluşturulmuş bilgiyi fiziksel dünya ile sorunsuz bir şekilde harmanlayabilme kapasitesi sayesinde AR ekranlarının gelişimi için harika bir adaydır. İmajların derinlik bulguları ve doğal bulanıklık etkileri, göze yakın yerleştirilen ekranlarda konforlu bir 3 boyutlu deneyim için önemli bir rol oynamaktadır. Hesaplamalı holografik ekranlar, doğal derinlik bulgularını ve görsel konforu sağlayan tek çözümdür. Göze yakın yerleştirilen holografik ekranlar (HNED); bilgisayarda oluşturulmuş hologramları (CGH), uzaysal ışık modülatörü (SLM) üzerinde göstererek sanal imajları kullanıcıya ulaştırır. Holografik ekranlar; geleneksel mikro ekranlar merkezli tasarımların yeterli olmadığı yerde çok geniş çaplı optik mimari seçeneklerini uygulanabilir kılmaktadır. Fakat; mevcut HNED tasarımları, SLM aygıtlarının teknolojik limitlerinden dolayı kısıtlı bir görüş alanı (FOV) ve göz bebeği çevresindeki küçük bir görüntüleme bölgesine (göz kutusu bölgesi) sahiptir.

Bu tezde; SLM ve HNED aygıtlarının mevcut teknolojik limitlerinin üstesinden gelecek çeşitli çözümler sunulmaktadır. İlk olarak, HNED aygıtlarının paraksiyal ABCD matris optik merkezli analizlerini gerçekleştirdik ve HNED mimarilerinin FOV ve göz kutusu bölgesini hesaplayacak formülleri geliştirdik. Bu sayede, paraksiyal optik mimarilere uygulanabilir bir CGH hesaplama prosedürü geliştirdik. Bu prosedürde; SLM aydınlatması (yakınsayan veya uzaksayan) paralel hale getirilebilir ve göz kutusu düzleminde görüntülenen SLM imajı istenilen pozisyonda oluşturulabilir, bu görüntü gerçek veya sanal olabilir. Bu yaklaşımı kullanarak; çeşitli FOV ve çözünürlük karakteristiklerine sahip, gerçek derinlik kontrolü olan ve tüm renkleri gösterebilen bir HNED tasarladık.

Bu tez kapsamında, 3 boyutlu imajları geniş FOV (70°), yüksek retinal çözünürlük (her derece için 30 döngü), bir çizgi üzerinde 4000 çözülebilir pikseli aşan, uzaksayan ışınlar ile aydınlatılan, lenssiz bir HNED mimarisi sunduk. Maskeler üzerine basılmış ikili hologramlar kullanılan deneylerimiz; CGH hesaplama prosedürünün, lazer tabanlı diğer ekranlarda görülen kromatik bozuklukları ve benek gürültüsünü ortadan kaldırdığını kanıtlamaktadır. Ayrıca 10° ve 20° FOV özelliklerine sahip, dinamik SLM kullanan iki farklı sistem tasarladık. Birinci sistem tekdüze çözünürlük sağlarken; ikinci sistem ise FOV bölgesi dahilinde aşamalı olarak çözünürlüğü azalan bir sistem sunmaktadır.

HNED mimarileri konusundaki keşiflerimizi bir adım daha öteye taşımak için; ışık

kaynağı tutarlılığı gereksinimlerini analiz ettik ve ışık yayan diyotlardan (LED) faydalanan HNED tasarımlarını inceledik. Lazer ışık kaynakları en yüksek derecede mekânsal ve zamansal tutarlılık sağlamasına rağmen; pahalıdır ve benek gibi istenmeyen yapılara eğilimlidir. Lazer yerine, bazı tasarım kısıtlamaları koşulları ile LED aygıtlarından faydalanılabileceğini ve daha yüksek kaliteli holografik imajlar elde edilebileceğini gösterdik. LED emisyonlarının imaj çözünürlüğü, kalite, derinlik algısı üzerindeki etkilerini analiz ettik. Son olarak, mikro ayna dizisi (MMA) tabanlı ince bileşenler tasarladık ve bunların AR ekranlarda boyutu ve hacmi düşürmek için eksen dışı ince lensler olarak kullanılabileceğini gösterdik.

ACKNOWLEDGMENTS

First and foremost, I would like to express my deepest gratitude to my supervisor, Prof. Dr. Hakan Ürey, for his endless support, encouragement, and patience during the past years. I greatly appreciate his comments and ideas, from which I have learned a lot. He has been the most inspirational person in my life.

I am indebted to Dr. Erdem Ulusoy, who provided me with his precious suggestions and creative ideas during my Ph.D. studies. I would also like to thank my colleagues in Optical Microsystems Laboratory and CY Vision company to have a vital role in my projects and make my past five years at Koç University a memorable episode of my life. I want to express my eternal gratitude to my parents for their everlasting love and support.

This work is supported by the European Research Council (ERC) under the Seventh Framework Programme (FP7/2007-2013) ERC advanced grant agreement (no. 340200), with acronym Wear3D. I gratefully acknowledge this support.

TABLE OF CONTENTS

LIST OF TABLES

LIST OF FIGURES

ABBREVIATIONS

2D: two dimensional

3D: three dimensional

VR: virtual reality

AR: augmented reality

MR: mixed reality

XR: extended reality

HWD: head-worn display

NED: near-eye display

HNED: holographic near-eye display

HMD: head-mounted display

FOV: field-of-view

VAC: vergence and accommodation conflict

CGH: computer-generated hologram

SLM: spatial light modulator

SBP: space-bandwidth-product

RGBD: Red, Green, Blue, and Depth

LUT: look-up table

NLUT: novel look-up table

FFT: fast Fourier transform

CG: computer graphics

DFT: discrete Fourier transform

IFTA: iterative Fourier transform algorithm

WDF: Wigner distribution function

MMA: micro-mirror array

HOE: holographic optical component

DOE: diffractive optical elements

PSF: point spread function

RMS: root mean square

LCOS: liquid crystal on silicon

CRT TV: cathode ray tube television

LCD: liquid crystal display

LED: light-emitting diode

OLED: organic light-emitting diode

AMOLED: active-matrix organic light-emitting diode

DLP: digital light processor

MEMS: micro-electro-mechanical system

LCA: lateral chromatic aberration

SAW: surface acoustic wave

Chapter 1

INTRODUCTION

1.1 Introduction to virtual and augmented reality

Virtual reality (VR) and augmented reality (AR) have played a central role in becoming the next wave of immersive technologies. Nonetheless, there is confusion about the differences between AR and VR [Jerald, 2016]. Both technologies can count as extended reality, where virtual environments are generated using computer graphic techniques. The user is immersed in the virtual environment with VR technology. However, AR is defined as an enhanced version of reality by using technology to overlay digital information and three-dimensional (3D) contents on top of the real world. The emergence of the AR/VR/smart-glasses boom in the early 2010s introduced new naming trends, more inclusive than AR or VR: mixed (or merged) reality (MR), more generally known today as "XR," a generic acronym for "extended reality." The name "smart eyewear" (world-locked audio, digital monocular display, and prescription eyewear) tends to replace the initial "smart glass" naming convention. Figure 1.1 represents the global XR spectrum continuum. It ranges from the real-world experience to augmented reality, where parts of the real-world are blocked through the occlusion, and digital information overlays the real world. In VR, users immerse themselves in a wholly digital world.

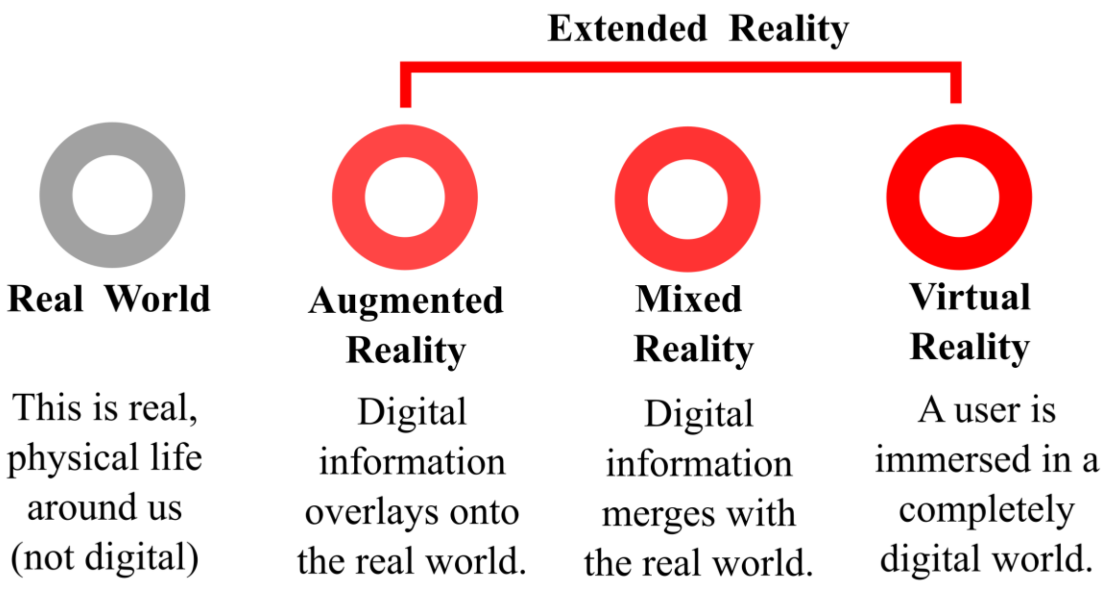

Figure 1.1 The terminology and differences of augmented, mixed, and virtual reality.

Stanley G. Weinbaum introduced the concept of VR, a science fiction writer, in his book Pygmalion's Spectacles dates back to the 1930s, as shown in Figure 1.2. He explains a game where the player wears a goggle to watch, touch, and smell the virtual stories' holographic recording.

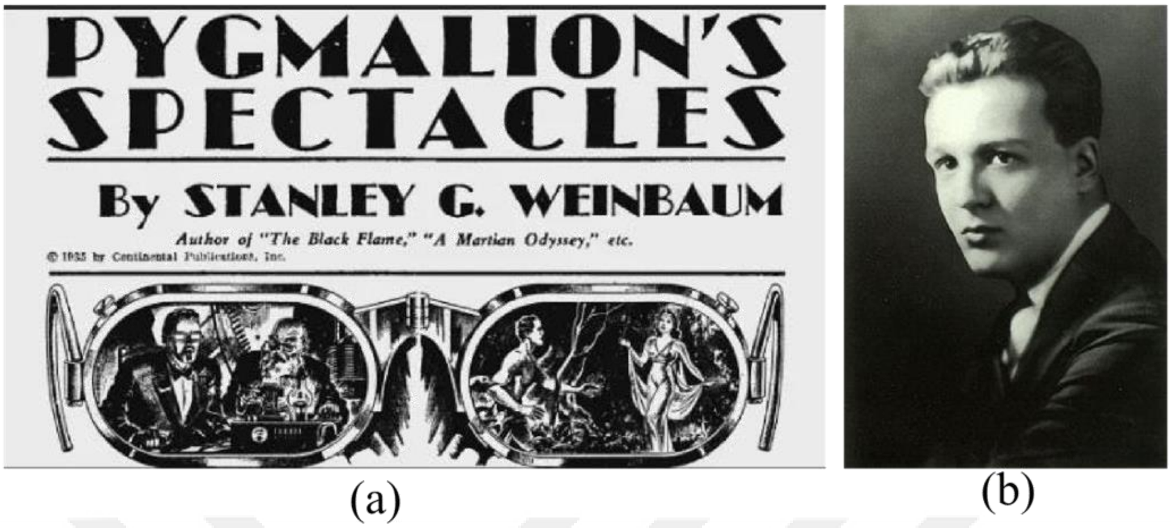

Figure 1.2 Pygmalion's Spectacles book cover (1930). (b)Stanley G. Weinbaum

As far back as the 1960s, the defense was the first AR and VR application market. American scientist Ivan Sutherland created the very first VR headset to be used with military applications. The photos of this headset can be seen in Figure 1.3. These tools are now a standard in the military and widely used for flight simulations.

Figure 1.3 Ivan Sutherland created the very first VR headset in the 1960s.

Based on such early developments, the first consumer AR/VR boom expanded in the early 1990s and considerably improved that decade. However, it was a technology ahead of its time and its markets [Barfield, 2015]. In other words, due to the lack of available cheap and consumer-level display technologies, a novel mixed reality display concepts were introduced throughout the 90s [Inzerillo, 2013; Azuma, 1997]. A state-of-the-art product was the "Virtual Boy" from Nintendo (1995), based on scanning displays instead of flat-panel displays. Figure 1.4 shows the virtual Boy from Nintendo, released with graphics in red and black in 1990 [Cakmakci and Rolland, 2006; Rolland and Cakmakci, 2009; Van Krevelen and Poelman, 2010].

(a) (b)

Figure 1.4 (a) The virtual Boy from Nintendo was released with graphics in red and black in 1995. (b) A screenshot of the graphics provided by the Nintendo device.

Although the mentioned display technologies were well ahead of their time, the lack of consumer-level inertial motion sensors, low-power 3D-rendering software and hardware, and high-speed wireless data transfer technologies contributed to the end this first VR boom. The other reason was the lack of digital content for enterprise or consumer spaces [Low et. al., 2003]. Today based on achievements in flat-panel display technologies, engineers invent novel immersive display technologies from scratch. Therefore, we have seen since 2012 the initial implementations of immersive AR/VR head-worn displays (HWDs) based on readily available smartphone display panels, pico-projector micro-display panels, and camera and depth map sensors. However, the immersive display experience in AR/VR is a paradigm shift from the traditional panel display experiences that have existed for more than half a century. The range is going from cathode ray tube televisions (CRT TVs) to liquid crystal display (LCD) and organic light-emitting diode (OLED) screens, to the liquid crystal on Silicon (LCoS), digital light processor (DLP), and micro-electro-mechanical system (MEMS) scanner digital projectors.

Scientists, academics, inventors, business managers, and AR/VR/MR system integrators, as well as enterprise users, expect to see a return on investment in XR technologies shortly, unlike in the former XR boom of the late 1990s.In 2014, Facebook acquired the Oculus VR system. In 2015, Oculus built partnerships with Samsung and began acquiring companies like Surreal Vision. This latest revolution in the VR industry provides a possibility for an average consumer to enjoy VR. Figure 1.5 shows the Oculus Rift series of products.

Figure 1.5 Oculus Rift series of products

After Oculus Rift, plenty of new VR devices are introduced to the market, and significant developments are made with applications, 360° cameras and cheap headsets. Today, consumers can experience VR apps with their smartphones and low-cost home devices like Google Cardboard. A variety of such low-cost and cheap devices are demonstrated in Figure 1.6.

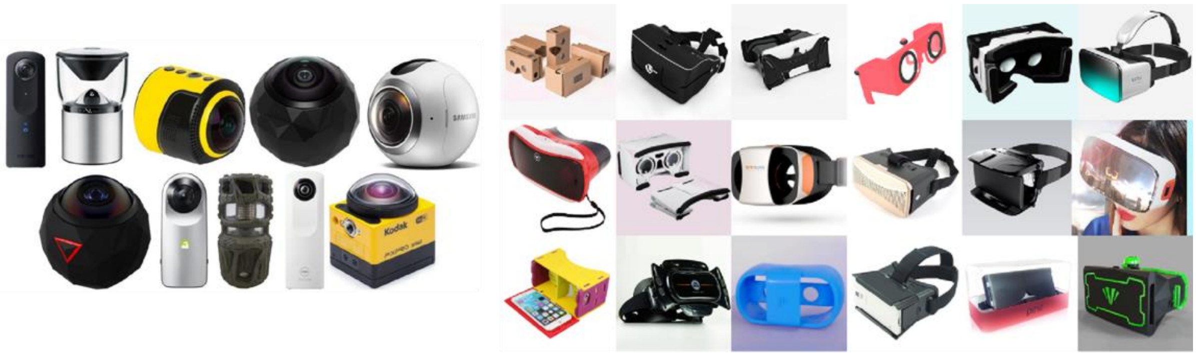

(a) (b)

Figure 1.6 (a) There are many 360 cameras introduced to the market. (b) Variety of extremely low-cost VR goggles that use a smartphone as a display.

The story of AR started in 1974 from a laboratory called the Videoplace founded by Myron Krueger. As shown in Figure 1.7, they combined projectors with video cameras that emitted interactive on-screen silhouettes.

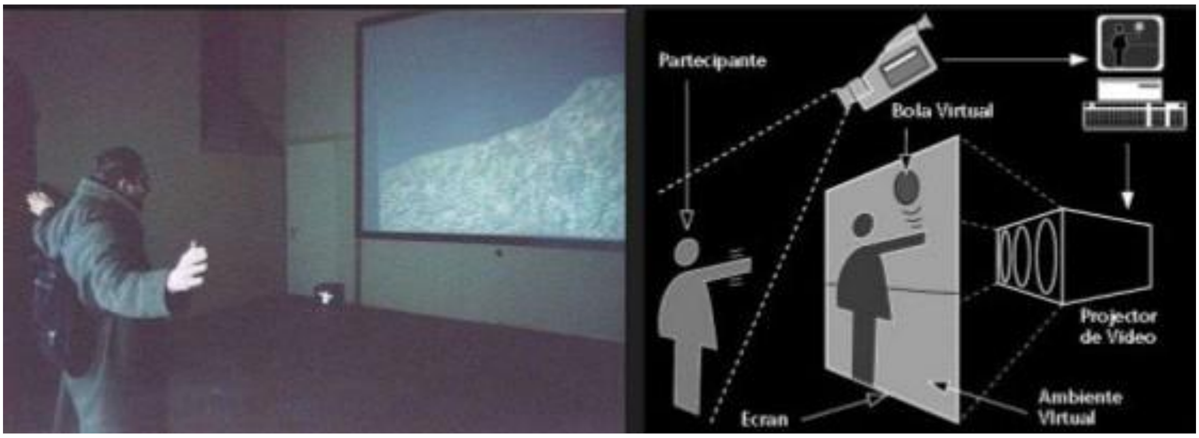

Figure 1.7 The story of AR started in 1974 from a laboratory called the Videoplace founded by Myron Krueger.

AR peaked in its hype from 2010–2015 when Google Glass was introduced and many other smart glasses. Figure 1.8 shows some of the AR headsets in the market till 2015. In 2014, Google announced the Google Glass device, Figure 1.8(a), for consumers, starting a wearable AR trend. A few years later, Microsoft Hololens version 1, Figure 1.8(b), and Meta AR, Figure 1.8(c), displays are introduced to the market.

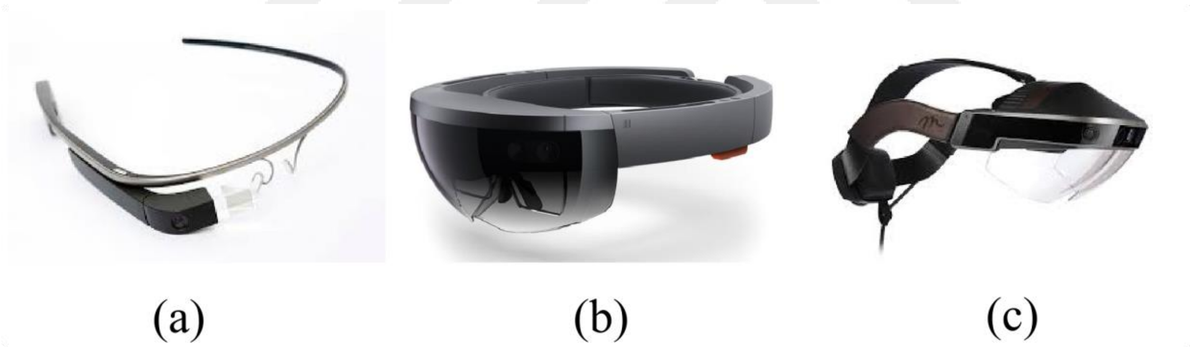

Figure 1.8 (a) Google Glass device, (b) Microsoft Hololens, (c) Meta AR

Investments in augmented reality are expected to reach 90 billion US dollars by 2020. Almost 50% of these investments aim at the hardware market, and many companies are funded to develop the next generation of AR/VR displays. In 2014, Magic Leap announced an AR investment of 50 million US dollars. A year later, the investment reached 700 million US dollars. Their long-awaited headset, Magic Leap One, was finally out in 2018 (cf. Figure 1.9). In 2017, the AR and VR investment records were broken as start-ups raised over 3 billion US dollars.

Evidence of an emerging smart glass/AR/MR user market is less apparent; hardware experiments have recently been investigated for smart glasses, including Google Glass, Snap Spectacles, Intel Vaunt, and North Focals. Despite the Oculus/Facebook VR and Sony Playstation VR products, VR headset improvements have also slowed a bit recently. The hyped

VR project at Google "DayDream" was restructured. Its hardware part dropped in October 2019, mainly because developers were not sufficiently enticed to develop quality apps for Google's Pixel phone series. We saw several medium-sized AR headset companies shut down in 2018, such as MetaVision Corp. (Meta2 MR headset), CastAR Corp., ODG Corp. (ODG R8 and R9 glasses). More recently, Daqri Corp., despite successful initial product introductions and good VC capital support with all four companies. Such companies were championing inspiring international AR shows, such as AWE (Augmented World Expo) from 2014–2018. Others, including Avegant Corp, went through a massive restructuring. Limited progress was seen by MetaVision and CastAR in mid-2019, showing that the sector is still volatile and full of surprises. Others (Vuzix Corp.) saw continuous growth during 2019 along with continuous VC support (Digilens Corp.) [Kress, 2020].

Figure 1.9 Magic Leap One and a view of the provided content

From 2018 on, as with many exciting technology cycles, extended reality starts to kick in as the market re-adjusts, many start-ups created during the euphoria period (2014-2018) close. New products are introduced specifically for the enterprise sector (Magic Leap One at $2,350, HoloLens V2 at $3,500, Google Glass V3 at $1,000, etc.).

A strong potential XR market relies on industries that can develop the required hardware and software. The development platforms and the software/cloud ecosystem to sustain a durable XR effort in the industry, providing a real return of interest for such industries. As a strong indicator of more prudent VC engagement, the latest investment round in Magic Leap (seeking $1.2B by the end of 2019) used the IP portfolio as collateral.

The exciting project Vaunt at Intel saw a renewal in 2018 (after the 2014 Google Glass failure in the consumer market) by providing small-form-factor smart glasses that included limited displays (around 10 degrees of FOV monocular) and prescription correction. Later that year, this project was stopped, as Intel instead invested in a very similar architecture, the Focals, built by North Inc., Canada. But the short-term future for consumer smart glasses remains unclear after a price drop of almost 50 percent in early 2019 and a significant layoff of North employees. North ended the production of its first Focal smart glasses in December 2019 and went through the second round of layoffs to develop its second-generation Focals smart glasses. This glass will provide a larger FOV and a larger eyebox size, based on a miniature laser scanner engine linked to a waveguide grating combiner. These smart glasses will be available in 2020. Another company, Bosch, unveiled at CES 2020 a similar monocular smart glass, based on a miniature MEMS laser scanner and a free-space holographic combiner. There has been slow but steady growth in other smart-glass concepts targeting enterprise sectors, including the rugged RealWear headsets (Vancouver, Canada) and the trendy Google Glass Enterprise V2 glasses. On the other hand, the latest VC investment speculation driving single start-ups like Magic Leap, Inc. (bringing the total of more than $3B VC investment pushing up a $7B company valuation before seeing any revenue) is a potent reminder of the ever-present' fear of missing out' actions of late-stage investors (Alibaba, Singapore Temasek, and Saudi funds) eager to get on the train driven by the early investment (Google ventures, Amazon, Qualcomm) [Kress, 2020].

It could take a significant consumer electronics corporation, regardless of the investment hype, to simultaneously build the ultimate consumer headset architecture (bringing up visual/wearable comfort and immersion experience) and the appropriate consumer demand. The consumer market relies entirely on the XR ecosystem's entire development, from generic hardware to generic content and applications, unlike the business market. Each enterprise delivers the content via the development of custom apps for particular needs. The smartphone revolution spurred the creation of successful developers in various parts of the world who organically created brand-new apps that took advantage of the phone form factor. Today, numerous small companies try to replicate such developments for AR and VR, with limited success.

During Q3 2018, we saw a worldwide decrease in both smartphone and tablet sales for the first time (indicating a 30 percent stock fallout from Apple in Q4 2018). XR consumer hardware can replace current smartphones or be the ultimate companion to a smartphone, offering an immersive experience out of competition for any other conventional display. For both consumer and enterprise users, the ultimate XR experience is defined along with two main factors: comfort (wearable, vestibular, visual, and social) and immersion (in all sensory directions). Three key characteristics are required for a convincing XR experience, considering comfort and immersion:

- Motion-to-photon latency below 10 ms via optimized fusion of sensors;
- Display locking through continuous depth mapping and semantic recognition in the 3D world; and
- Fast and consistent eye tracking.

Comfort in all aspects is key to enabling a large consumer acceptance when it comes to an XR headset. Some of the best exercises for better wearable and vestibular comfort are listed. An untethered headset with a small size, light-weight, center of gravity closer to that of a human head is desirable for comfort and the best mobility. Thermal and skin contact management throughout the entire headset is necessary. Visual comfort is an essential key for the mass adoption of XR. Large eyebox size is desired to allow for vast interpupillary distance (IPD) coverage. Optics can also come in various designs (i.e., small, medium, and large IPDs), but for enterprise, since the headset is shared between staff, it needs to fit a broad range of IPDs. A near 20/20 visual acuity angular resolution (at least 45 pixels per degree (PPD) in the central foveal region) is required, reducing to a few PPDs in the peripheral vision area. A high dynamic range (HDR) through high brightness and high contrast are also crucial for better visual comfort. Emissive displays such as MEMS scanners and OLEDs show different HDR behaviors than non-emissive displays such as LCOS and LCD. In an ultimate display, ghost images must be minimized. Providing an unconstrained 200+ degrees see-through peripheral vision is beneficial for outdoor activities, defense, and civil engineering. Display brightness control is also playing an important role to accommodate various environmental lightning conditions. Color accuracy and color uniformity over the FOV and eyebox (EB) are also important vision comfort keys. Vergence–accommodation conflict (VAC) mitigation for close objects located in the foveated cone through vergence tracking from differential eye-tracking data creates a comfortable user experience. Active pupil movement correction improves visual comfort for large-FOV optics. On the graphics side, an active pixel occlusion makes the displayed data more realistic. Social comfort features include no world-side image extraction (present in many waveguide combiners) and conversion of multiple-sensor objective cameras pointing to the world.

Immersion is the other key to the ultimate XR experience. Having an immersive FOV is a 3D concept that includes the z distance from the user's eyes, allowing for arm's-length display interaction through VAC mitigation. Immersive experiences come in various forms, including a foveated display. The foveated display is either static (foveated rendering) or dynamic (through display steering, mechanically or optically), a world-locked accurate spatial mapping, and accurate eye/gesture/brain-sensing using different sensors. The sensation of presence is created by immersion. However, several key factors must be addressed and solved in the HWD for a vivid sensation, not only in the display (refresh rate, FOV, angular resolution, VAC mitigation, occlusion, optical foveation, HDR, etc.) but also over the sensor fusion phase [Koulieris, et. al., 2019].

The optical design task must be considered a human-centric task to provide a display architecture with the ultimate XR comfort and immersion experience. This section identifies some of the specifics of the human vision system [Deering, 1998] and how they can be used to decrease the complexity of the optical hardware and software design without degrading the user's immersion and comfort experience in any way [Guirao et. al., 1999]. Thanks to its high cone density, the human fovea's resolution is maximum (covers just 2 to 3 degrees). The blind spot, where the optic nerve is located, is offset from the fovea's middle by around 18 degrees. Cone and rod densities differ around the retina, as seen in Figure 1.10.

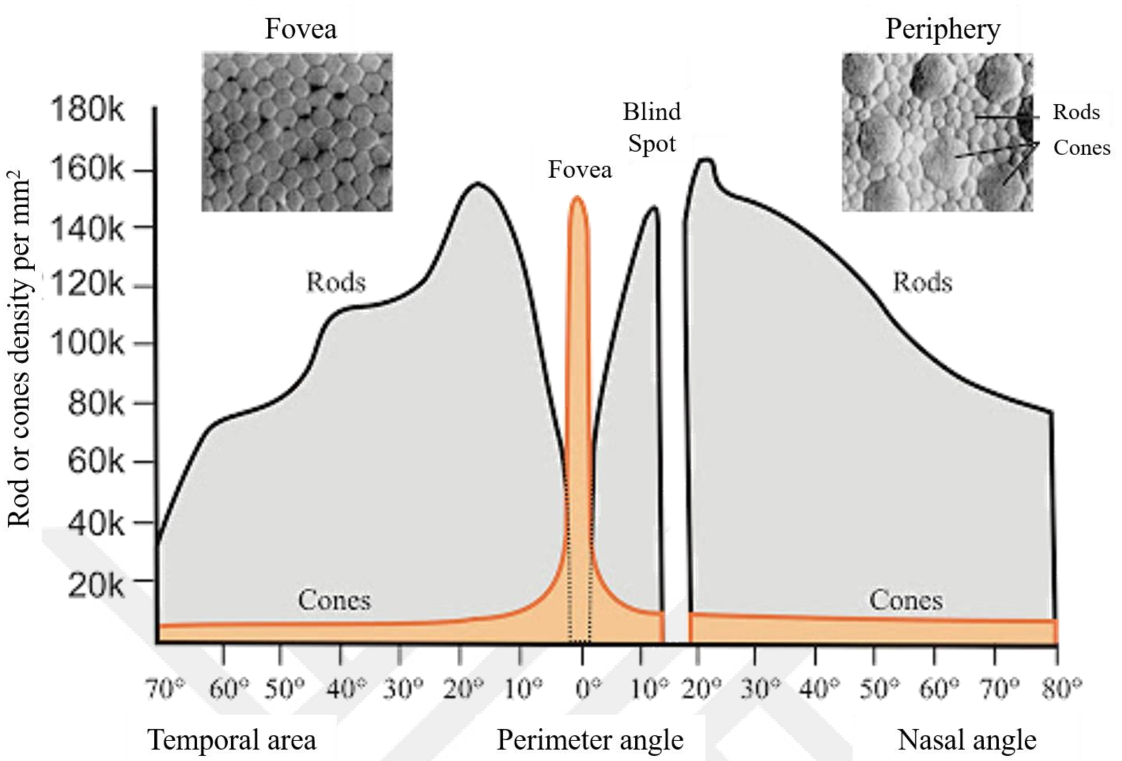

Figure 1.10 Rod and cone cell density on the retina. A microscopic view of cone and rod cells are provided as insets.

The optical axis (or pupillary axis, normal to the corneal vertex) is slightly offset by approximately 5 degrees from the line of sight [Meister, 2013] and agrees with the fovea's position on the retina, as shown in Figure 1.11.

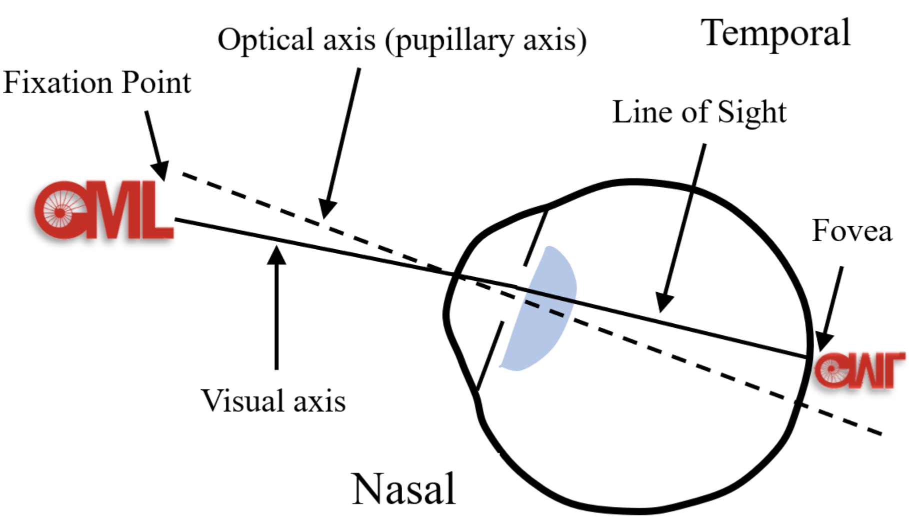

Figure 1.11 Optical axis and line of sight illustration.

Based on specific human visual behavior, the human fovea develops slowly in early life, and it is not a characteristic of our visual system at birth. Therefore, with novel visual habits that occurred during human evolution, the fovea's location could drift to new locations on the retina, such as the use of tiny digital displays carried by children at close range. Keeping digital panel screens too close to the eyes may cause early childhood myopia [Peli, 1998; Turnbull and Philips, 2017]. Chromatic aberrations result in color separation. The "L" in LCA Lateral chromatic aberration (LCA) causes different colors to focus at different depths. Reflective optics do not produce LCA and are therefore used extensively in AR display applications. Correcting chromatic aberrations and resulting artifacts such as color aliasing is a difficult task. Optical dispersion compensation is better, but it also requires more complex optics (e.g., more lenses or coupling architectures such as refractive optics with reflective optics. A method is developed for correcting LCA in holographic displays in this thesis. The proposed method is the equivalent of having three distortion map compensations, one for each color.

The ability of the eye to resolve small features is referred to as "visual acuity." The teenage and early-adult human eye can differentiate black and white alternating line patterns as tiny as one arcmin (30 cycles or per degree) [Navarro et. al., 1993]. The is the definition of the vision of 20/20. Stereo understanding is the difference in the two positions, converted into an angle of binocular disparity, or the difference in their binocular parallax. The vertical stereo disparity can be skewed when the AR or VR headset is tilted over the user's face or if one eye's display engine is misaligned to the other after a shock or a drop. Maintaining an excellent vertical stereo disparity within 3–5 mrad is often used as a rule in the AR/VR design field.

The horizontal extension of the human binocular vision system's various angular regions is shown in Figure 1.12. While the entire FOV is more than 220 degrees horizontally, in most situations, the binocular range is just 120 degrees (depending on the nose geometry). Stereopsis (the 3D depth cue provided by the left and right monocular vision fusion [Patterson and Earl, 2015]) is more restricted. It spans in a ± 40 degrees region, relative to fixation [Banks et. al., 2016], as shown in Figure 1.12.

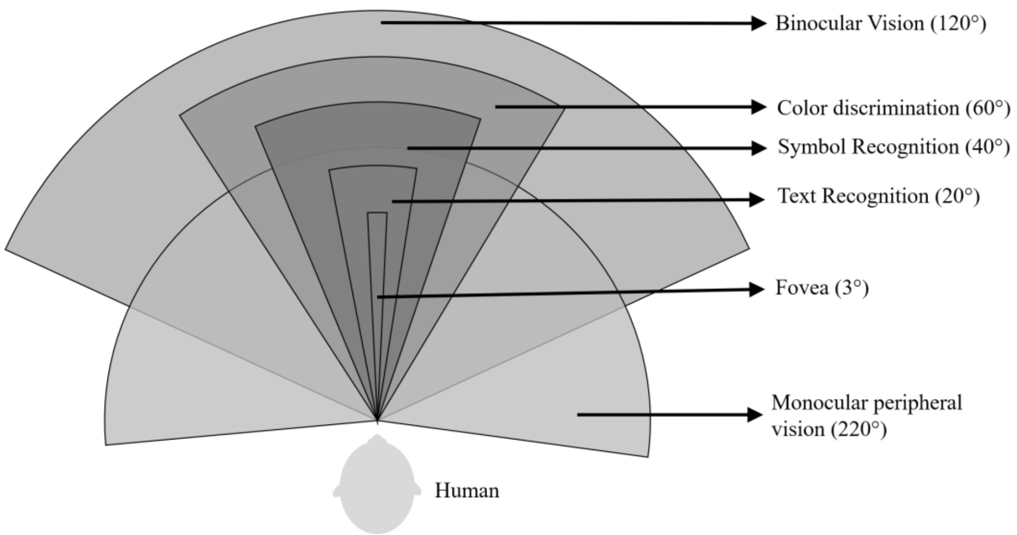

Figure 1.12 The horizontal FOV of the human eye

The vertical FOV is set off-axis from the horizontal line of sight, by about 15 degrees downward, as shown in Figure 1.13 as the relaxed line of sight. A relaxed head gaze would further lower that relaxed line of sight by about 10 degrees.

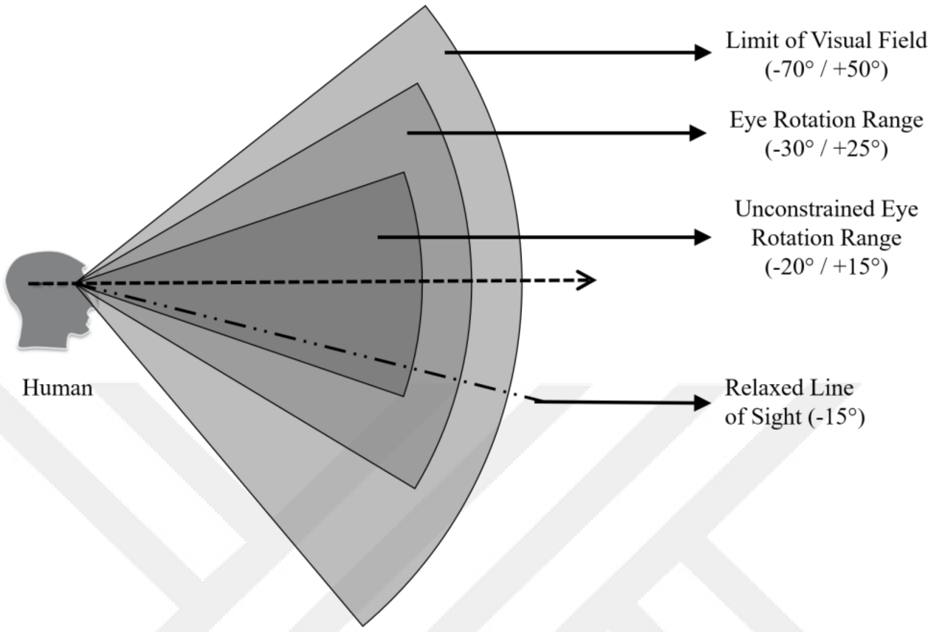

Figure 1.13 The vertical FOV of the human eye

The human FOV is a complicated concept, best defined when considering the limited and unrestricted ranges of eye motion [Meister, 2013]. Although the range of mechanical eye motion can be in the order of ±40 degrees horizontally, excluding the head-turning reflex, the unconstrained eye motion over which gaze is possible is much smaller and covers horizontal FOV of about ±20 degrees. The horizontal FOV area is about 40-45 degrees. For most current high-end AR/MR devices, the eye gaze defines the diagonal FOV. Besides, color recognition extends over ±60 degrees FOV, shape recognition over ±30 degrees, and text recognition over ±10 degrees for a given gaze angle. Standard VR headsets (including Oculus Rift 1, HTC Vive, Sony Playstation, Microsoft Windows MR) all have diagonal FOVs of about 110 degrees, expanding for some others to 200 degrees FOV (PiMax and StarVR). A large display panel combined with a large single curved free-space combiner (Meta2, DreamGlass, Mira AR, NorthStar Leap Motion AR) can produce large AR FOVs up to 90 degrees. Smaller-FOV high-end AR/MR systems can be created with micro-display panels, such as Microsoft HoloLens 1 and Magic Leap One. Usually, smart glasses have diagonal FOVs from 10 to 15 degrees (Zeiss Tooz smart glasses, Google Glass, North Focals) to more extensive FOVs beginning at 25 degrees, up to a 50-deg D-FOV (including Vuzix Blade, Digilens, Optinvent ORA, Lumus DK50, ODG R9) [Kress, 2020]. This thesis achieved a FOV of 70 degrees using a holographic display with a static binary hologram.

The FOV and resolution perceived by the human visual system is the bottom line for XR systems. In a human-centric system architecture, the resolution is a perceived specification rather than a scientifically measured specification. For instance, the perceived resolution on an immersive display can be doubled by duplicating the pixels on the actual display panel using the new iteration of the Samsung Odyssey Windows MR (2018 version) headset. The display pipeline renders and drives the display at 616 PPI, while 1233 PPI is seen in the resulting physical display. This case works for displays with uncoherent lights. In coherent-light-based displays (e.g., holographic display as discussed in the thesis), we demonstrated other methods to increase reconstructed holograms' resolution.

Perceived FOV range, especially in AR systems, can also be subjective. The display quality (resolution, absence of artifacts, reduced aliasing, and motion blur) leads to a perceived FOV larger than that of a comparable immersive display architecture. However, it would theoretically have lower image efficiency. A combination of the natural see-through FOV available and the virtual image's consistency defines the experience of the FOV by the user. Perceived color uniformity over the eyebox and the FOV is a combined left–right-eye effect in binocular devices. A monocular device might have random color uniformity issues (especially when using a grating or hologram waveguide combiner). A similar display built-in binocular headset will be perceived as having fewer color uniformity issues while having the same color uniformity issues as the monocular version. The factors and optical specifications driving the optical design cost functions include the eyebox, eye relief, FOV, brightness, angular resolution in the foveated region, and peripheral vision.

To fit a device to a variety of users covering a large population, it is critical to cover the 49-74 mm range of a population's IPDs. A large eyebox is necessary to achieve this result. The simplest definition of the eyebox is a 3D region located between the optical combiner and the eye. The entire FOV is visible for a typical pupil size [Harding and Rash, 2017]. The most specific criteria defining the eyebox is image vignetting (a sudden drop of image brightness at the edges of the FOV, clipping the image) [Barten, 2003].

For a given optical system, the eyebox is inversely proportional to the field of view. Therefore, the effective eyebox can be enlarged or reduced by simply lighting up a smaller or larger part of the available display panel. The eyebox that is perceived is also proportional to the pupil size of the user. The pupil size can be sensed as smaller in brighter environments or larger in darker environments (interior and with visor dimming).

Eye relief is usually the distance between the last surface of the combiner and the human eye pupil, which increases the effective eye relief by about 2 mm (given the 3-mm distance between the cornea and pupil in a medium of refractive index 1.33). Typical values of eye relief in XR headsets range from 13 mm to 25 mm. A more extended eye relief than 25 mm usually reduces the eyebox size to levels that provide less visual comfort.

In most XR architectures, the eyebox is usually a cone, with its most extensive section located right at the surface of the last optical surface. Therefore, the closer the user's eye can be to that optical surface, the better. Human ergonomics (eyelashes, eyebrows, forehead, nose, etc.) and prescription eyewear between the eye and the optics limits this distance to a minimum of 13– 14 mm.

The field of view (FOV) in an immersive display system is the angular range over which an image can be projected near or far-field [Wheelwright et. al., 2018]. It is measured in degrees. Usually, the FOV is given as a diagonal measurement of a rectangular aspect ratio image. For larger FOV values, the aspect ratio can become square or even circular or elliptical. The optical FOV can be larger than the experienced FOV if the eyebox is not wide enough.

The FOV is linearly proportional to the micro-display size and inversely proportional to the focal length of the collimation lens or collimation lens stack. Keeping the same FOV while reducing the micro-display for industrial design reasons requires the optical designer to increase the numerical aperture of the collimation optics, which increases their size and weight and introduces more aberrations, especially at the edges of the FOV. Therefore, a balance between micro-display size and lens power in the optical engine is needed to achieve the best performance. In holographic displays, the influence of the spatial light modulator parameters (instead of microdisplay) on the FOV is quite different from conventional displays. A detailed study is reported in this thesis.

The brightness is a crucial factor when it comes to designing an efficient AR optical system. The target luminance of the XR display must compete with the luminance of the surrounding world. For example, a 500-nits immersive display luminance would be acceptable inside a living room, but outdoor use would require more than 1,000 (up to 3,000 nits), whereas a jet fighter pilot's AR helmet would require over 10,000-nits display. On the VR side, 300–400 nits are usually sufficient. Luminous intensity (or luminance) is measured in nits [Kress, 2020].

In a decent XR system, the desired experience is to get the same resolution over the digital world, therefore expecting 20/20 vision over the entire FOV, which turns out to be about 0.3-arcmin resolution (or 195 PPD). A 1.3-arcmin angular resolution (relating to about 45 PPD) provides a decent XR experience for most people in their 20s to 30s. Even a modest resolution of 45 PPD (1.3 arcmins) stretched over a 110-degrees horizontal FOV would require a prohibitive number of pixels. Both foveation and peripheral display attempt to provide a large drop in the pixel count (while retaining a high angular resolution experience for the user.

Peripheral vision is a specific region of the human visual system in which flicker and aliasing effects are very critical, requiring a high refresh rate, low latency, and high persistence. To provide a high-resolution experience to the user while limiting the number of pixels in the display, one can use various foveation techniques [Hua and Liu, 2008; Ienaga et. al., 2001; Patney et. al., 2016; Chang et. al., 2020; Cem et. al., 2020], such as

- Static digital foveation without gaze tracking (same static display, fixed foveation is rendered over a central static 40-deg FOV cone).

- Gaze-contingent dynamic digital foveation (same static display, but high-resolution rendering is processed over a dynamic foveated region over a moving 15–20-deg FOV cone).

- Gaze-contingent dynamic optical foveation (uses two different display systems: a static low-resolution, high-FOV display over 60+ deg, combined with a dynamically steerable high-resolution, low-FOV display over about a 15–20-deg FOV cone—the displays can be either fixed or gaze-contingent— using a steering mechanism).

Optical foveation based on gaze also requires subsequent mechanical (mirror) or phased array steering of the high-resolution display within the low-resolution display FOV [Kim et. al., 2020; Akşit et. al., 2019]. Varjo (Finland) uses a gaze-tracker based mechanical system. Eyeway-Vision (Israel) uses both low- and high-resolution MEMS laser-scanner display systems low-resolution scanning system can be steered to follow the gaze direction.

1.2 Near-eye displays

Near-eye displays (NEDs, also referred to as head-mounted or head-worn displays) have promised an incredible experience of human-computer interaction with quite exciting applications of augmented and virtual reality since their introduction in the early 1960s. None of the available NEDs managed to overcome several fundamental limitations and fulfill the expectations until today. NEDs present two-dimensional (2D) or 3D virtual objects or scenes exclusively to a user's eyes, providing a light, efficient, immersible, and personalized experience.

Designing AR headsets is a more difficult task compared to the design of VR headsets. The display engine is the main optical building block of the display architecture of any HWD. The task of the display engine is, therefore, threefold. It must produce the desired image, provide an exit pupil, and shape this exit pupil to the aspect ratio required by the pupil expansion scheme to create the desired eyebox. Therefore, the optical display engine's design needs to be done as global system optimization and the combiner's design, primarily when a waveguide combiner is used. Display engines are usually formed around three distinct building blocks:

1. The illumination engine (for non-emissive display panels),
2. The display panel (e.g., micro-display or spatial light modulator) or scanner, and
3. The relay optics (or imaging optics) form the exit pupil for the combiner optics.

The display engines can be divided into two main branches: panel-based and scanner-based display engines.

There are two types of panel display systems available for VR and AR systems today: direct-view panels and micro-display panels. The direct-view panels are used in smartphone systems and range in size from 3.5–5.5" and in resolution from 500–850 DPI. Micro-display panels, such as LCD micro-panels and silicon-backplane-based liquid crystal on silicon (LCoS), micro- active-matrix organic light-emitting diode (mu-AMOLED), or light-emitting diode (LED) panels, and Digital Light Processing (DLP) MEMS panels come in sizes from 0.2–1.0". Polarization and emission cones are also essential features of any micro-display-panel system. The panel's speed is also an important feature, especially when the display needs to be driven at higher refresh rates to provide added functionality, such as in multi-focal-plane displays. DLP is the fastest display available (used in the Avegant multi-focus AR HWD).

The LED arrays on Silicon backplanes have gained a lot of attention because of their high brightness, high efficiency, high reliability, and small pixels. LED arrays have been used in various wearable products such as smartwatches (LuxVue acquisition by Apple in 2014) or AR devices (InfiniLed Acquisition by Facebook/Oculus in 2015, a $15M Google investment in Glo Inc. in 2016, as well as in Mojo-Vision in 2019, and a $45M Intel Capital investment in Aledia SaRL in 2017).

Almost all existing NEDs are designed as standard incoherent imaging systems. For each eye, a flat panel microdisplay is deployed, and the visual information is presented in the form of regular 2D images, mostly corresponding to perspective 2D views. This approach leads to two fundamental limitations: relay optics and visual fatigue problems. The problem with relay optics arises from the fact that human eyes cannot focus directly on a near-to-eye microdisplay, as their near-point is about 25 cm. Optical conjugation of the microdisplay to the retina implies additional optical components. Microdisplay-based NEDs ultimately require a balance in FOV, resolution, and form factor. The visual fatigue limitation comes from the fact that microdisplay-based NEDs can support only stereoscopic 3D. It is well known that stereoscopic systems have a fixed distance of focus and therefore cause visual discomfort, caused by the conflict between the responses of the accommodation (change of focal length of the eye lens) and convergence (rotation of the eyeballs towards a viewed object) [Urey et. al., 2011]. Integral imaging or NEDs based on pinhole have decreased discomfort significantly but at the expense of resolution loss [Hua and Javidi, 2015]. Shifting the microdisplays back and forth or using variable focal length lenses in time-multiplexed schemes are some solutions forming a multitude of focus distances and are limited to small FOVs only [Liu and Hua, 2009]. Light field, or integral imaging-based NEDs that use micro-lens or pinhole arrays as relay elements. NEDs that use directional backlights have small size and broader FOV, and substantially lower resolution [Hua and Javidi, 2014; Maimone et. al., 2014; 2013, Maimone and Fuchs]. Scanning display engines are implemented in various HMD systems today. Such systems' main advantages are their small size (not limited explicitly by the etendue law since there is no object plane as in display panels), high brightness, high efficiency with laser illumination, and high contrast. Note that miniature cathode ray tube (CRT) display units (which are also technically scanners) were used for early VR and AR systems (e.g., Sword of Damocles, 1968). 2D MEMS laser/VCSEL scanners (Intel Vaunt, Focals by North, Hololens v2) dramatically reduce the optical engine's size [Baran, 2012]. Yet other scanning technologies have also been investigated, such as fiber scanners [Schowengerdt et. al., 2010; Khayatzadeh et. al., 2018], integrated electro-optic scanners, acousto-optical modulators (AOMs), phase array beam steerers, and surface acoustic wave (SAW) scanners [Jolly et. al., 2017].

Most scanner-based optical engines lack exit pupil size (small eyebox) and therefore need complex optical architectures to extend/replicate or steer the exit pupil to the user's eye. A few such architectures for MEMS scanning displays are used in recent products like Intel Vaunt, North by Focals, and HoloLens V2 by Microsoft.

1.3 Holographic near-eye displays principles

Dynamic holographic displays promised the delivery of 3D images with natural depth cues based on the introduction of computer-generated holograms (CGHs) in the late 1960s and the current progress in spatial light modulator (SLM) technologies [Kang and Onural, 2010].

Laser-based phase panel display engines have been recently applied to the design of interesting holographic HWD architectures prototypes that can provide a per-pixel depth display and effectively solving the VAC. [Zschau et. al., 2010, Maimone et. al., 2017, Kazempourradi et. al. 2019] Phase panels can come in many forms, from LCoS platforms (HoloEye, Jasper, Himax, etc.) and ferroelectric LCOS platforms [Banks, 2006] to MEMS pillar platforms (Texas Instruments). Diffractive panels usually operate in color-sequential mode. The phase difference required for a substantial local destructive interference (or a phase shift) is strongly dependent on the reconstruction wavelength, much more than for a traditional amplitude LCoS panel. A phase panel must have a few specifications that differ from traditional amplitude LCoS panels to generate high efficiency and a high-contrast image:

- Accurate phase levels are required, matching the laser wavelengths in color sequence.
- Analog drive is preferred since a digital drive with pulse width modulation (PWM) can produce parasitic orders.
- A low number of bit depth is enough (such as 1, 2, 3, or 4 bits— amplitude panels usually have a minimum 8-bit modulation depth) since 16 phase levels are enough to generate 99% efficiency, theoretically.
- A small pixel size is necessary to allow for a large diffraction angle (and thus a large FOV).
- A minimal pixel interspacing will limit parasitic diffractions.

A holographic display generates and demonstrates a portion of the wave field that would emanate from the displayed 3D objects instead of stereoscopic displays with 2D perspective images. As a consequence, 3D objects with natural depth cues are seen by viewers. The VAC is omitted because audiences no longer concentrate on the display screen but rather on the viewed 3D object itself. Most of the holographic display schemes proposed have a table-top television-like design and attempt to synthesize mid-air floating ghost-like 3D objects around which many users can move and rotate [Yaras et. al., 2009; Yaras et. al., 2011; Sasaki et. al., 2014]. While this idea is exciting, it is very complicated as well. In particular, such systems require large-area SLMs with micron-level pixel pitches, which correspond with large space-bandwidth product (SBP) constraints that are far from being met by the current state of SLM technology [Kang and Onural, 2010]. Not surprisingly, demos are limited to very tiny 3D models and small viewing areas, with no evidence of any noticeable short-term progress. The use of eye-tracking suggested by SeeReal Inc. to alleviate space-bandwidth-product (SBP) requirements is a great solution [Haussler and Leister, 2008]. The solution from SeaReal does not deliver the object waves within a large viewing area but simply provides the object wave within two tiny windows conjugated to and steered with the viewer's eyes. This way, the holographic display's spatial bandwidth requirement is significantly reduced. However, a broad panel SLM dedicated to a single user is still needed for this solution. Another complication is tracking the viewer's eyes through cameras located on the distant display screen, which is about the user's length of an arm. Moreover, before the display has to be rotated or interpreted, the device enables user movement only within a restricted space [Kuo et. al., 2020].

As the two realms are unified as HNEDs, the fundamental limitations associated with NEDs and holographic displays are significantly alleviated. This method has been largely neglected until recently, except for a few efforts that do not seem to acknowledge the potential benefits fully. A holographic head-mounted display with RGB light-emitting diode light source is explored in [Moon et. al., 2014], where the findings do not include a full-color reconstruction free of speckle noise. A bar-type HNED is recorded in [Yeom et. al., 2015] using two holographic optical elements with a small FOV. A full-color HNED concept is published by Microsoft, in which random phase assignment on virtual object points adds speckle noise to the reconstructed holograms [Maimone and Kollin, 2017, Park, 2017]. In Figure 1.14, the advantages of HNEDs are represented by the creative illustration of the ultimate augmented HNED we imagine. Its relatively simple optical design consists of a point light source that illuminates an SLM mounted directly in front of the eye. The HNED has a relatively thin form factor. The illustrated HNED uses no optical relay and can provide a wide FOV, despite this simplicity. Besides, the HNED offers natural accommodation cues thanks to its holographic nature, as demonstrated by the given retinal images where a virtual text object appears in or out of focus together with the actual object on which it is augmented. The HNED is also very versatile in providing additional features, such as presenting the always-in-focus virtual object reading “Istanbul Tour” with no hardware modification.

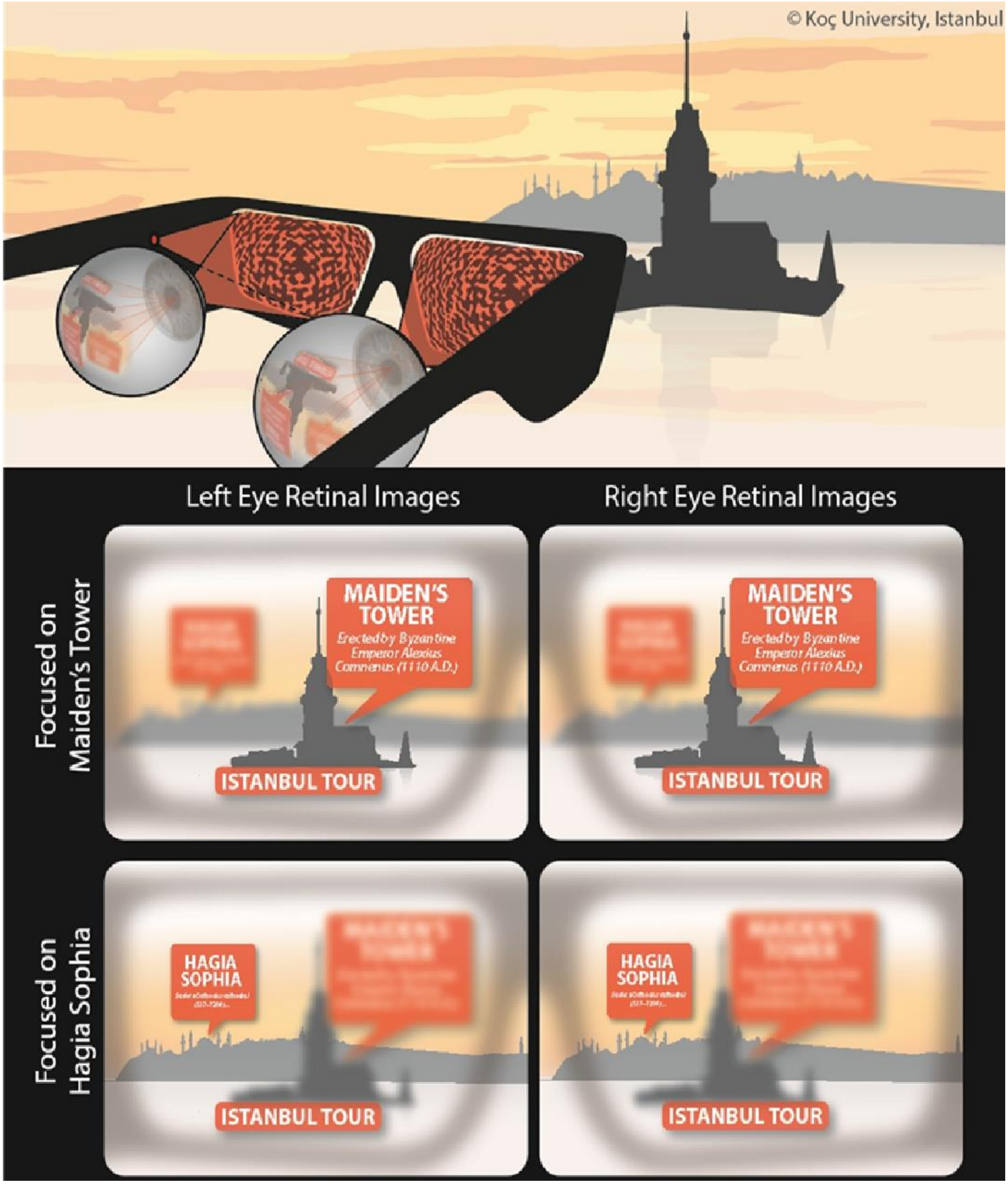

Figure 1.14 Artistic interpretation of HNED, as the ultimate augmented reality solution is provided. The scene depicts the Maiden’s Tower and Hagia Sophia, respectively, as actual nearby and far objects. Through the CGHs displayed on the reflective and semi-transparent SLMs, the HNED is intended to be in the shape of an eyeglass and shows virtual objects on top of the real-world view. The HNED is illuminated by the point light sources positioned on either side. Insets display the images created on the user’s retinas. Along with the corresponding real objects, two of the virtual objects (large text boxes) appear in or out of focus, while the virtual object reading “Istanbul Tour” is always in focus. The eyeglass frame always appears out of focus as expected. (Illustrated by Çaglar Genç, Design Lab, Koç University).

The primary operational concepts outlined in Figure 1.15 justify the probability of achieving the HNED in Figure 1.14. The point light source generates a narrowband, spatially coherent diverging wave that illuminates a reflective and semi-transparent SLM. Notice that there are still no transparent SLMs with sufficiently small pixel sizes on the market. The SLM functions as an optical mask under the correctly computed CGH loaded on it, converting the illumination wave directly into the true light wave that would emanate from the virtual objects as they reside at their apparent positions. This latest wave goes through the eye's pupil, along with the wave emerging from the real objects, and forms an image on the retina. Because the wave produced by the SLM is already formed to have the correct ray angles, without requiring the support of relay lenses, the eye can quickly form a focused image. The correct ray angles, therefore, contribute to the correct accommodation cues. Hence, the visual fatigue inherent in all stereoscopic displays is removed. Virtual objects whose waves are distributed within the whole eyebox (assumed to encapsulate the eye pupil completely) are viewed at the retinal resolution. Always-in-focus objects can be seen using a smaller portion (around 1 mm) of the eye pupil. A separate point light source should be switched on and off for each color channel in a time-sequential manner for full-color applications, and the CGH on the SLM should be changed in synchronism. Similarly, functionality such as compensation for users' visual disabilities can be offered by simple modifications to the displayed CGHs without manipulating the hardware.

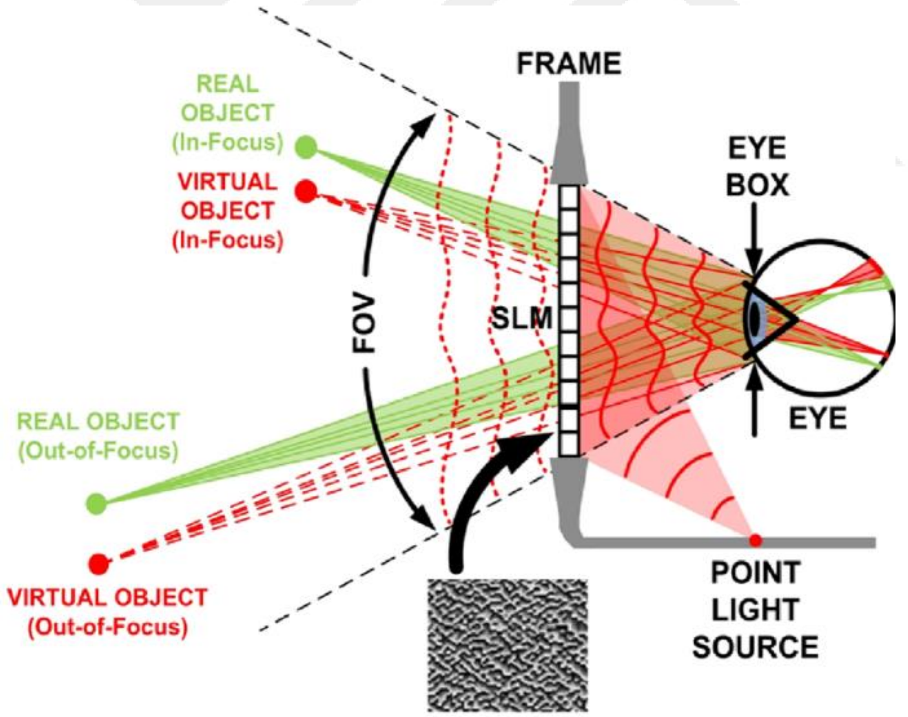

Figure 1.15 Schematic top view of the left eye of a person wearing the HNED. The CGH on the SLM explicitly translates the diverging wave from the point light source to the correct waveform (with proper ray angles) from virtual objects. The wave passes through the eye's pupil and the light from real objects and creates a retinal image. The eye is focused on nearby objects in the figure.

Figure 1.15 shows a cost-effective and straightforward implementation in terms of hardware from the viewpoint of holographic displays. The display's near-eye character minimizes the SLM size needed for a given FOV. By reducing the monitor's eyebox size down to the user's eye pupil size and using pupil trackers to handle the eye movements, the SLM's space-bandwidth constraint can be reduced. The amount of visual information the display offers at a time. Therefore the SLM's SBP requirement is reduced in this manner. Compared to a distant-to-eye display, the pupil trackers can be integrated in a much simpler way through cheap miniaturized cameras and infrared light sources on a head-mounted system. The system's computational complexity is increased by the trackers and related content update procedures, but this is easier to manage with a dramatically reduced hardware cost. For many decades, static holograms have been developed and used for different applications, such as structured lighting for depth cameras (Kinect 360 (2009) and iPhone X (2018)) or as engineered diffusers; custom pattern projectors such as the interface projector of the virtual keyboard (Canesta 2002 and Celluon 2006); or more common laser pointer pattern projectors.

In most conventional NED systems, the visual information emanates from flat-panel microdisplays. They are either self-emissive or illuminated with diffuse backlights. Flat-panel microdisplays comprise an incoherent array of pixels that pass through a relay optics module (ROM). ROM is placed between the microdisplay and the user's eye. The fact that a human eye does not focus on a microdisplay near the eye necessitates utilizing ROM since the near focal point of human eyes is 25 cm. The design of ROM involves inevitable compromises among FOV, image quality, and form factor. The ROM essentially forms a virtual image of the microdisplay at some distance between 25 cm to infinity, at which the user can focus. Equivalently, the relay optics system supplements the human eye's refractive power, and the microdisplay and the retina become optical conjugates. The conjugation between the microdisplay and retina is mandatory since the only way of representing visual information on a microdisplay is through possibly distorted perspective images of a virtual scene. Each pixel of a virtual scene can only be represented by a single pixel of a microdisplay. An extended microdisplay area cannot represent a virtual scene pixel because microdisplay pixels are incoherent. Visual discomfort, including headaches, eye strain, and motion sickness associated with conventional stereoscopic NEDs, create a less than desirable viewing experience. Matching the vergence and accommodation, depth cues, and natural blurring of images is essential for a comfortable 3D experience with NEDs. Computational holographic near-eye displays (HNEDs) are the only solution that can provide all the natural depth cues and visual comfort [Kang and Onural 2010, Kazempourradi et. al., 2019; Cem et. al., 2020].

In comparison, coherent-light-based HNED systems, where CGHs represent visual information loaded on SLMs, provide great optical design flexibility. In HNEDs, each virtual scene pixel is represented by its hologram, which may be distributed over an extended area of the SLM, covering many coherently interacting pixels. The individual hologram creates a wavefront, which (after possibly tracing some subsequent optical components) appears to the eye as the wavefront emanating from the corresponding virtual scene pixel. As a result, in HNEDs, several unique advantages in terms of optical design are present. First, deploying a relay optics system between the SLM and eye is not fundamentally necessary. An SLM can be placed directly in front of the eye. Optics between SLM and eye may only be used to tackle some current technological challenges of SLMs if desired. Second, SLM does not need to be conjugated to the retina (or a particular virtual object plane). Third, if used, the relay optics do not need to have an excellent aberration performance since aberration correction can be partly softly performed via CGHs. In this way, no compromise is fundamentally needed among FOV, image quality, and form factor. The computational nature of HNEDs provides excellent flexibility in optical design. It enables a vast range of optical architectures with different properties, impossible for conventional micro-display-based NED designs. This potential of HNEDs, which we believe is not fully understood and appreciated, is undertaken in this thesis through simple paraxial matrix optics formalism. We define the generic HNED architecture, which consists of a light source plane, an SLM plane, an eye plane, and paraxial optical systems - described by ABCD parameters - sandwiched in between.

We developed a simple paraxial ABCD matrix optics-based method for designing holographic displays and show that FOV and eyebox size limitations of HNEDs can be extended beyond what has been reported in the literature. The limited bandwidth of the SLM imposes a meaningful trade-off relationship between FOV and eyebox size. The display's near-eye character minimizes the SLM size needed for a given FOV. By reducing the display's eyebox size to the size of the user's pupil size, the SLM's SBP constraint can be reduced. The area under the FOV and the eyebox size curve is constant [Brooker and Brooker, 2003], determined by the SLM's size and pixel pitch. Several researchers have studied the bandwidth limitations of holographic displays. The Wigner distribution function (WDF) is a transform that can represent the optical signal's angular and spatial boundaries, making it a useful tool for analyzing the bandwidth of the holographic displays [Lohmann et. al., 1996; Testorf and Lohmann, 2008]. The WDF is recently used to analyze the resolution and degrees-of-freedom of the holographic displays [Gao et. al., 2017; Jang et. al., 2018]. The FOV of an HNED followed by a condition on the size of the eyebox using matrix-optics analysis is determined, which results in a fundamental relation between the product of the FOV and effective eyebox size.

In a generic HNED, the optical system placed between the point light source plane and the SLM plane is named the illumination module, and the optical system placed between the SLM plane and eye plane is named the eyepiece module. In this thesis, we restrict our attention to paraxial systems. Therefore, the illumination and eyepiece modules are represented by ABCD parameters. Note that any or both modules can merely be some free-space section (a free-space section with thickness d) represented with parameters (A = 1, B = d, C = 0, D = 1)). Regarding the illumination module, the only restriction we impose is that we avoid imaging the point light source on the SLM plane. We want the entire SLM to get illuminated.

Commercial SLMs modulate either the phase or the amplitude of the complex-valued CGHs. However, the complex modulation of light is desired to transform the incoming wave to a wavefront indistinguishable from the wavefronts emanating from real objects. Hence, additional encoding steps are required to convert a full-complex CGH to a phase-only, amplitude-only, or binary CGH. Conversion of full-complex CGH to a modulated CGH can be performed using direct binary search, error diffusion, or iterative Fourier transform algorithm (IFTA) procedures [Mori et. al., 2014; Takaki and Yokouchi, 2011; Deng and Chu, 2017]. However, almost all of these algorithms have an iterative structure and have repetitive fast Fourier transformation (FFT) or pixel-by-pixel processing operations that require high computational complexity. A non-iterative algorithm uses straightforward discrete Fourier transform (DFT) relations to calculate phase CGHs presented in [Mengu et. al., 2016] by precisely controlling half of the necessary image samples through a single FFT. Alternatively, for complex modulation, a pair of SLMs or a grating is used in the literature [Wyrowski and Bryngdahl, 1988].

Holographic displays are coherent systems of light processing where visual information is fed by CGHs presented on SLMs, and wavefronts are synthesized and indistinguishable from those emanated by physical objects. In [Park, 2017], a study of recent progress in computer-generated holography is provided. CGH computation methods can be categorized by the manner they express 3D objects. In wave-propagation-based methods, objects are represented by point clouds or polygons. In contrast, in ray-tracing-based methods, the 3D model is represented with RGB-Depth (RGBD) or multi-view images.

Objects are represented by a series of self-emitting point sources (the point-based model) or polygons in wave-propagation methods (mesh model). By superposing the individual wave fields of primitive structures, the optical wave field of a 3D scene is reconstructed. The diffusive or specular reflection of each surface of the 3D object is uniform. Therefore, an immense number of points, usually in millions of scales, must be sampled by the object. Wave-propagation techniques typically suffer from two key problems: the high computational expense of superimposing object point wavefields at each pixel of a CGH, and the problem of occlusion, i.e., occluded primitives of a scene should be defined at each point of view, and their contributions should be removed. Hidden surfaces become apparent if the above computation is skipped and the entire scene becomes transparent in an unrealistic way. The first look-up table (LUT) approach was proposed by [Lucente, 1993]. A set of elementary fringe patterns of uniform sampled points in 3D image space are pre-computed and stored in a memory to enhance the point cloud method's computational performance. Although the CGH computation is accelerated successfully by the LUT, a large memory allocation is required. Many novel LUT (NLUT) methods have recently reduced this large memory requirement [Kim and Kim, 2008, Kim et. al., 2012]. CGH estimates based on recurrence-relation were also proposed in [Matsushima and Takai, 2000; Yoshikawa, 2001; Shimobaba et. al., 2002]. These approaches are well-suited to applying hardware acceleration [Shimobaba et. al., 2002]. The dense sampling on the 3D object as well as on the hologram plane affects point-based methods. Polygon-based approaches were proposed as a solution instead of point-based methods, where polygons, typically triangles, represent the 3D object. The incorporation of texture and shading algorithms from computer graphics into polygon methods is also relatively simple. Matsushima summarized the conventional method's entire formulation and evaluated the effect of various approaches to interpolation [Matsushima et. al., 2003] and examined texture, shade [Matsushima, 2005], and specular reflection in surface rendering. An original triangle is represented in its local coordinates for each arbitrary polygon. Then, to get a local spectrum of the triangle, a simple Fourier transform (FFT) is performed. The arbitrary polygon's global spectrum is obtained by remapping the spectrum to global coordinates implemented by 2D interpolation. To measure the diffraction pattern on the hologram plane, a 2D shift and angular spectrum propagation are performed. Several methods were proposed to shorten the original polygon's depicting procedure, the FFT computation, and the 2D interpolation. A complete analytical polygon-based approach was proposed by Kim and Ahrenberg, where a primitive polygon and its spectrum are analytically obtained. By considering the 3D rotational transformation, 2D origin shift, and the angular spectrum propagation as an integrated phase, the spectrum's value at each frequency point of the diffracted wave is analytically derived [Ahrenberg et. al., 2008; Kim et. al., 2008]. Using Fraunhofer diffraction to reflect waves in the Fresnel region, Liu reported a complete analysis method [Liu, 2011]. Polygon-based approaches are preferable compared to point methods with less sampling quantity. The FFT and 2D interpolation, however, are robust processes of computation. While several improved polygon methods were suggested, they either sacrificed texture or brought additional computation. So far, no real-time polygon-based method has existed [Pan, 2016]. In ray-tracing-based methods, CGHs are computed by processing 3D scenes with computer graphics methods. For each viewpoint, computer graphics techniques are utilized to determine perspective views, including occlusion effects, quickly and efficiently. Unlike point cloud and polygon approaches, this approach requires neither hidden surface removal nor shading processing because the CG technique automatically performs both. Moreover, this approach readily manages natural 3D scenes and 3D computer graphics. However, the final CGH is shaped in most implementations as a series of 2D perspective views, missing the accommodation cue. Well-known examples of this category are holographic stereograms and integral imaging-based displays. Holographic stereograms are composites of simple holograms generated by FTT from 2D images. [Hilaire et. al., 1995]. Holographic stereograms have a much lower computational cost compared to the point cloud and polygon approaches. Instead, deep depth images' accuracy is problematic, even if an observer may identify a 3D image reconstructed from elemental holograms. Researchers have suggested phase-added stereogram, and reliable phase-added stereogram approaches to enhance this process. [Onural et. al., 1994; Smalley, 2006]. Original and modified holographic stereogram computational costs are almost equal. Although binocular disparity and motion parallax cues can be properly supplied along with correct occlusion effects in these displays, all objects appear sharp only when the viewer focuses at a single depth (usually the hologram plane). As a consequence, the well-known VAC of stereoscopic displays is subjected to such implementations. A method is provided for computing realistic 3D object CGHs. The rendered view and the scene depth map are used to deal with occlusion, shading, and parallax effects and prevent VAC. [Kazempourradi et. al., 2017].

The computed full-complex CGH computed by all of the methods discussed shows the virtual object wave inside the eyebox of a holographic display. Further encoding steps, such as amplitude or phase-only or binary modulation, are needed since SLMs do not handle full complex but specific modulation types. A well-known method for encoding complete complex CGHs into amplitude or phase is utilizing error diffusion and iterative Transform based algorithms, respectively. [Wyrowski and Bryngdahl, 1988; Fienup, 1980; Eschbach, 1991]. However, almost all of these algorithms have an iterative structure and require repeated FFT or pixel-by-pixel processing operations that present considerable computational complexity. 2A non-iterative algorithm where simple Discrete Fourier Transform (DFT) relationships are used to determine phase CGHs presented in [Mengu et. al., 2016] by controlling half of the desired image samples through a single FFT.

The complexity of CGH computation has made it difficult to achieve real-time holographic displays. Various efficient computation techniques have been studied [Fienup, 1980], in addition to improvements in GPU performance and CGH generation algorithms.

Look-up-table based methods have been proposed to speed up the calculation [Eschbach, 1991]. Entire pipelines from image rendering to CGH generation have been constructed to achieve fast real-time computation [Mengu et. al., 2016; Gao et. al., 2017]. In particular, high-quality imagery as a compact holographic near-eye display and proposed a linearly separable convolution method with a real-time varying convolution kernel is demonstrated in [Mengu et. al., 2016].

Light field-based hologram rendering techniques have been studied for fast rendering and correct intra-occlusion effects [Gao et. al., 2017]. A method is provided for computing realistic 3D object CGHs. The rendered view and the scene depth map are used to deal with occlusion, shading, and parallax effects and prevent VAC. [Kazempourradi et. al., 2017, Park, 2017]. We report a method for phase-only CGH computation for HNEDs using scalar wave optics, the matrix-optics analogy with paraxial approximation, and IFTA in this thesis. We discuss our computation process's specifics in this thesis to remove speckle noise and chromatic aberrations from light sources and the optics.

Recently, several algorithms using deep learning techniques are provided to accelerate the computation of CGHs [Horisaki et. al., 2018]. A neural network architecture that represents the first CGH algorithm capable of generating full-color holographic images at 1080p resolution in real time is reported in [Peng et. al., 2020]. A non-iterative algorithm that relies on a convolutional neural network for CGH computation is reported in [Eybposh et. al., 2020]. Metasurface holography, realized by encoding the hologram in the metasurface, is investigated in [Jiang et. al., 2019].

1.4 Effect of light source coherency on holographic displays

The high coherency of the light source is vital for reconstructing high-quality holograms. A CGH must be illuminated with a monochromatic point light source to create the desired interference pattern on the image plane. A laser source coupled to single-mode fiber is the best practical light source option. However, using a laser source introduces several artifacts [Reichelt et. al., 2008; Stanley et. al., 2004]. The reconstructed image under the laser source illumination suffers from the speckle noise. Furthermore, the reflections from different surfaces of the optical system shape undesired fringe patterns and degrade the image quality. Several techniques are reported in the literature to avoid the speckle noise, in the cost of increasing the computational cost [Yaraş et. al., 2011; Kozacki et. al., 2012; Reicherter et. al., 1999; Marquet et. al., 2005].

One viable option to reduce speckle noise in holography is using a low temporal and spatial coherent source [Sang et. al., 2011]. Utilizing light-emitting diodes (LEDs) makes it possible to decrease the undesirable interference effects and speckle noise in HNEDs to a certain extent at the expense of reduced resolution [Nobukawa et. al., 2015, Makowski et. al., 2009, Buckley, 2011]. LED sources have a more comprehensive spectral range and a lower spatial coherence in comparison with laser sources. Besides, LEDs do not produce eye hazards, ease application, and small die sizes [Buckley, 2010; Yaraş et. al., 2010; Slinger et. al., 2005]. Recently there is a rising research interest in utilizing LEDs in HNEDs. The effect of using an LED as a light source together with phase-only and amplitude-only SLMs has been studied

[Chellappan et. al., 2010; Dainty, 2013; Garcia et. al., 2005; Tziraki et. al., 2000; Takano et. al., 2007].

In this thesis, we proposed a straightforward analysis using matrix optics for investigating the effect of spatial and temporal coherence of LED sources on the resolution of HNEDs.

1.5 Optical combiners

The optical combiner is often the most complex and most costly optical element in the entire XR display architecture: it is the one component seen directly by the user and the one seen directly by the world. It often defines the size and aspect ratio of the entire headset.

A large FOV and small form factor are required in the design of AR head-worn displays. [Akşit et. al., 2015]. As relay elements, traditional AR head-worn displays with large FOV use bulky optical lenses and mirrors. In consumer applications, the low form factor of such displays impedes their adoption. Different solutions have been exploited by alternative techniques to reduce the size and bulk of the optics. One promising solution is active pupil tracking, but pupil tracking's optical methods are complicated [Jang et. al., 2017]. Other approaches to reducing the form factor in near-eye displays are unconventional relay optics, including holographic optical elements, waveguides, and diffractive optics [Jang et. al., 2016; Mukawa et. al., 2009; Levola, 2006]. Holographic optical elements (HOEs) using volume gratings are an excellent option for replacing bulky elements with thin and flat components, making near-eye display optics more compact and lighter. [Zhou et. al., 2018].

HOEs are manufactured by recording interference patterns on high-resolution photosensitive materials from two coherent light beams. For each wavelength and optical design, this process requires carefully calibrated and stable optical setups. It is also challenging to physically acquire the wavefronts free of aberrations for specific components such as high NA lenses. It may first require the physical manufacturing of the associated traditional component. The recording laser's wavelength does not correspond to the target wavelength in certain situations, further complicating the production process. [Kim et. al., 2017]. During the manufacturing process, the shrinkage of the final HOEs should also be considered and compensated. [Sweatt, 1977].

Alternative flat lens technology is the micro-mirror array (MMA). First, compared to the HOE case, the MMA does not require the preparation of a physical interference setup but can be numerically configured to substitute any traditional optical relay element for any desired wavelength. Although a HOE needs to be recorded separately in each new sample's interference setup, an initial MMA sample can be manufactured once with grayscale lithography. It can then be used as a master shim from which several MMA replicas can be easily made. Besides, the MMA retains its light efficiency with small changes in the output focal spot location and shape because of its reflective nature compared to HOEs. Light efficiency falls rapidly with deviations from design wavelengths and input light directions. Due to their large micro-mirror sizes, active MMA designs that have previously been studied often provide low quality [Song et. al., 2018]. Several passive MMAs are designed using ray optics and used in various displays [Yan et. al., 2004; Ochiai et. al., 2017]. In designing and manufacturing tiny optical elements, obtaining high diffraction efficiency is a challenge, especially for diffractive optical elements (DOEs) with wide off-axis deflection angles and high numerical aperture lenses. The DOE phase function is either approximated by a multilevel structure or realized directly as continuous surface relief with an analog profile to obtain high efficiency. [Hessler et. al., 1998]. MMA is a type of DOE with a discrete pixelated structure for surface relief.

1.6 Contribution of the thesis research

Generic paraxial HNED architectures have been analyzed in terms of FOV and resolution (eye box). The analysis reveals the structure of the FOV versus resolution tradeoffs that are feasible under the space bandwidth product constraint. The developed formulas constitute an easy guide for the design of paraxial HNEDs with the desired FOV versus resolution characteristics. A generic CGH computation procedure is formulated for paraxial HNED architectures in terms of ABCD parameters. The procedure can handle arbitrary placement of the SLM in the optical train, and arbitrary optics between the light source and SLM, and SLM and eye.

Using our analysis results, we computed a CGH printed on a binary lithography mask to demonstrate a direct view (lensless) and speckle free HNED with a FOV of 70° degrees for the first time. This demonstration verifies the ultimate HNED architecture, which consists only of a CGH illuminated by the diverging beam from a point light source, without any optics in between. We also designed and developed full-color HNEDs that are free from chromatic aberrations. We showed that besides conventional HNED designs providing uniform resolution over the FOV. It is also possible to design foveated HNEDs that mimic human vision by providing varying resolution across the FOV, resulting in better utilization of the SLM's available space-bandwidth product.

We examined the effect of spatial and temporal coherence of LED sources on the resolution of HNEDs and confirmed the theoretical analysis with experiments. We showed that the loss in spatial resolution of holographic images due to the light source's spatial incoherence depends on the depth of objects and increases as the object depth gets separated from the virtual SLM plane's location. We demonstrated a range of HNED architectures for which LED sources can replace the laser sources while keeping the loss in spatial resolution imperceivable to the human eye.

An alternative thin and flat lens consisting of an array of micromirrors (MMA) is introduced to reduce the size and bulk of relay optics for HNEDs. Micro-mirror sizes and shapes are optimized using diffraction simulations to satisfy a phase-matching condition simultaneously for three wavelengths and the fabrication process's constraints. The MMA was fabricated using grayscale lithography and tested successfully in an HNED architecture. The developed structure is expected to stimulate further research on novel planar diffractive optical components in HNED systems.

1.7 Outline of the dissertation

In Chapter 2, the matrix-optics approach analyzes the FOV and the eyebox size of an HNED. We determine the FOV of an HNED followed by a condition on the size of the eyebox using matrix-optics analysis, which results in a fundamental relation between the product of the FOV and effective eyebox size. The design procedure of an HNED and CGH computation for HNEDs using scalar wave optics and paraxial approximation is presented in Chapter 2. Furthermore, the experimental results are reported using different optical setups with collimated, converging, or diverging SLM illumination in this chapter.

In Chapter 3, we proposed a straightforward analysis using matrix optics for investigating the effect of spatial and temporal coherence of LED sources on the resolution of HNEDs. The provided analysis helps us to optimize the optical architecture and minimize the side effects of utilizing LEDs. We experimentally investigated the spatial coherence of LED illumination with various pinhole sizes.

Chapter 4 details information on the MMA design and fabrication as an alternative thin and flat lens technology is introduced to reduce the size and bulk of the relay optics for HNEDs. The contributions of this thesis are summarized and discussed in Chapter 5.

Chapter 2

MATRIX-OPTICS ANALYSIS OF COMPUTATIONAL HOLOGRAPHIC NEAR-EYE DISPLAYS

Holographic near-eye displays (HNEDs) deliver virtual images using computer-generated holograms (CGHs) displayed on spatial light modulators (SLMs). Holographic displays allow for a vast range of optical architectures that are not possible with conventional micro-display-based designs. However, due to the space-bandwidth limitations of SLMs, HNEDs have a limited field of view (FOV) and eyebox size.

In this chapter, we developed a simple paraxial ABCD matrix optics-based method for designing holographic displays. We show that FOV and eyebox size limitations of HNEDs can be extended beyond what has been reported in the literature. The method allows for the design and analyses of Fourier and other types of holographic displays where the SLM's virtual image can appear anywhere in space. Furthermore, we used the ABCD matrix representation for efficient CGH computation using scalar wave optics. We confirmed our matrix-optics method with several simulations and experiments.

2.1 Introduction

A generic HNED architecture consists of three fundamental planes: a point light source plane, the SLM plane, and an eye plane. A sample of HNED optical architecture is illustrated in Figure 2.1(a). The light emits from a point light source and passes through a collimating lens of focal length f. The collimated light reflects toward the SLM after hitting the beam splitter surface. The modulated beams reflect from the SLM plane and propagate a distance to reach the eye-piece lens. The eye-piece lens focuses the light on the pupil plane. An image of a resolution chart is provided in Figure 2.1(b) and is used for the schematic reconstructions. A schematic drawing of two different optical architectures with collimated SLM illumination is illustrated in Figure 2.1(c) and Figure 2.1(d). The architecture provided in Figure 2.1(c) has a higher FOV (indicated with solid black lines) compared to the architecture provided in Figure 2.1(d), where a smaller portion of the sample image is captured. However, the resolution of the reconstructed image degrades except for a small part of the FOV. This case is schematically illustrated in the left (the reconstructed image) and middle (eyebox size versus FOV curve) images of Figure 2.1(c). In the architecture shown in Figure 2.1(d), a larger portion of FOV has a full resolution. We should note that the area under eyebox size versus the FOV curve is constant for both systems.

We developed a simple paraxial ABCD matrix optics-based method for designing holographic displays and show that FOV and eyebox size limitations of HNEDs can be extended beyond what has been reported in the literature.

We report a method for phase-only CGH computation for HNEDs using scalar wave optics and the matrix-optics analogy with paraxial approximation. The developed HNEDs provide full-color and high-quality holograms with high resolution and proper per-pixel focal control in the fovea.

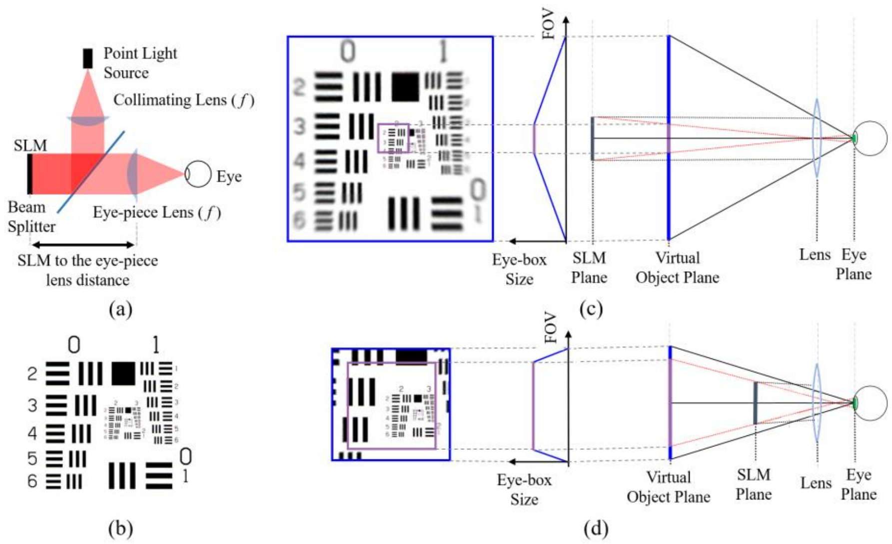

Figure 2.1 (a) A sample HNED optical architecture is illustrated. The light emits from a point light source and passes through a collimating lens of focal length f. The collimated light reflects toward the SLM after hitting the beam splitter surface. The modulated beams reflect from the SLM plane and propagate a distance to reach the eye-piece lens. The eye-piece lens focuses the light on the pupil plane. (b) An image of a resolution chart that is used for the schematic reconstructions. A schematic drawing of two different optical architectures with collimated SLM illumination is illustrated (c) and (d). The architecture provided in (c) has a higher FOV (indicated with solid black lines) compared to the architecture provided in (d), where a smaller portion of the sample image is captured. However, the resolution of the reconstructed image degrades except for a small part of the FOV. This case is schematically illustrated in the left (the reconstructed image) and middle (eyebox size versus FOV curve) images of (c). In the architecture shown (d), a larger portion of FOV has the full resolution. We should note that the area under eyebox size versus FOV curve is constant for both systems (c) and (d).

2.2 Field-of-view and eyebox size analysis

We determine the FOV of the HNED followed by a condition on the size of the eyebox using matrix-optics analysis, which results in a fundamental relation between the product of the FOV and effective eyebox size. Consider the object point placed at x_{OB} on the virtual object plane at a distance of z_{OB} from the eye plane. This object point has an angle of θ_{OB} with respect to the center of the eyebox placed at x_{EB} on the eye plane, as shown in Figure 2.2.

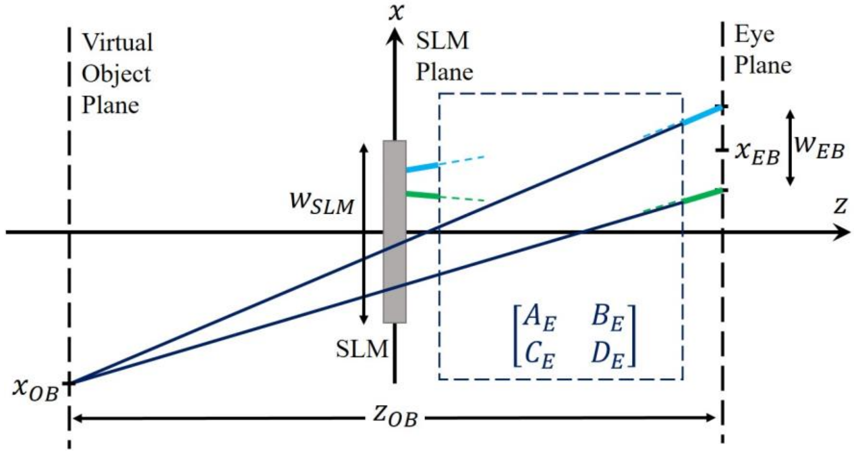

Figure 2.2 Consider the object point placed at x_{OB} on the virtual object plane at a distance of z_{OB} from the eye plane. This object point has an angle of θ_{OB} with respect to the center of the eyebox placed at x_{EB} on the eye plane. The width of SLM is denoted by w_{SLM} and w_{EB} is the eyebox width.

The width of SLM is denoted by w_{SLM} and w_{EB} is the eyebox width in Figure 2.2. The rays emanating from the virtual object point that fall into the eyebox on the eye plane are expressed as (x_p, θ_p). The rays (x_s, θ_s) on the SLM plane must be launched to reproduce (x_p, θ_p) after passing the eye-piece module optics. In Figure 2.2, A_E, B_E, C_E and D_E are the elements of the eye-piece optics module matrix. Using matrix optics calculations, we see that the footprint of rays from the considered virtual object point is centered around

$$x_{CRP} = D_E x_{EB} - B_E \theta_{OB}, \tag{2.1}$$

where x_{CRP} is the chief ray position on the SLM plane and occupy an interval of size:

$$\Delta x_{SLM} = w_{EB} \left| D_E - \frac{B_E}{z_{OB}} \right|. \tag{2.2}$$

2.2.1 Field-of-view

We consider the two possibilities for the size footprint of rays on the SLM with respect to the SLM width and derive a generalized expression for the resolution and FOV of a given HNED system.

In a holographic near-eye display, we can find the SLM field in two steps, as shown by the yellow arrow in Figure 2.3. In the first step, the emanated field from virtual object points fills the eyebox. The field on the eyebox is back-propagates through the eye-piece optics in the second step and forms the field on the SLM plane.

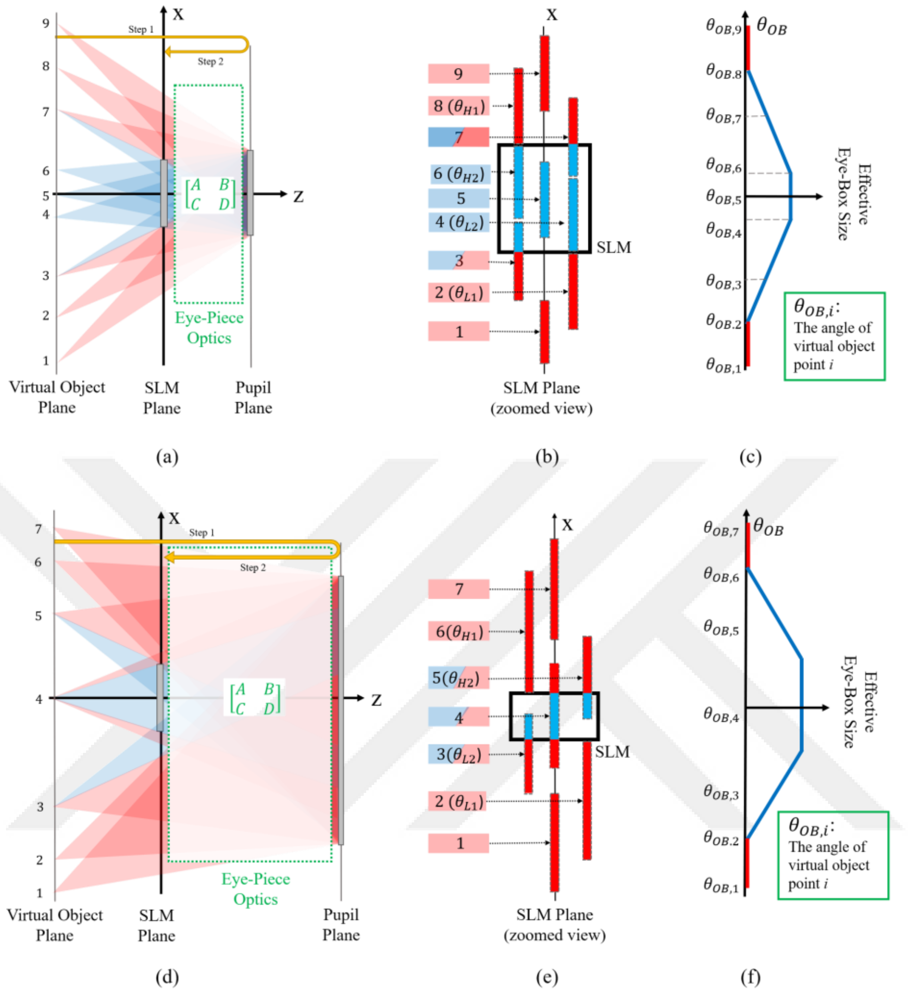

Figure 2.3 Case 1: $\Delta x_{SLM} < w_{SLM}$: (a) A schematic drawing of the rays emanating from 9 different positions on the virtual object plane and falling into the eyebox on the eye plane. The blue rays fall within the SLM aperture and can be generated using the display. The red rays fall outside the SLM aperture and cannot be displayed. (b) The SLM plane's zoomed view represents the footprint of the rays on the SLM plane emanating from the virtual object points. The rays falling into the SLM aperture are shown with blue, and the rays that cannot be displayed are illustrated with red. (c) The plot illustrates the effective eyebox size for different object point angles. Case 2: $\Delta x_{SLM} > w_{SLM}$: (d) A schematic drawing of the rays emanating from 7 different positions on the virtual object plane and falling into the eyebox on the eye plane. The blue rays fall within the SLM aperture and can be generated using the display. The red rays fall outside the SLM aperture and cannot be displayed. (e) The SLM plane's zoomed view represents the footprint of the rays on the SLM plane emanating from the virtual object points. The rays falling into the SLM aperture are shown with blue, and the rays that cannot be displayed are illustrated with red. (f) The plot illustrates the effective eyebox size for different object point angles.

Case 1: $\Delta x_{SLM} < w_{SLM}$

For $\Delta x_{SLM} < w_{SLM}$, the footprint of rays on the SLM occupies a smaller space compared to the SLM width. Figure 2.3(a) illustrates a schematic drawing of the rays emanating from 9 different positions on the virtual object plane and falling into the eyebox on the eye plane. The blue rays in Figure 2.3(a) fell within the SLM aperture and are generated using the display. The red rays fall outside the SLM aperture and cannot be displayed, as evident in Figure 2.3(a). Object points between point 2 and point 8 in Figure 2.3(a) are within the FOV of the display. Object points between point 4 and point 6 can be displayed within the entire eyebox. Object points between point 2 and point four and object points between point 6 and point 8 can only be displayed within sub-regions of the eyebox and have a smaller effective eyebox size. The zoomed view of the SLM plane shown in Figure 2.3(b) represents the rays' footprint on the SLM plane emanating from the virtual object points shown in Figure 2.3(a). The rays falling into the SLM aperture are shown with blue, and the rays that cannot be displayed are illustrated with red. Figure 2.3(c) illustrates the effective eyebox size for different object point angles.

As shown in Figure 2.3(a)-Figure 2.3(c), θ_{L_1} is the angle of object point 2, θ_{L_2} is the angle of object point 4, θ_{H_2} is the angle of object point 6, θ_{H_1} is the angle of object point 8. Assuming $B_E < 0$ and $D_E - \frac{B_E}{z_{OB}} > 0$, the value of θ_{OB} can be calculated using

$$\theta_{OB} = \frac{1}{B_E}\left(D_E x_{EB} - x_s + \Delta_x\left(D_E - \frac{B_E}{z_{OB}}\right)\right), \tag{2.3}$$

with $|\Delta x| \leq w_{EB}/2$. For $\theta_{OB} = \theta_{L_1}$, we replace x_s with $-w_{SLM}/2$ and $\Delta_x = +w_{EB}/2$ in Equation 2.3. Setting $x_s = -w_{SLM}/2$ and $\Delta_x = -w_{EB}/2$ results in $\theta_{OB} = \theta_{L_2}$. For object point 6, we set $x_s = +w_{SLM}/2$ and $\Delta_x = +w_{EB}/2$ to find $\theta_{OB} = \theta_{H_2}$. Finally, the value for $\theta_{OB} = \theta_{H_1}$ can be calculated by setting $x_s = +w_{SLM}/2$ and $\Delta_x = -w_{EB}/2$ in Equation 2.3. The assumption of $B_E < 0$ means the virtual object maps with the same orientation on the SLM plane, while the virtual object gets inverted for $B_E < 0$. The rays on the eyebox map in the same order as the virtual objects for $D_E - \frac{B_E}{z_{OB}} > 0$, while having $D_E - \frac{B_E}{z_{OB}} < 0$ condition reverses the order of the object points on the eyebox. We also define the angle of the center point of the FOV as $\theta_C = \frac{D_E x_{EB}}{B_E}$.

Case 2: $\Delta x_{SLM} > w_{SLM}$

In this case, the footprint of rays on the SLM plane is larger than the SLM width, and none of the object points can be shown over the entire eyebox. Figure 2.3(d) illustrates a schematic drawing of the rays emanating from 7 different positions on the virtual object plane and falling into the eyebox on the eye plane. The blue rays in Figure 2.3(d) fell within the SLM aperture and are generated using the display. The red rays fall outside the SLM aperture and cannot be displayed, as evident in Figure 2.3(d). When the footprint of the rays on the SLM plane matches the SLM aperture size (i.e., the virtual object points are between point 3 and point 5 in Figure 2.3(d)), the maximum effective eyebox size of

$$w_{EB_{\max}} = \frac{w_{SLM}}{\left|D_E - \frac{B_E}{z_{OB}}\right|} \tag{2.4}$$

is achieved. The zoomed view of the SLM shown in Figure 2.3(e) represents the rays' footprint on the SLM plane emanating from the virtual object points defined in Figure 2.3(d), where the rays falling into the SLM aperture are shown with blue. The rays that cannot be displayed are illustrated with red. Figure 2.3(f) illustrates the effective eyebox size for different object point angles. As shown in Figure 2.3(e), θ_{L_1} is the angle of object point 2, θ_{L_2} is the angle of object point 3, θ_{H_2} is the angle of object point 5, θ_{H_1} is the angle of object point 7. Similar to Case 1, the values for θ_{L_1}, θ_{L_2}, θ_{H_2} and θ_{H_1} can be computed.

2.2.2 *Field-of-view formula*

The values for θ_{L_1}, θ_{L_2}, θ_{H_2} and θ_{H_1} for both Case 1 and Case 2 can be expressed using the following generalized formula:

$$\theta_A = \frac{D_E x_{EB}}{B_E} + s_1 \cdot \frac{w_{SLM}}{2|B_E|} + s_2 \cdot \frac{w_E B}{2|B_E|} \cdot \left|D_E - \frac{B_E}{z_{OB}}\right|, \tag{2.5}$$

where $A \in \{L_1, L_2, H_2, H_1\}$, $s_1 \in \{-1, +1\}$ and $s_2 \in \{-1, +1\}$. Table 2.1 presents the values for A, s_1 and s_2 for both of the cases.

Table 2.1. The values for θ_{L_1}, θ_{L_2}, θ_{H_2} and θ_{H_1} for both Case 1 and Case 2

Case 1: $\Delta x_{SLM} < w_{SLM}$			Case 2: $\Delta x_{SLM} > w_{SLM}$		
A	s_1	s_2	A	s_1	s_2
L_1	-1	-1	L_1	-1	-1
L_2	-1	1	L_2	1	-1
H_2	1	-1	H_2	-1	1
H_1	1	1	H_1	1	1

The general plot of the effective eyebox size versus the angle of the virtual object point (i.e., FOV) is provided in Figure 2.4.

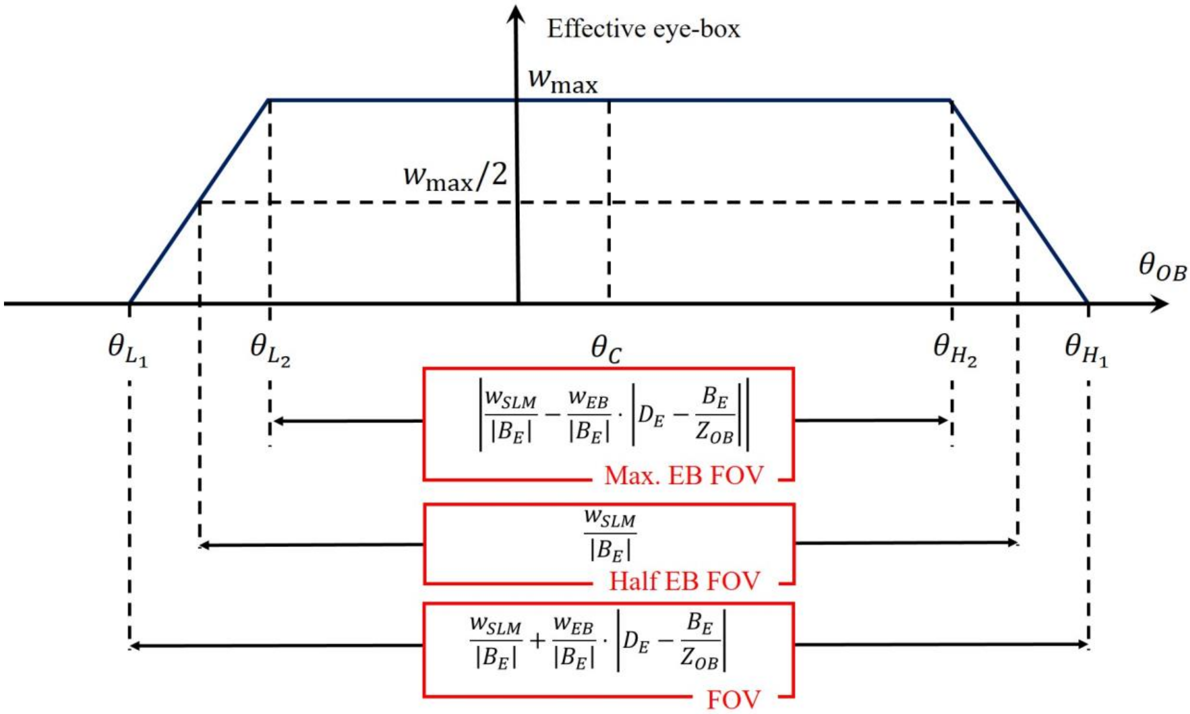

Figure 2.4 The general plot of the effective eyebox size versus the angle of the virtual object point (i.e., FOV) is illustrated. According to our definitions, total FOV depends on the distance of the virtual object plane to the eye plane (z_{OB}). Total FOV is minimum for $z_{OB} = B_E/D_E$ with a value of $w_{SLM}/|B_E|$, where the SLM and the virtual object point become conjugates, and the plot becomes a rectangular box (i.e., $\theta_{L_1} = \theta_{L_2}$ and $\theta_{H_1} = \theta_{H_2}$). The maximum value of the effective eyebox size is denoted with w_{max}.

According to our definitions, total FOV depends on the distance of the virtual object plane to the eye plane (z_{OB}). Total FOV is minimum for $z_{OB} = B_E/D_E$ with a value of $w_{SLM}/|B_E|$, where the SLM and the virtual object point become conjugates and the plot in Figure 2.4 becomes a rectangular box (i.e., $\theta_{L_1} = \theta_{L_2}$ and $\theta_{H_1} = \theta_{H_2}$). The maximum value of the effective eyebox size is denoted with $w_{\max}$ and has the following value:

$$w_{\max} = \begin{cases} w_{EB} & \text{if } \Delta x_{SLM} < w_{SLM} \\ \dfrac{w_{SLM}}{\left|D_E - \dfrac{B_E}{z_{OB}}\right|} & \text{if } \Delta x_{SLM} \geq w_{SLM} \end{cases} \tag{2.6}$$

Based on the results provided in Figure 2.4, the FOV of the system is

$$\theta_{FOV} = \frac{w_{SLM}}{|B_E|} + \frac{w_{EB}}{|B_E|} \cdot \left| D_E - \frac{B_E}{z_{OB}} \right|. \tag{2.7}$$

2.2.3 Restriction on the eyebox size

Until now, we did not restrict the size of the eyebox (w_{EB}). In practice, there is an upper limit on the w_{EB} that is imposed by the limited bandwidth or the finite number of pixels of the SLM. Suppose the SLM pixel pitch is Δ. The SLM can uniquely represent a signal that locally fits within a band of size $1/\Delta$. Equivalently, under paraxial approximation, the ray spread around each SLM point should be limited to an interval of size λ/Δ.

A set of rays is defined on the pupil plane as (x_p, θ_p) and the rays (x_s, θ_s) are defined on the SLM plane. Doing some algebra, we conduct that

$$\theta_s = \frac{x_p}{B_E} - \frac{A_E}{B_E} x_s \tag{2.8}$$

and θ_s is limited to

$$\frac{x_{EB}}{B_E} - \frac{A_E}{B_E} x_s - \frac{w_{EB}}{2|B_E|} \leq \theta_s \leq \frac{x_{EB}}{B_E} - \frac{A_E}{B_E} x_s + \frac{w_{EB}}{2|B_E|}. \tag{2.9}$$

Thus, the rays around a point on the SLM have a spread of $w_{EB}/|B_E|$. This spread, as discussed above, should not exceed λ/Δ, which leads to the following condition on the size of the eyebox:

$$w_{EB} < \frac{\lambda |B_E|}{\Delta}. \tag{2.10}$$

If w_{EB} exceeds $\frac{\lambda|B_E|}{\Delta}$, we get different interpretations for different cases. An SLM with a pixelated nature generates diffraction orders, and the orders propagate to the eye plane. Some of the higher diffraction orders leak into the eyebox, corrupting the displayed image with ghosts. Even if the system uses internal filters, it will not isolate the signal beam from higher diffraction orders without clipping the eyebox. If the SLM does not generate diffraction orders, since ray spread exceeds the SLM capability, some rays will not get generated, effectively reducing the size of the eyebox.

2.2.4 The area under the eyebox size versus FOV curve

The area under the curve (S) provided in Figure 2.4 is

$$S = w_{\max} \cdot \frac{w_{SLM}}{|B_E|} = \begin{cases} w_{EB} \cdot \dfrac{w_{SLM}}{|B_E|} & \text{if } \Delta x_{SLM} < w_{SLM} \\ \dfrac{w_{SLM}}{|B_E|} \cdot \dfrac{w_{SLM}}{\left|D_E - \dfrac{B_E}{z_{OB}}\right|} & \text{if } \Delta x_{SLM} \geq w_{SLM} \end{cases} \tag{2.11}$$

Using the results from Equation 2.6 and Equation 2.10, we conduct that

$$S < \lambda \frac{w_{SLM}}{\Delta}. \tag{2.12}$$

Note that the number of SLM pixels is $N_p = w_{SLM}/\Delta$ and we have the following fundamental result:

$$S = \int_{\theta} \mathrm{EEB}\,(\theta)\,\mathrm{d}\theta < \lambda N_p, \tag{2.13}$$

where $\mathrm{EEB}(\theta)$ is the effective eyebox size for each virtual object point in the FOV. The result is Equation 2.13 enforces that all holographic head-mounted designs should target an eyebox size versus FOV curve subject to this condition. Total FOV is minimum for $z_{OB} = B_E/D_E$ with a value of $w_{SLM}/|B_E|$, where the SLM and the virtual object point become conjugates and the plot in Figure 2.4 becomes a rectangular box (i.e., $\theta_{L_1} = \theta_{L_2}$ and $\theta_{H_1} = \theta_{H_2}$). In this case, the product of the FOV and effective eyebox size is equal to the area under the eyebox size versus the FOV curve.

2.3 Holographic near-eye display design

In this section, we focus on how to design the eye-piece optics module or M_E, such that a specific FOV is achieved for a specified eyebox size. In a practical design, we typically want to utilize only some fraction of the available SLM bandwidth $1/\Delta$. There are various reasons for this choice. Most SLMs have a restricted modulation form, such as phase-only, amplitude-only, and binary, rather than full-complex modulation. The full-complex signal must be embedded into such restricted type signals with the addition of some encoding noise. Part of the SLM bandwidth must be reserved for the noise term. The noise term can be random noises in iterative procedures such as IFTA or conjugate beams in amplitude modulation. Furthermore, we need to leave some gap between the signal beam's replicas to filter the replicas out either on the eye plane by the user’s pupil or some aperture in an internal filtering plane. The same is true for eliminating the unmodulated beam and its higher diffraction orders.

We summarize all the discussion with a parameter called the SLM space-bandwidth product utilization ratio η, where $0 < \eta < 1$. Assuming that system parameters change only marginally with the wavelength in full-color holographic displays, we choose the blue wavelength as the safe design wavelength, and the design process applies for the red and green wavelengths, and we have

$$\eta_B = \eta, \tag{2.14}$$

$$\eta_G = \eta \cdot \frac{\lambda_B}{\lambda_G}, \tag{2.15}$$

and

$$\eta_R = \eta \cdot \frac{\lambda_B}{\lambda_R}, \tag{2.16}$$

where the R, G, and B represent the red, green, and blue colors, respectively. Given λ, Δ, w_{SLM} and N_p, we start the design by specifying $w_E B$, η and θ_{FOV} for a given virtual object plane at a distance of z_{OB}. Virtual objects will be visible in the region defined by w_{EB}, however, recall that not all object points may be visible at all points of the eyebox in general. For a specific η, the effective pixel pitch of the SLM will be Δ/η, and the effective pixel count will be $\eta \cdot N_p$. The modified form of Equation 2.10 will be

$$w_{EB} = \eta\lambda \frac{|B_E|}{\Delta}, \tag{2.17}$$

which sets

$$|B_E| = \frac{\Delta w_{EB}}{\eta\lambda}. \tag{2.18}$$

The FOV must be specified for a specific z_{OB}. According to the developed theory, there is no mathematical upper limit for the θ_{FOV} (in practice, we note that $\theta_{FOV} < \pi$), but there is a lower limit $\theta_{FOV,\min}$, i.e.,

$$\theta_{FOV} \geq \frac{w_{SLM}}{|B_E|} = \theta_{FOV,\min}, \tag{2.19}$$

where using Equation 2.18, we conduct that

$$\theta_{FOV,\min} = \frac{\eta\lambda N_p}{w_{EB}}. \tag{2.20}$$

We define a sign parameter $s_3 \in \{-1, +1\}$ and rewrite Equation 2.18 as

$$B_E = s_3 \cdot \frac{\Delta w_{EB}}{\eta\lambda}. \tag{2.21}$$

Furthermore, we define another sign parameter $s_4 \in \{-1, +1\}$, such that $|D_E - B_E/z_{OB}| = 1/s_4 \cdot (D_E - B_E/z_{OB})$. Substituting s_4 in Equation 2.7, we find the value of the D_E as

$$D_E = s_3 \cdot \left(\frac{\Delta w_{EB}}{\eta\lambda z_{OB}}\right) + s_4 \cdot \left(\frac{\theta_{FOV}\Delta}{\eta\lambda} - \frac{w_{SLM}}{w_{EB}}\right). \tag{2.22}$$

It is well known that any optical system can be modeled as a combination of free-space propagation, a thin lens, and other free-space propagation within the domain of paraxial optics. In this respect, the architecture of the eye-piece optics module of a generic paraxial HNED has the form depicted in Figure 2.5.

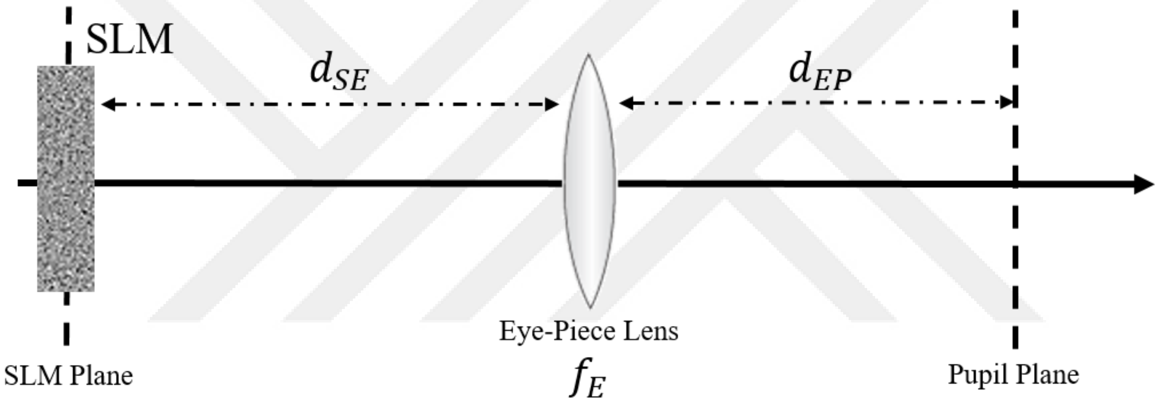

Figure 2.5 Architecture of the eye-piece optics module of a generic paraxial HNED. The distance between the SLM and the eye-piece lens is d_{SE}, the distance between the eye-piece lens and the pupil plane is d_{EP} and the eye-piece lens has a focal length of f_E.

The distance between the SLM and the eye-piece lens is d_{SE}, the distance between the eye-piece lens and the pupil plane is d_{EP} and the eye-piece lens has a focal length of f_E, as evident in Figure 2.5.

The matrix representation of the system shown in Figure is:

$$\mathrm{M}_E = \begin{bmatrix} A_E & B_E \\ C_E & D_E \end{bmatrix} = \begin{bmatrix} 1 - \frac{d_{EP}}{f_E} & d_{SE} + d_{EP} - \frac{d_{SE}d_{EP}}{f_E} \\ \frac{-1}{f_E} & 1 - \frac{d_{SE}}{f_E} \end{bmatrix}. \tag{2.23}$$

Because $|\mathrm{M}_E| = 1$, the matrix M_E and the equivalent optical system has 3 degrees of freedom (DOFs) as

$$d_{EP} = \frac{A_E - 1}{C_E}, \tag{2.24}$$

$$d_{SE} = \frac{D_E - 1}{C_E} \tag{2.25}$$

and

$$f_E = \frac{-1}{C_E}. \tag{2.26}$$

Until now, we specify two DOFs with Equation 2.21 and Equation 2.22, where we have four alternatives due to the sign parameters s_3 and s_4. Once A_E, B_E, C_E and D_E are determined, the values for d_{EP}, d_{SE} and f_E can be found. If $d_{EP}, d_{SE} > 0$ the system is physically realizable. We need to impose additional conditions, and we will study two possible options.

2.3.1 Option 1: Set $d_{EP} = f_E$

In this case, the pupil plane is placed on the focal plane of the eye-piece lens, and plane waves on the SLM plane get focused on the eye plane. In some cases, the beam illuminating the SLM gets partly modulated, with an unmodulated beam traveling unaffected from the CGH on the SLM. It may be good to image an unmodulated beam on the eye plane and filter it out by the user's pupil in such cases. This option also allows the collimated illumination of the SLM for positive values of f_E. In this case $A_E = 0$ and the following set of equations characterize the system:

$$1 - \frac{d_{SE}}{f_E} = D_E, \tag{2.27}$$

$$d_{SE} + d_{EP}D_E = B_E \tag{2.28}$$

and

$$d_{EP} = f_E. \tag{2.29}$$

Doing some algebra and considering Equation 2.21 and Equation 2.22, the values for f_E, d_{SE} and d_{EP} can be found as

$$f_E = B_E, \tag{2.30}$$

$$d_{SE} = B_E(1 - D_E) \tag{2.31}$$

and

$$d_{EP} = B_E. \tag{2.32}$$

2.3.2 Option 2: Set $d_{EP} = d_{EC}$

In this case, we specify a particular eye-clearance distance d_{EC}. Along with Equation 2.21 and Equation 2.22, this condition determines the system such that

$$f_E = \frac{B_E - d_{EC} \cdot D_E}{1 - D_E}, \tag{2.33}$$

$$d_{SE} = B_E - d_{EC} \cdot D_E, \tag{2.34}$$

and

$$d_{EP} = d_{EC}. \tag{2.35}$$

2.3.3 Specific D_E values and the relation with FOV

In this section, we elaborate on some specific D_E values. From Equation 2.22, we know that the specification of FOV merely affects D_E.

Case 1: $D_E = \frac{B_E}{z_{OB}}$

This case corresponds to a FOV specification of $\theta_{FOV} = \theta_{FOV,\min}$. In this case, the SLM is imaged to z_{OB}. We get the minimum FOV and a uniform rectangular eyebox size versus the FOV curve at some specific depth.

Case 2: $D_E = \frac{B_E}{z_{VOP}}$

This case is essentially similar to the previous one. However, it can be useful when the SLM is conjugate to some plane specified as z_{VOP}. FOV is still specified at z_{OB}, which may be different from that z_{VOP}. The FOV at z_{VOP} will be smaller than the FOV at z_{OB}, for a z_{VOP} different than z_{OB} and we have

$$\theta_{FOV} = \theta_{FOV,\min} + w_{EB} \cdot \left|\frac{1}{z_{VOP}} - \frac{1}{z_{OB}}\right|. \tag{2.36}$$

Case 3: $D_E = 1$

The condition $D_E = 1$ implies that $d_{SE} = 0$ in Figure 2.5, and the eye-piece lens is placed right after the SLM, which can also be removed. Note that this case does not work with design option 2, implying that in this case, the eye-clearance distance cannot be arbitrarily specified. The FOV of the system is $\theta_{FOV} = \theta_{FOV,\min}$ at $z_{OB} = \frac{\eta\lambda}{\Delta w_{EB}}$, that is the distance required to separate the higher diffraction orders of the SLM by w_{EB}/η.

Case 4: $D_E = \frac{-B_E}{r_e}$

In this case, the SLM gets imaged to the rotation center of the eye, where r_e denotes the radius of the user's eye. In other words, SLM is conjugated to the retina and acts as a microdisplay with an additional degree of freedom to compensate for the aberrations in the optical train. There is an exciting implementation of a foveated display architecture, where an extended holographic FOV can be obtained by simply rotating the eye [Cem et. al., 2020].

2.4 CGH computation for HNEDs using scalar wave optics and paraxial approximation

This research uses the scalar wave optics theory of light and paraxial approximation for CGH computation. Given a 3D scene, we use a graphical processing unit (GPU) and computer graphics methods to define perspective images for a set of viewpoints. Besides, the depth map information that is already computed during rendering calculations is extracted and used. We break the scene into several slices centered on the depth map, each corresponding to a particular depth. Then, using an FFT based Fresnel transform representing the depth slice's contribution to the field on the SLM plane, we calculate an intermediate field for each slice. The entire field for a perspective on the SLM plane is obtained by superposing the depth slices' intermediate fields. Afterward, to tackle the light source and eyebox positions, linear and quadratic phase terms are superimposed. The proposed process quickly computes a CGH with correct occlusion and accommodation effects. The resulting complex function is coded into a phase-only pattern using the iterative Fourier transform algorithm (IFTA) with about ten iterations for experiments with phase-only SLM reported in this chapter. For the fabricated binary mask, the same procedure is used except that encoding is performed using the error diffusion algorithm.

Our computational procedure is also optimized for speckle-free image formation. Our technique begins because the human eye images a point object not as a point but as an Airy disk on the retina due to diffraction from the eye's pupil. The individual Airy disks of close-by object points interact with each other in an extended object illuminated with coherent light. The granular surface structure contributes to a random phase distribution on the object points, whether it is an ordinary, physically existing real object. Therefore, there are also random phase values of the individual Airy disks on the retina. The resultant interference pattern consists of increasingly varying disruptive and constructive areas, seen as speckle noise to a user. However, there is full freedom in assigning a phase value to object points in a virtual object. In particular, if an initial phase value is assigned to the object points such that all Airy disks arrive at the retina at the same phase, the distribution of retinal intensity is smoothly interpolated, and speckle noise is effectively eliminated. The images that result appear similar to images that would be produced with incoherent light. The HNED architecture consists of a point light source, an SLM, an eyebox plane, and optical components in between. The HNED is modeled as a combination of a free-space propagation, a thin lens, and another free-space propagation. In this respect, a generic paraxial HNED architecture has the form depicted in Figure 2.6, which is the architecture we consider in this thesis.

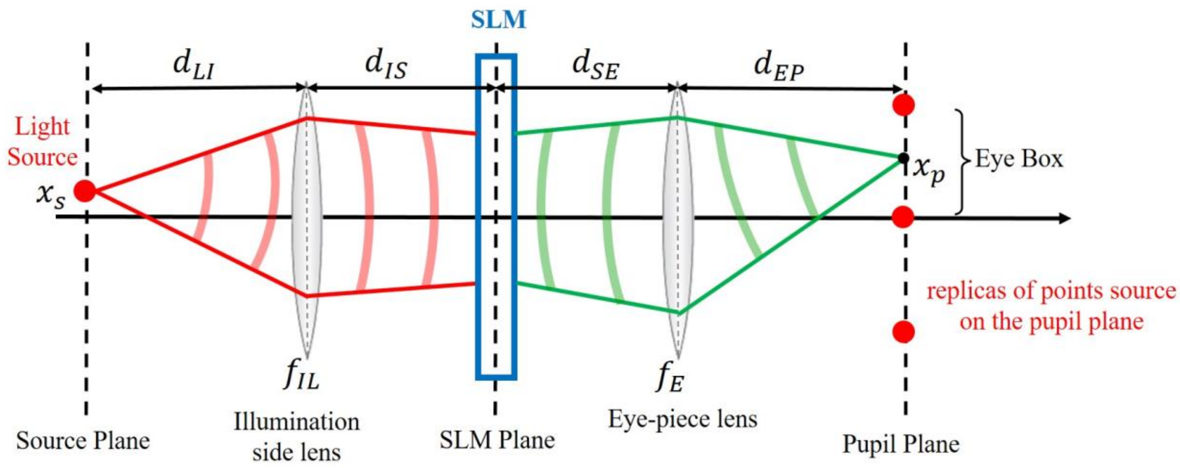

Figure 2.6 The generic paraxial HNED architecture is demonstrated. Light is emitted by a point source located at x_s and propagates for a distance of d_{LI}. The beam travels through the illumination side lens with a focal length of f_{IL} and propagates for a distance of d_{IS} where it hits the SLM. Light emanates from the source and goes through the illumination optics module (shown with a solid red box). The light is modulated after passing through the SLM, which is modeled as a thin multiplicative optical element. Light propagates a distance of d_{SE} to the eye-piece lens with a focal length of f_EAnd another propagation for a distance of d_{EP} after which they reach the pupil plane, where an eyebox is constructed around x_p. The point source's image replicas are created on the pupil plane since part of the incident light does not modulate in most SLMs. Besides, diffraction orders of both modulated and unmodulated beams are formed by the SLM's pixelated structure. This chapter assumes that since the separation between two consecutive diffraction orders is minimum for blue wavelength, the eyebox fits in the free region between the zeroth and first orders of the blue non-modulated beams. The rays propagate into the user's eye (shown with a solid green box).

As illustrated, light is emitted by a point source located at x_s and propagates for a distance of d_{LI}. The light passes through the illumination side lens with a focal length of f_{IL} and propagates for a distance of d_{IS} where it impinges on the SLM. Equivalently, light is emitted by the light source and passes through the illumination optics module (illustrated with a solid red box), described by the matrix

$$\mathrm{M}_I = \begin{bmatrix} A_I & B_I \\ C_I & D_I \end{bmatrix}. \tag{2.37}$$

The light gets modulated upon passage through the SLM, which is modeled as a thin multiplicative optical element. Light propagates a distance of d_{SE} towards the eye-piece lens with a focal length of f_E, followed by another propagation for a distance of d_{EP} after which they reach the pupil plane, where an eyebox is formed around x_p. In the pupil plane, the point source's image replicas are created since part of the incident light is not modulated in most SLMs. Besides, diffraction orders of both modulated and unmodulated beams are formed by the SLM's pixelated structure. In this segment, we assume that since the separation between two consecutive diffraction orders is minimum for blue wavelength, the eyebox fits in the free region between the zeroth and first orders of the blue non-modulated beams. By moving from the eye-piece optics assembly, the rays propagate into the user's eye. (illustrated with a solid green box in Figure 2.6), modeled by matrix

$$\mathrm{M}_E = \begin{bmatrix} A_E & B_E \\ C_E & D_E \end{bmatrix}. \tag{2.38}$$

By using the SLM in color field sequential mode, we presume that full-color holograms are reconstructed. Using the correct parameters of the paraxial model for each wavelength to remove chromatic aberrations is vital. Chromatic aberrations result in lateral and axial shifts and size mismatches between color components if not handled correctly. Real lenses typically have slightly different focal lengths and principal planes for different wavelengths, which must be considered.

Figure 2.7 summarizes all the steps of the CGH computation algorithm.

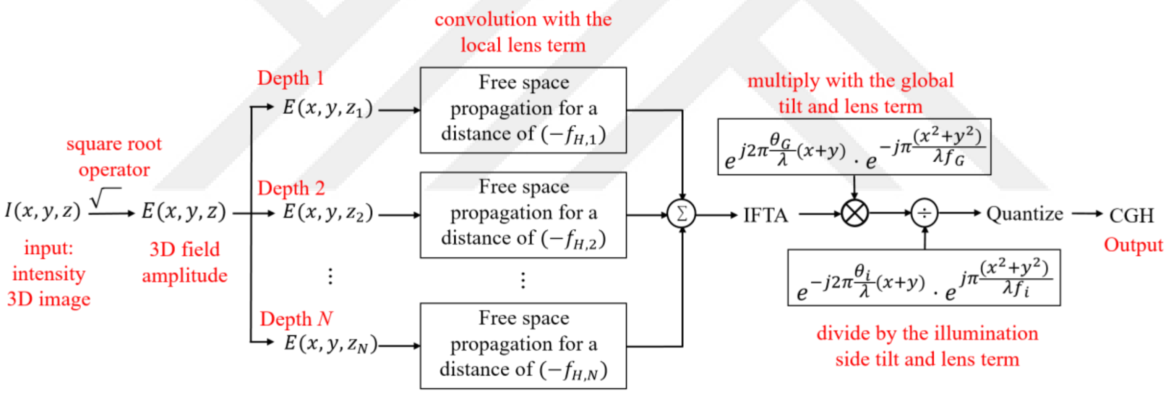

Figure 2.7 A summary of the steps of the CGH computation algorithm.

The proposed method starts with a 3D intensity image, i.e., a 2D image and a depth map ($I(x,y,z)$) rendered for a single viewpoint (x_p, the center of the eyebox). After taking the square root of the 3D intensity image ($I(x,y,z)$), the resulting 3D field amplitude ($E(x,y,z)$) is sliced into N planes (i.e., $z_1, z_2, \cdots, z_N$). The field amplitude at a distance of z_i (i.e., $E(x,y,z_i)$) is convolved with a lens term of focal length $f_{H,i}$ given as:

$$f_{H,i} = \left(\frac{A_E - z_i C_E}{B_E - z_i D_E} - \frac{A_E}{B_E}\right)^{-1} = \frac{(f_E(d_{EP} + d_{SE}) - d_{EP} d_{SE})^2}{z_i f_E^2}. \tag{2.39}$$

We calculate an intermediate field for each slice using an FFT-based free-space propagation for a distance of $-f_H$. Afterward, the intermediate fields of depth slices are superimposed. The computed full-complex hologram is encoded into a phase-only CGH. An alternative is to discard the field's magnitude information. Therefore, we use IFTA to compute phase-only

CGHs in this step. Finally, we superimpose global tilt and lens terms on the phase CGH to include the light source and eyebox locations. The global lens term has a focal length of

$$f_G = \frac{B_E}{A_E} = \frac{d_{SE}(f_E - d_{EP}) + d_{EP} f_E}{f_E - d_{EP}} \tag{2.40}$$

and the global tilt term has an angle (in radians) of

$$\theta_G = \frac{x_p}{B_E} = \frac{x_p f_E}{f_E d_{SE} + f_E d_{EP} - d_{SE} d_{EP}}. \tag{2.41}$$

The illumination lens term has a focal length of

$$f_i = \frac{B_I}{A_I} = \frac{d_{LI}(f_{IL} - d_{IS}) + d_{IS} f_{IL}}{f_{IL} - d_{IS}} \tag{2.42}$$

and the illumination tilt term has an angle (in radians) of

$$\theta_i = \frac{x_s}{B_I} = \frac{x_s f_{IL}}{f_{IL} d_{LI} + f_{IL} d_{IS} - d_{LI} d_{IS}}. \tag{2.43}$$

The lens and tilt terms' physical interpretations are provided as follows: the illumination lens and tilt terms convert the incoming illumination wave into a normally incident collimated plane wave. The resulted incident plane wave is imaged to the center of the eyebox with global lens and tilt terms. The lens term $f_{H,i}$ is added to the CGH so that instead of the pupil plane, the point light source is imaged on a plane at a distance z_i to the left of the pupil plane and forms a virtual object point there.

2.5 Simulations and experimental results

To verify the premises of the proposed methods, For the diverging beam and then converging beam illumination situations, we conducted proof-of-concept experiments.

2.5.1 Experiment 1: Diverging beam illumination using SLM

The experimental configuration is represented in Figure 2.8(a). SLM (Holoeye Pluto-VIS, 8-bit phase-only modulation in the 0-2π range, 1920 by 1080 pixels with a pixel pitch of 8 μm) is a reflective liquid crystal on silicon (LCOS). The point light source illuminating the SLM is a Gaussian beam diverging from the tip of a single-mode fiber coupled to a He-Ne laser source with a wavelength of 632.9 nm. A beam splitter combines the coherent light modulated and reflected by the SLM with real objects' incoherent light since the SLM is not transparent. The two dice were placed, respectively, 250 mm and 500 mm away from the eye. A camera captures the light in front of which an aperture of 3 mm in diameter is mounted to imitate the eye pupil. The distance is set to 60 mm between the aperture and the SLM. The distance between the point light source and the SLM is 250 mm. The effective eyebox is 4 mm x 4 mm square in this experiment. The system has 16.7 degrees diagonal FOV—two virtual text objects designed to appear next to each dice using a single phase-only CGH. Figure 2.8(b) and Figure 2.8(c) show the two images captured by the camera when the focus is adjusted on each of the two dice. The findings indicate that despite the lack of relay lenses, the SLM positioned far closer than the human eye's near point can provide focused retinal images. Besides, the system provides natural accommodation cues, and only when the eye focuses on the true depths can virtual objects appear in focus. We limited the laser power emanating from the single-mode fiber to <20 μW not to saturate the camera. The power captured by the camera inside the eyebox is around one microwatt, which is already very bright for the eye. The system is highly efficient in delivering light to the user's eyes, verifying that low-power HNEDs using low-power laser light sources are possible.

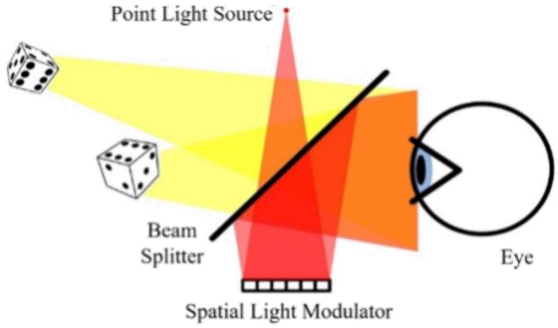

(a)

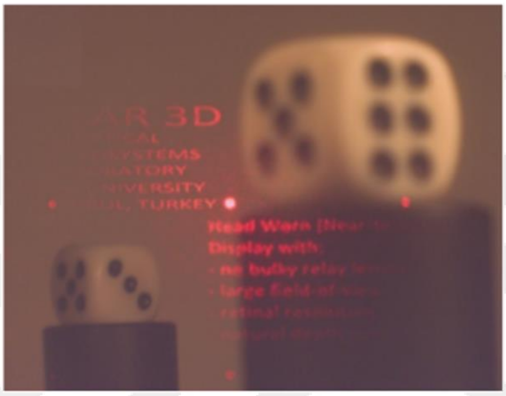

(b)

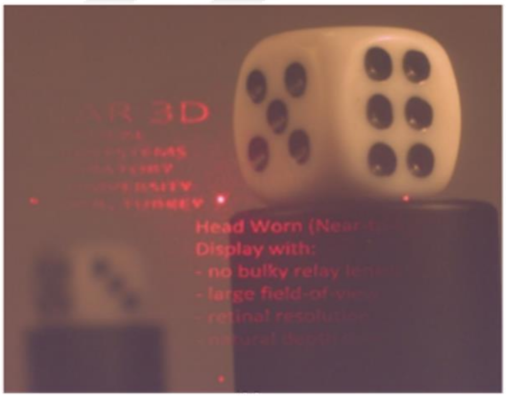

(c)

Figure 2.8 a) A not to scale setup of the first experiment. The distance from the eye to the SLM is 60 mm, while the distance from the point of light to the SLM is 250 mm. At 250 mm and 500 mm from the eye, respectively, are the nearby and far dices. Both of the dices have a 14 mm side length. To simulate the eye pupil, a 3 mm aperture is located in front of the camera. b, c) A camera image is captured when the lens is changed to 250 mm and 500 mm, respectively. The experiment confirms that 3D images with proper focus cues are shown without relay lenses, at retinal resolution. However, the images are degraded by the bright spots created by the SLM's un-modulated beam and the intensity variation due to SLM pixels' non-uniform directivity.

In addition to verifying the principles of the HNED solution, the first experiment also reveals two technical constraints linked to current SLMs. (Zhang, You, and D. Chu 2014): (i) Part of the light hitting the SLM stays unmodulated, creating mirror images of the point light source that are also captured by the camera and reduce the final image quality. (notice the bright spots in Figure 2.8(b) and Figure 2.8(c)), (ii) There is an intensity change of the images over the FOV, with dark bands near the edges. For the diverging beam case, Fourier transform of the pixel aperture results in Sinc^2 intensity profile across the reconstructed holographic image. The intensity variation can be minimized by adding an inverse brightness difference across the original image or limiting the SLM pixel reflector areas. The first problem is that inter-pixel gaps are not perfect absorbers, while the second problem occurs because the diffraction of SLM pixels around specular reflections is limited. As SLMs with smaller pixels become usable, both of these issues will be alleviated. The most apparent impact of the demonstrations in Figure 2.8 is that the distance of eye relief can be reduced to a distance shorter than 60 mm. (which is slightly impractical for near-to-eye configurations) with no sufficient pixel density of the SLM to support closer distances. The supportable eyebox size becomes smaller than the eye pupil for closer distances. In this case, unnecessary quantization noise, un-modulated and higher-order replica beams often reach the eye, corrupting the image resolution. Fortunately, LCOS-based SLMs with pixel pitches of 3.74 μm has already been demonstrated and are commercially available (Collings et. al., 2011; Bleha and Lei, 2013). The eye relief distance can then be reduced to about 30 mm.

2.5.2 Experiment 2: Diverging beam illumination using binary mask

A second experiment with a binary CGH printed on chrome on a glass mask with a minimum feature size of 2 μm and a total size of "20 mm" by "20 mm" is provided to prove the maximum potential of HNEDs. The mask is designed to function at a comfortable "20 mm" eye relief distance corresponding to a diagonal FOV of 70°. The effective eyebox in this experiment is 2.5 mm x 2.5 mm square. We placed a cell phone camera at the eye pupil location, as in Figure 2.9(a). Figure (b) shows the wide FOV image captured by the camera, while the images in Figure 2.9(c) and Figure 2.9(d) illustrate the details at different zoom levels. The smallest fonts correspond to 30 cycles per degree, and the total image comprises over 4000 by 4000 pixels. The high-quality image can also be seen with the naked eye.

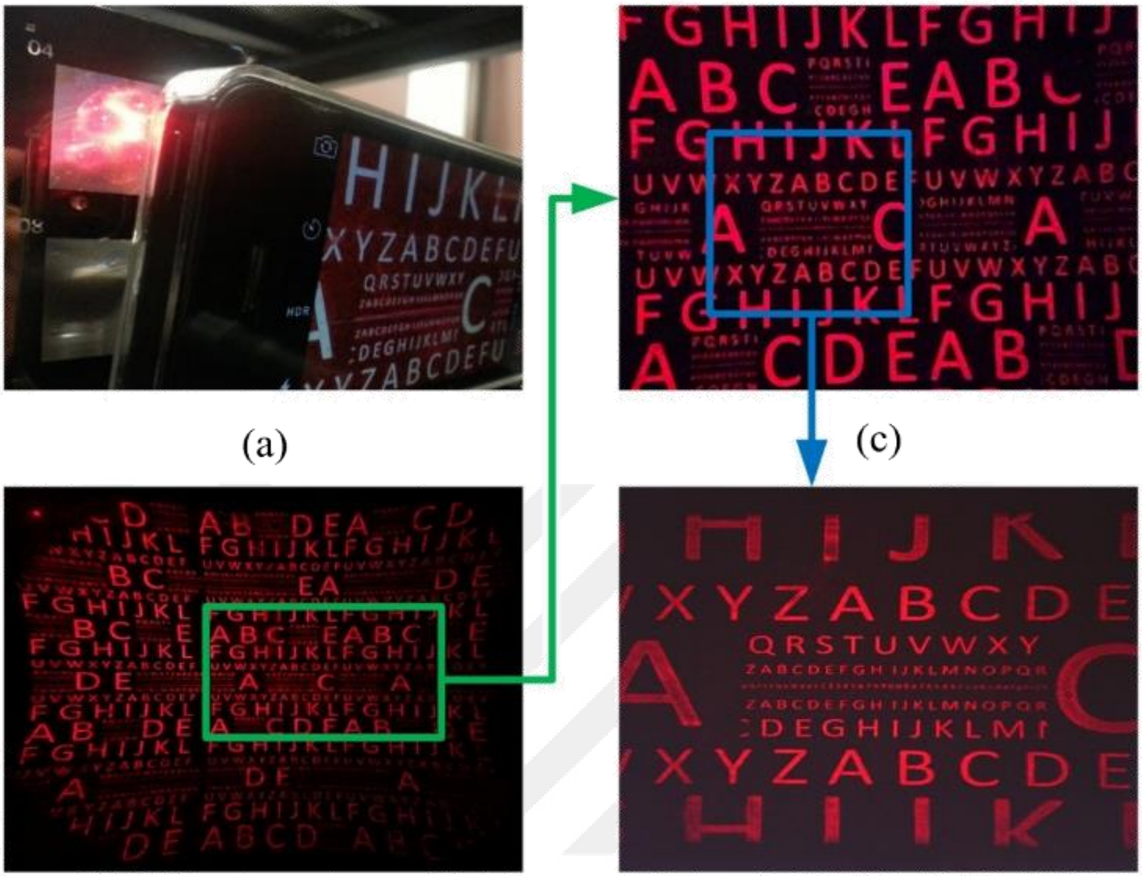

(a) (c)

(b) (d)

Figure 2.9 Results of the second experiment. a) 20 mm by 20 mm chrome on a binary glass mask placed 20 mm away from a cell phone camera. b) The camera sees the entire image with 70 degrees diagonal FOV. The FOV contains more than 4000 by 4000 pixels. c, d) Images at varying stages of zoom. The resolution of the smallest resolvable text is 30 cycles per degree.

2.5.3 Experiment 3: Converging beam illumination using SLM

Alternatively, as in the third experiment in Figure 2.10, the HNED architecture can be modified. The mere change is that the reflective SLM is mounted to a plano-convex lens with a focal length of 60 mm, and the point light source to SLM distance is set to 60 mm. A square region of 4 mm x 4 mm is the effective eyebox in this experiment. The system has a diagonal FOV of 16.7 degrees. The central point to consider here is that the lens is not supposed to act as a relay lens., but its primary purposes are (i) to concentrate the un-modulated beam to a region outside the eyebox (so that the eye pupil can filter it out), and (ii) to rotate the diffraction cones of SLM pixels to receives uniform power from each pixel on the eyebox. Therefore, the lens does not need to be free of aberrations and can be a simple single-piece lens, unlike the possibly the best relay lenses used in microdisplay-based approaches. The CGH computation procedure can easily accommodate lens aberrations. The loss due to the un-modulated beam and the variation in intensity is eliminated.

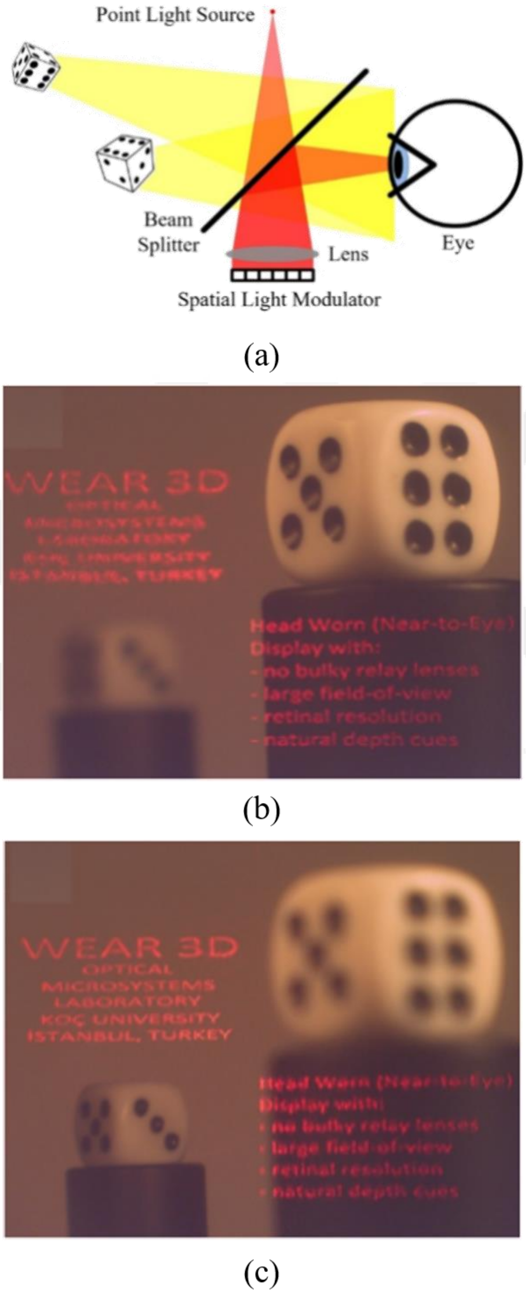

Figure 2.10 a) A not to scale schematic drawing of the third and fourth experiment setup. A plano-convex lens with a focal length of 60 mm is placed in front of the SLM. The light source is placed 60 mm away from the SLM. Other ranges, like the first experiment, are the same. b, c) Captured images by the camera show that the first experiment's artifacts are eliminated.

2.5.4 Experiment 4: Reconstruction of holograms with four depth planes

We used a 632 nm red He-Ne laser to reconstruct a hologram of a 3D computer-generated scene created utilizing Blender 3D.

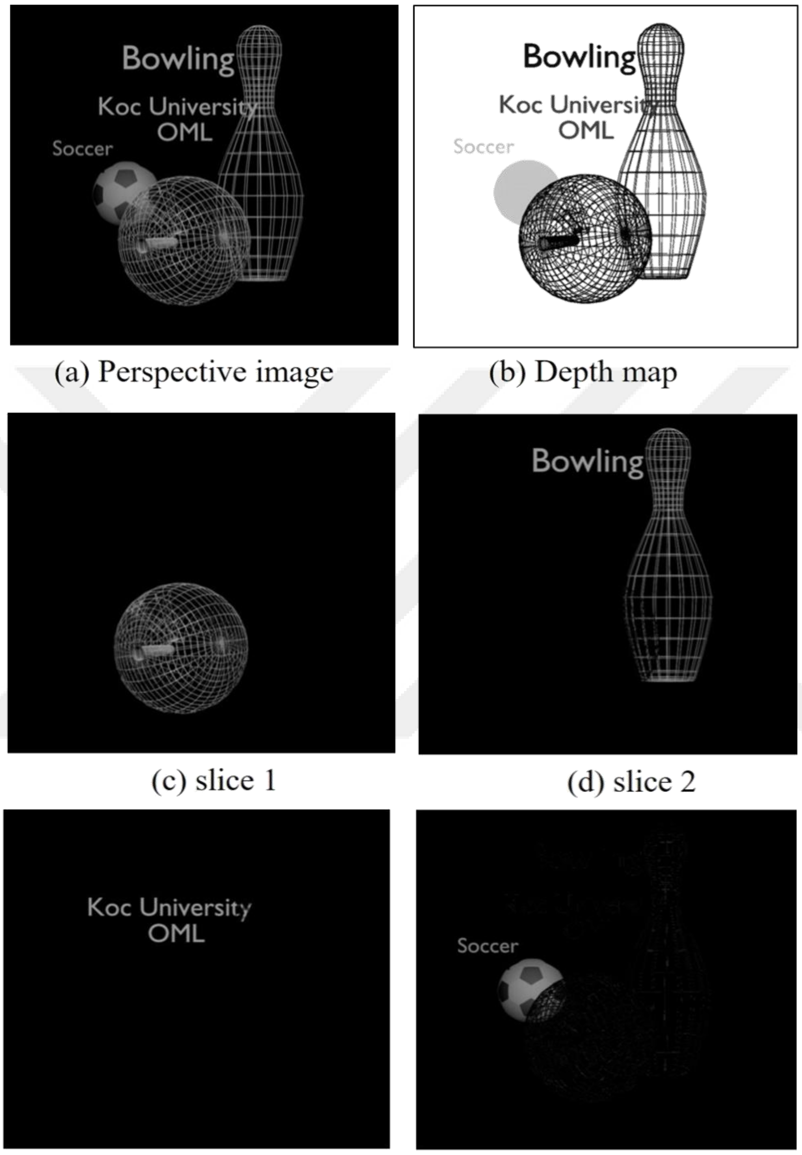

(a) Perspective image (b) Depth map

(c) slice 1 (d) slice 2

(e) slice 3 (f) slice 4

Figure 2.11 a) A screenshot of the 3D scene using Blender software. (b) The depth map image of the 3D scene rendered using Blender software. (c) The slice of the scene belonging to a distance of 4 diopters (25 cm). (d) The slice of the scene corresponding to a distance of 3 diopters (33 cm). (e) The slice of the scene corresponding to a distance of 2 diopters (50 cm). (f) The slice of the scene is related to a distance of 1 diopter (100 cm).

The scene in Blender, as shown in Figure 2.11(a), consists of a meshed bowling ball, a meshed bowling bottle along with a "Bowling" text on top of it, a "Koc University, OML" text, and a "Soccer" text soccer ball. These objects are respectively placed at a distance of 25cm, 33cm, 50cm, and 1m (1 diopter separation in between) from the pupil. The depth map image of the 3D scene created by Blender software is shown in Figure 2.11(b). The scene depth map (z-buffer) data allows us to obtain perspective views and the object's 3D location. The depth range is divided into four planes and the slices corresponding to the object planes, as shown in Figure 2.11(c)- Figure 2.11(f), respectively.

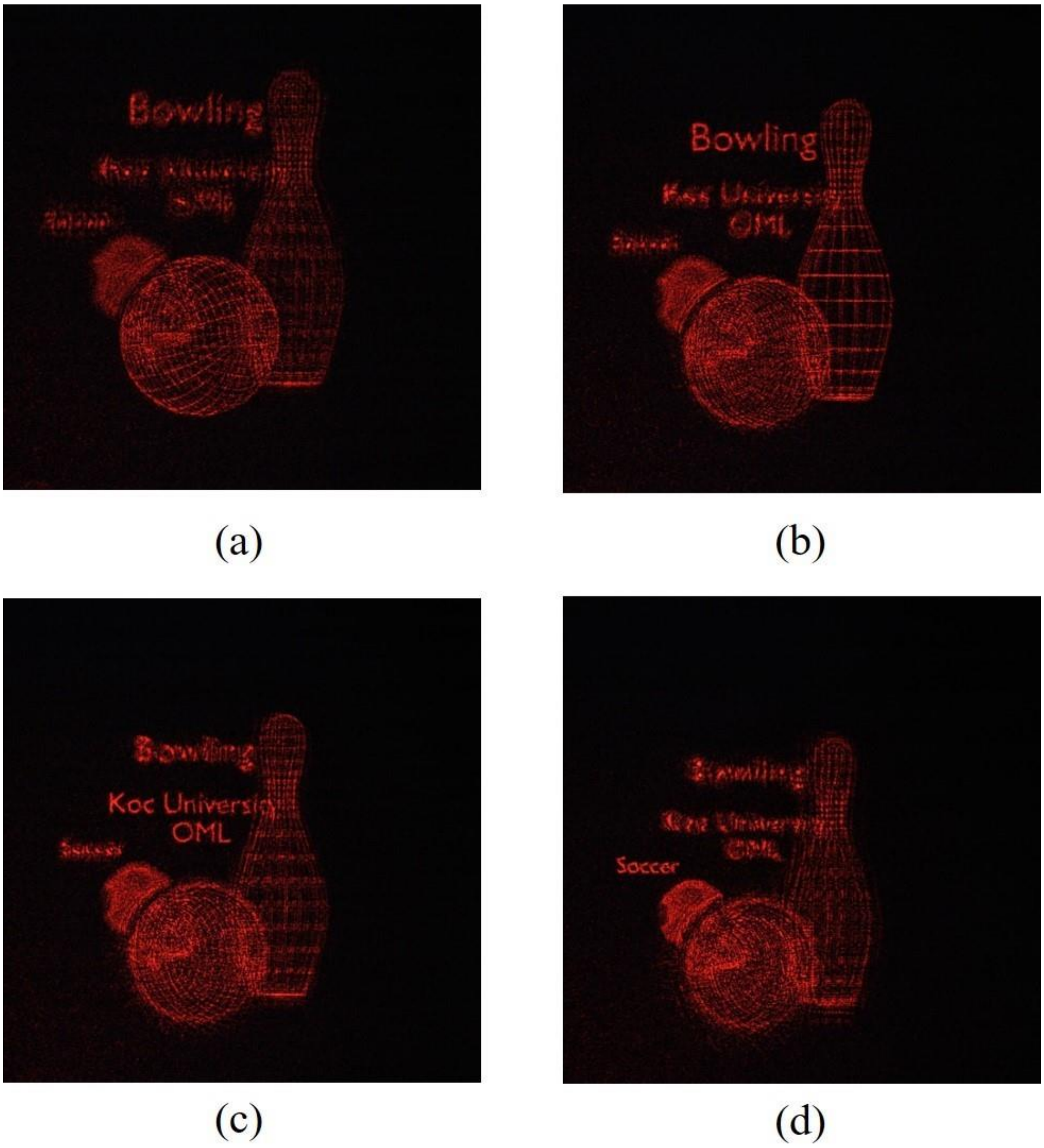

Figure 2.12 Experimental results and captured holograms (a) The camera is focused on four diopters (25 cm). (b) The focus of the camera is at three diopters (33 cm). (c) The focus of the camera is set to 2 diopters (50 cm). (d) The camera focus is set to 1 diopter (100 cm).

Figure 2.12 shows the experimentally captured holographic images. Figure 2.12(a)-

Figure 2.12(d) illustrate the reconstructed images where the camera focus varies from the first object to the last object, ranging from 25 cm to 100 cm, respectively. The results prove that the proposed technique is capable of providing both accommodation and occlusion cues. The effective eyebox size in this experiment is a square of 4 mm x 4 mm. The system has a diagonal FOV of 16.7 degrees.

2.5.5 Experiment 5: Converging beam illumination using SLM and speckle reduction

Since laser-based displays suffer from speckle noise, the use of a coherent laser light source could be seen as a fundamental limitation of the HNED method [Chellappan, Erden, and Urey, 2010]. First, we note that a perfect monochromatic illumination is not necessary for the device. Like many other holographic displays shown in the literature, it can operate under LED illumination. The LED source is partially coherent, i.e., sufficiently narrowband, and has a limited emission field. Indeed, at the expense of a small loss in resolution, the relatively low coherence of LED sources helps wash out the speckle patterns. Second, it is possible to obtain speckle-free and natural-looking retinal images using our computational methodology discussed in this thesis. An experimental result proving this idea is illustrated in Figure 2.13(a) and Figure 2.13(b). The image in Figure 2.13(a) suffers from speckle noise because of having an assigned random phase distribution to the virtual object points, which is the primary practice in most of the CGH algorithms. Furthermore, the image in Figure 2.13(b) is almost free of speckle due to the assignment of an optimized phase distribution computed using our proposed methodology. We point out that a small mismatch still exists between the simulated and the achieved images, which can be attributed to SLM pixels' crosstalk and other small artifacts from the optical components.

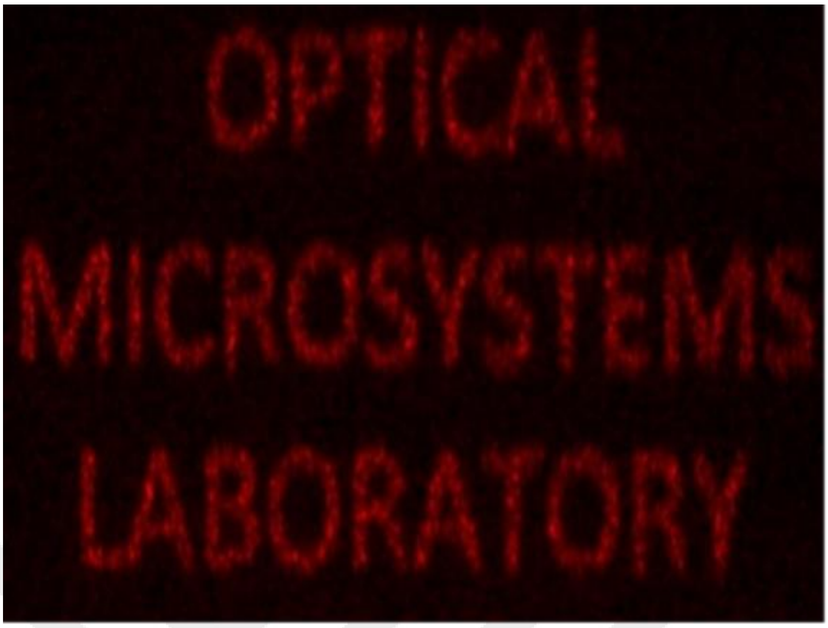

(a)

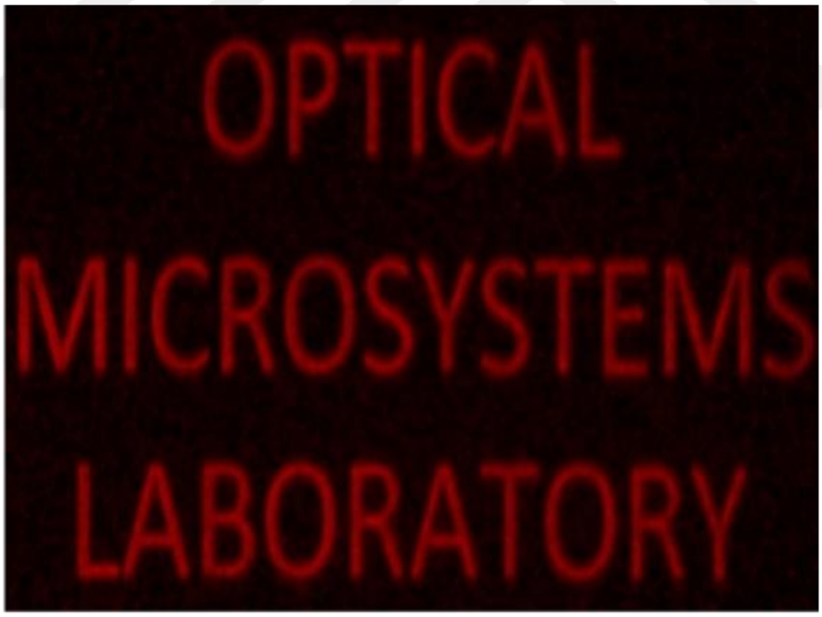

(b)

Figure 2.13 a) The speckle corrupted reconstructed holographic image of a virtual object with a random phase distribution. b) The speckle-free reconstructed holographic image of a virtual object with an optimized phase distribution verifies our methodology. It provides a solution to reduce the speckle artifact present in all laser displays.

2.5.6 Experiment 6: Full color with aberration correction using SLM:

We captured a full-color hologram using the same setup shown in Figure 2.10(a) as the last series of experiments with this setup. This experiment's effective eyebox is a square of size 3 mm x 3 mm (reduced due to wavelength scaling), and the diagonal FOV is 16.7 degrees. To reconstruct the full-color holograms, a time-division multiplexing technique is used. Single-mode fiber is used, where red, green, and blue lasers are coupled into that. To synchronize with the SLM's corresponding trigger signal, we used an Arduino to switch the lasers on and off sequentially. Using a 5 Mega-pixel JAI color sensor, the individual images of each red, green, and blue hologram are captured. We combined the captured images of each color into a single RGB image using MATLAB, and the results are provided in Figure 2.14 and Figure 2.15. The optical reconstruction of CGHs is based on the theory of diffraction, and chromatic aberration arises from various wavelengths. Reconstructed holographic images do not blend to form a full-color hologram without considering the right compensation factors. Neglecting the change of the refractive indices of the lenses to the wavelength, which can be compensated by the thick lens approximation in the CGH computation algorithm, is one of the critical causes of chromatic aberration. Figure 2.14(a) and Figure 2.14(b) shows the results when we do not utilize the thick lens approximations in our computation. As evident in the magnified views, the colors are separated. In Figure 2.14(a), the camera is focused at 25 cm, wherein in Figure 2.14(b), the camera's focus is set to 100 cm.

Figure 2.15(a) and Figure 2.15(b) demonstrates the experimental results of the captured correct full-color reconstructed holograms after applying proper corrections using thick lens approximation. Figure 2.15(a) shows that the camera is focused at 25 cm, and the magnified views provide the correct overlap. Similarly, a color-overlap is shown in Figure 2.15(b), where the camera focus is set to 100 cm.

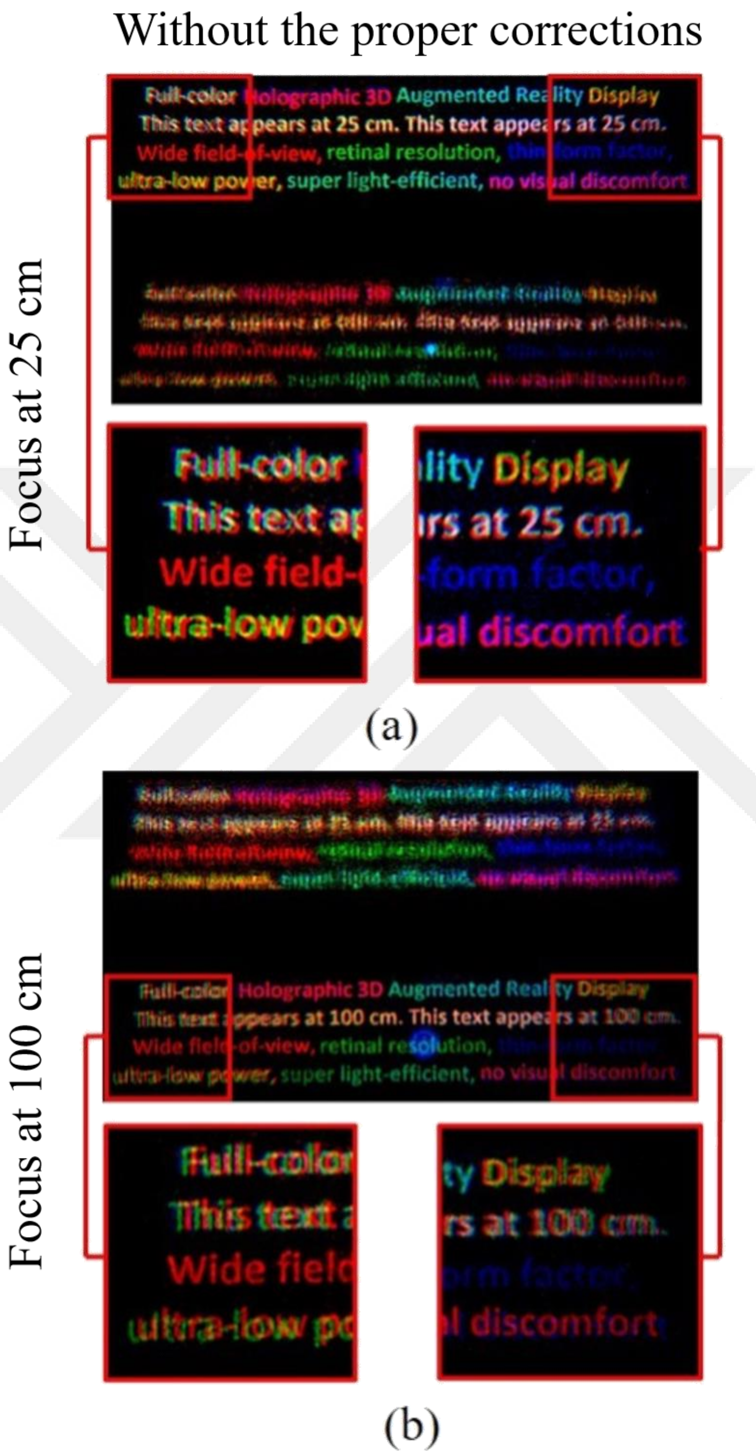

Figure 2.14 a, b) Experimentally captured full-color reconstructed holograms without the proper corrections. As seen in the magnified views, the colors are separated. The camera is focused at a distance of 25 cm in (a), and the focus of the camera is set to a distance of 100 cm in (b).

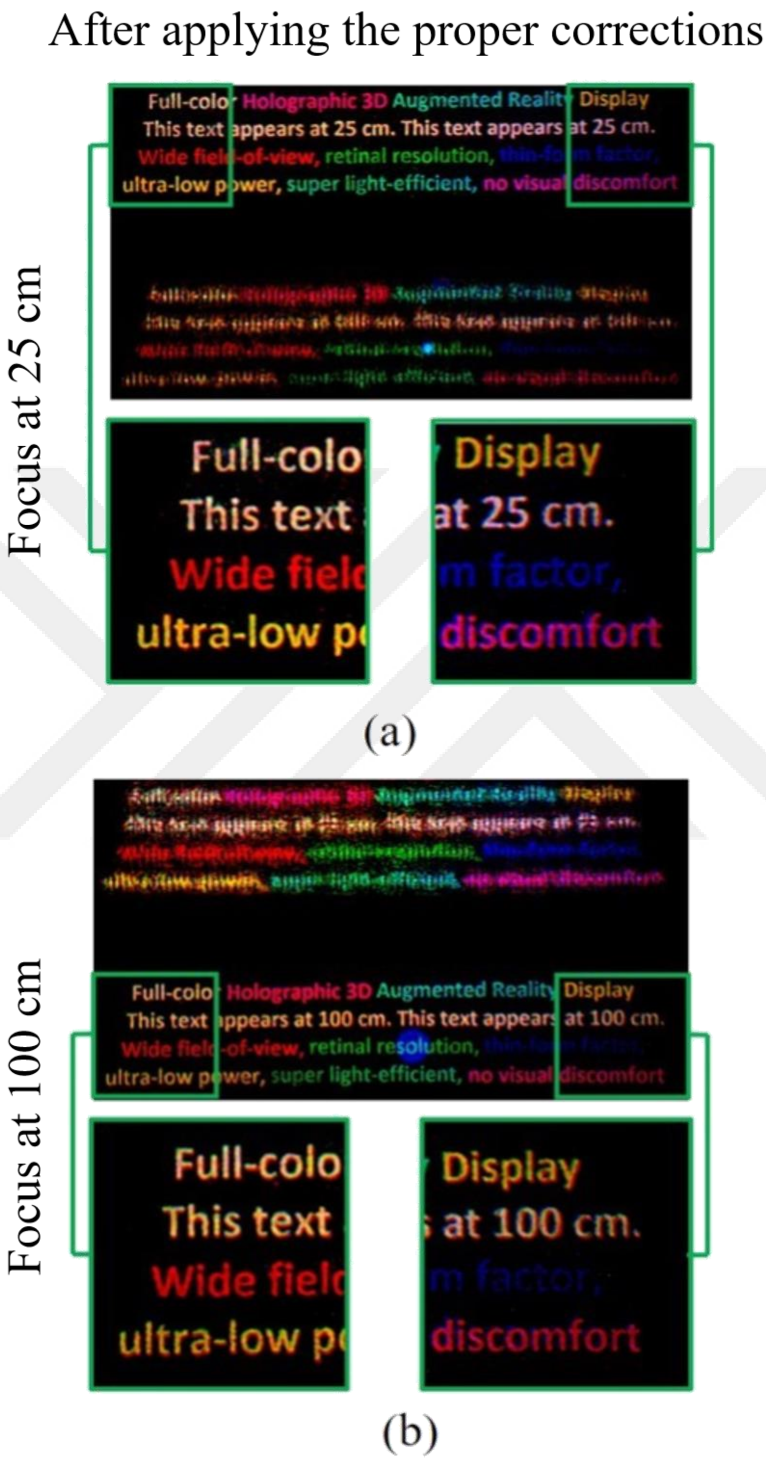

Figure 2.15 a, b) Correct full-color captured holographic reconstruction experimental results after applying proper corrections. The camera is focused at 25 cm, and the magnified views prove the correct overlap in (a). The color-overlap is evident in (b), where the camera focus is set at a distance of 100 cm.

2.5.7 Experiment 7: Designs with the same optical components and different FOVs

The proposed method is verified with optical experiments. The optical architectures of the experiments are shown in Figure 2.16. As shown in Figure 2.16(a), the light emits from a point light source and passes through a collimating lens of focal length f. The collimated light reflects toward the SLM after hitting the beam splitter surface. The modulated beams reflect from the SLM plane and propagate a distance to reach the eye-piece lens. The eye-piece lens focuses the light on the pupil plane. In these experiments, the pupil plane is placed on the focal plane of the eye-piece lens, and plane waves on the SLM plane get focused on the eye plane (i.e., Option 1 in Section 3). In some cases, the beam illuminating the SLM gets partly modulated, with an unmodulated beam traveling unaffected from the CGH on the SLM. It may be useful to image an unmodulated beam on the eye plane and filter it out by the user's pupil in such cases. This option also allows the collimated illumination of the SLM for positive values of focal length.

The HOLOEYE PLUTO spatial light modulator with 1920 by 1080 pixel resolution and an 8 μm pixel pitch is used in the experiments. We use a set of lenses that are f=100.3 mm in focal length. Figure 2.16(a) shows the architecture of the first experimental setup with a 10 degrees FOV. The distance between the SLM and the eye-piece lens must be 134 mm. The second experimental setup's architecture with a 20 degrees FOV is shown in Figure 2.16(c). The distance between the SLM and the eye-piece lens is calculated to be 573 mm. Additional imaging optics can design a more compact system suitable for a near-eye display [Cem et. al., 2020].

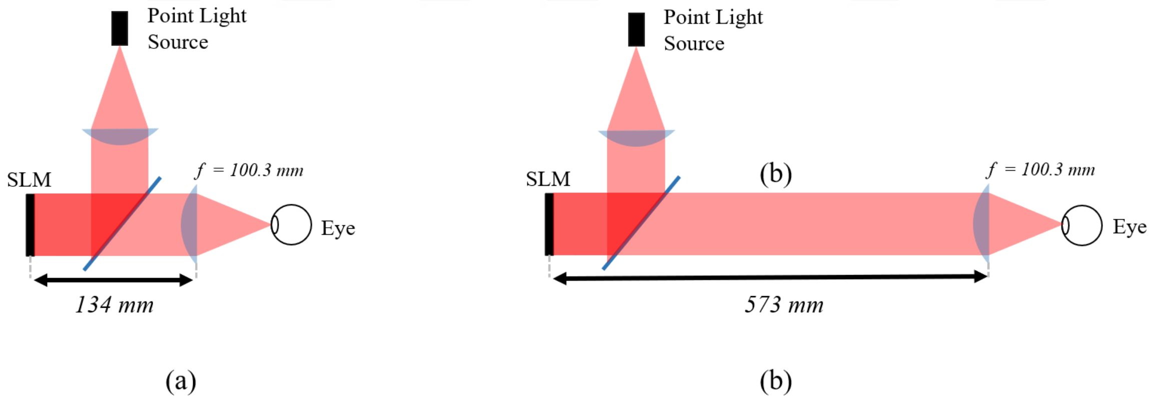

Figure 2.16 The optical architecture of the experiments. The virtual object point is placed at a distance of 500 mm from the eye. (a) The architecture of the first experimental setup with a 10 degrees FOV, where the distance between the SLM and the eye-piece lens must be 134 mm. (b) The architecture of the second experimental setup with a 20 degrees FOV, where the distance between the SLM and the eye-piece lens is calculated to be 573 mm.

The plots for the effective eyebox size versus the FOV is illustrated in Figure 2.17.

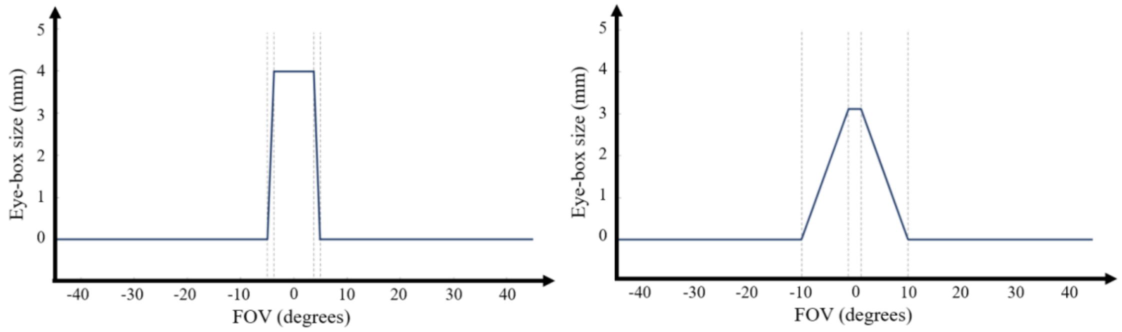

FOV	10 degrees
Maximum eye-box size	4 mm
SLM to the eye-piece lens distance	134 mm
Focal length of the eye-piece lens	100.3 mm

(a)

FOV	20 degrees
Maximum eye-box size	3.1 mm
SLM to the eye-piece lens distance	573 mm
Focal length of the eye-piece lens	100.3 mm

(b)

Figure 2.17 The plots for the effective eyebox size versus the FOV. (a) The plot corresponds to the architecture shown in Fig. 8(b) with a 10 degrees FOV. For this case, the maximum eyebox size is 4 mm, as reported in the table below the plot. (b) The plot for the architecture is shown in Fig. 8(c) with a 20 degrees FOV. For this case, the maximum eyebox size is 3.2 mm, as reported in the table below the plot.

Figure 2.17(a) corresponds to the architecture shown in Figure 2.16(a) with a 10° FOV. The maximum eyebox size is 4 mm, as reported in the table below the plot in Figure 2.17(a). Figure 2.17(b) belongs to the architecture shown in Figure 2.16(b) with a 20° FOV. The maximum eyebox size for this case is 3.2 mm, as reported in the table below the plot in Figure 2.17(b). As evident in Figure 2.17, the resolution of the image degrades as we move toward the edges of the FOV.

The simulation and experimental results for the architecture with a $\mathbf{10}^{\circ}$ FOV is shown in Figure 2.18(a) and Figure 2.18(b), respectively.

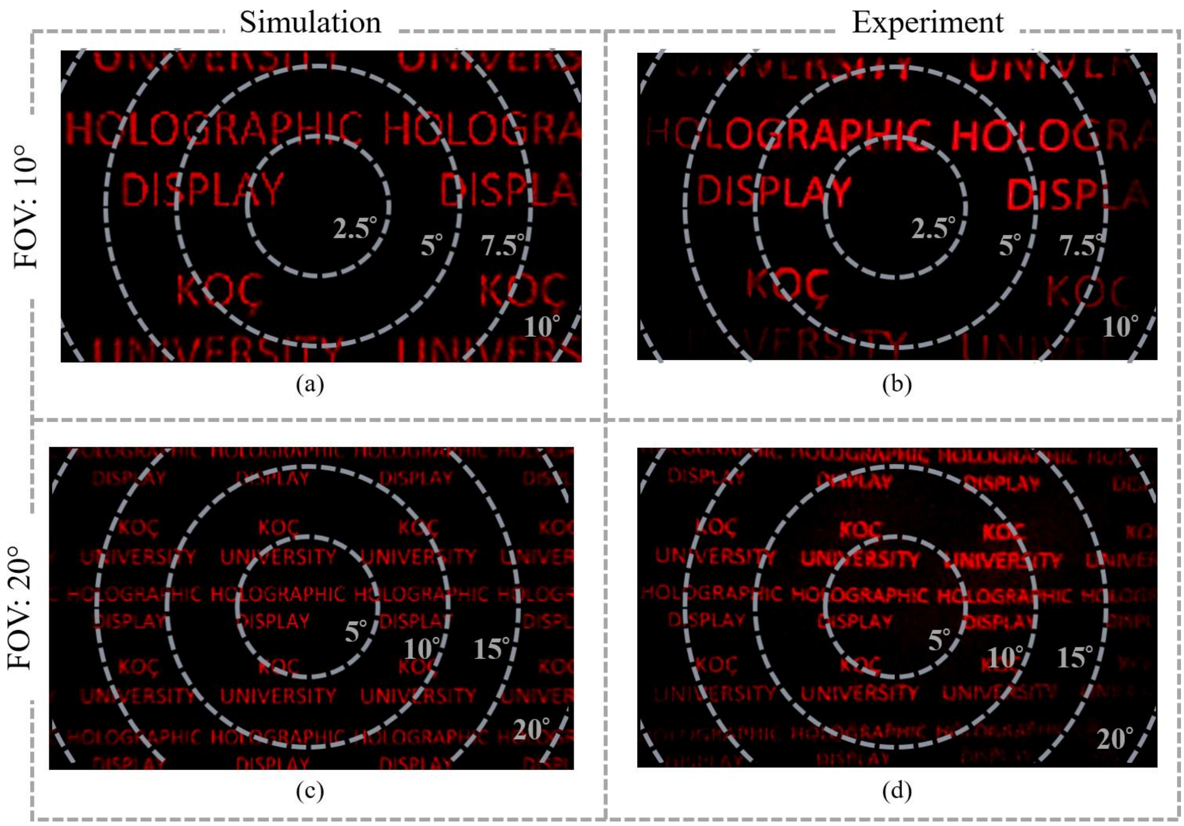

Figure 2.18 (a) The simulation results for the architecture with a 10 degrees FOV. (b) The experimental results for the architecture with a 10 degrees FOV. (c) The simulation results for the architecture with a 20 degrees FOV. (d) The experimental results for the architecture with a 20 degrees FOV.

The wavelength for both simulation and the experiment is chosen to be $\boldsymbol{\lambda} = \mathbf{632}$ nm. The simulation and experimental results for the architecture with a $\mathbf{20}^{\circ}$ FOV is shown in Figure 2.18(c) and Figure 2.18(d), respectively. As evident, the resolution of the images downgrades as we move toward the edges of the FOV. These experiments prove that given a set of parameters, we can design the optical architecture of the HNED for the desired FOV using the matrix-optics methodology explained in this chapter.

Chapter 3

COHERENCE ANALYSIS FOR HOLOGRAPHIC DISPLAYS

3.1 Introduction

The high coherency of the light source is vital for reconstructing high-quality holograms. A CGH must be illuminated with a monochromatic point light source to create the desired interference pattern on the image plane. A laser source coupled to single-mode fiber is the best practical light source option. However, using a laser source introduces several artifacts. The reconstructed image under the laser source illumination suffers from the speckle noise. Furthermore, the reflections from different surfaces of the optical system shape undesired fringe patterns and degrade the image quality.

One viable option to reduce speckle noise in holography is using a low temporal and spatial coherent source. Utilizing light-emitting diodes (LEDs) makes it possible to decrease the undesirable interference effects and speckle noise in HNEDs to a certain extent at the expense of reduced resolution. LED sources have a wider spectral range and a lower spatial coherence in comparison with laser sources. Besides, LEDs do not produce eye hazards, have ease of application, and small die size.

In this chapter, we proposed a straightforward analysis using matrix optics for investigating the effect of spatial and temporal coherence of LED sources on the resolution of HNEDs. The provided analysis helps us to optimize the optical architecture and minimize the side effects of utilizing LEDs. We experimentally investigated the spatial coherence of LED illumination with various pinhole sizes. Also, a He-Ne laser source coupled to single-mode fiber is used as a reference light source. Holograms of the USAF resolution target is reconstructed by utilizing LEDs and a laser source. Different configurations are studied by altering the position of the SLM and virtual object plane. For each configuration, the resolution of reconstructed images is analyzed by computing the contrast transfer function. Besides, we theoretically analyzed the effect of low-temporal coherence of LEDs. By optimizing the optical architecture, we obtained sharp and high contrast images using an LED light source.

3.2 Theoretical analysis

To model the effect of spatial and temporal coherence on a reconstructed hologram's quality, we assume that the SLM acts as a stack of diffractive optical lenses in principle. In this manner, an HNED becomes a diffraction-limited imaging system, which forms a light distribution in the space. An ideal imaging system performs a one-to-one mapping between object points (that is, the light source in an HNED) and image points. Within the context of an imaging system and coherent light illumination, two spatially separated pixels of a CGH form interference patterns on the virtual object plane. A model of a point light source emitting waves of different wavelengths is used to analyze the effect of temporal coherence. Waves with the same wavelength interfere and construct a pattern. The intensity patterns corresponding to different wavelengths will sum up and reshape the constructed image by imposing an envelope curve.

To analyze the effect of spatial coherence on the image quality, a partially-coherent light source with a finite extent is modeled as a collection of interfering point sources. These point sources generate almost identical and shifted interference fields on the image plane. The final image will summarize these interference patterns and degrades the image quality in most cases. The following analysis and simulations show that a light source's spatial and temporal coherence affects the reconstructed image's image quality. However, the effect of spatial coherence is much more apparent compared to the effect of temporal coherence. Furthermore, the following analysis provides a solution to avoid image quality degradation due to the absence of spatial coherence.

3.2.1 Spatial coherence analysis

The schematic of the optical system is shown in Figure 3.1.

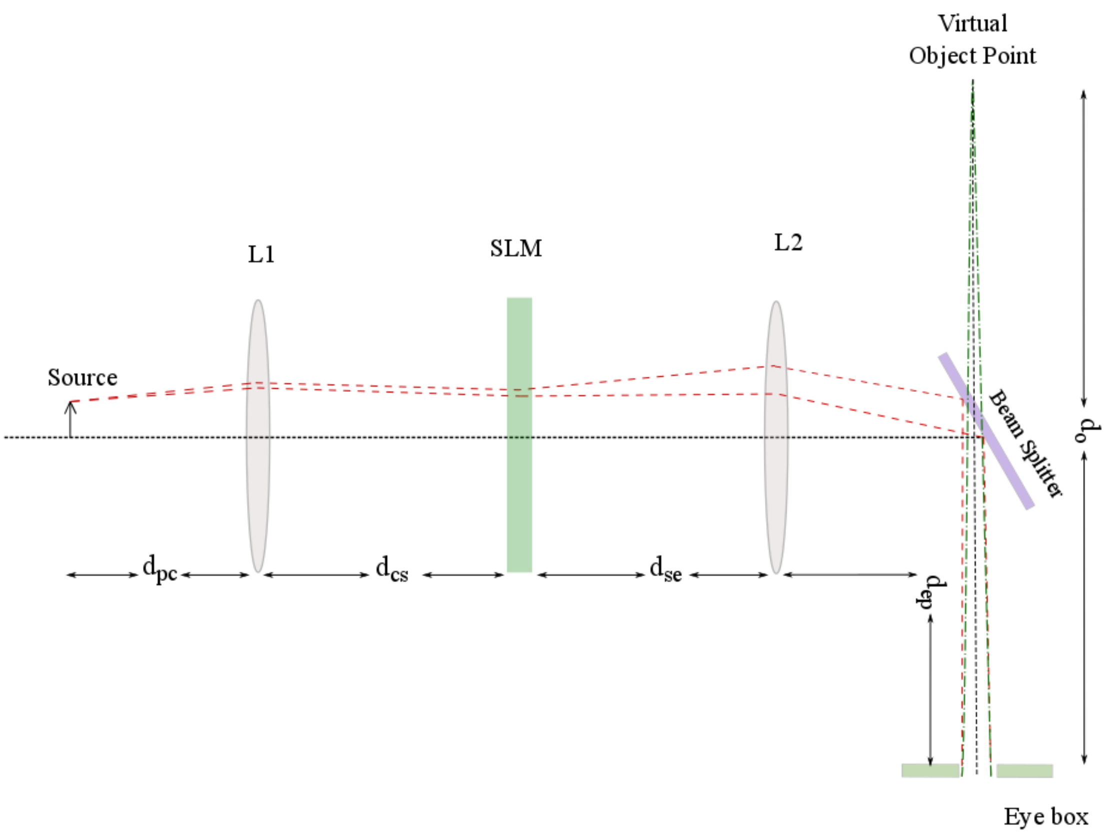

Figure 3.1 The schematic of the optical system. A collimated beam illuminates the SLM surface. A point source is imaged on the virtual object image plane.

This setup can be used as a near-to-eye display. The light emits from the source and travels a distance of d_{pc} and reaches the first lens of focal length f_c. The optical rays propagate a distance of d_{cs} and hit the SLM surface. Without loss of generality, we assume the SLM is transparent.

In experiments, we use a reflective SLM. The rays continue their path and hit the second lens of focal length f_e that is placed at a distance of d_{se} from the SLM. The eye-pupil plane is located at a distance of d_{ep}. To analyze the effect of spatial coherence on the image quality, a partially-coherent light source with a finite extent is modeled as a collection of interfering point sources. The optical system, shown in Figure 3.1, images the point source to a virtual object point at a distance of d_o from the pupil plane. The CGH is computed such that the SLM acts as a negative lens with a focal length of f_H. We use matrix optics to model the system mathematically. The relation between a point source of finite-extent x_s and the extent of the virtual object point x_o can be derived using the following equation:

$$\begin{bmatrix} x_o \\ \theta_o \end{bmatrix} = \begin{bmatrix} 1 & -d_o \\ 0 & 1 \end{bmatrix} \cdot \begin{bmatrix} 1 & d_{ep} \\ 0 & 1 \end{bmatrix} \cdot \begin{bmatrix} 1 & 0 \\ -1/f_e & 1 \end{bmatrix} \cdot \begin{bmatrix} 1 & d_{se} \\ 0 & 1 \end{bmatrix} \cdot \begin{bmatrix} 1 & 0 \\ -1/f_H & 1 \end{bmatrix} \cdot \begin{bmatrix} 1 & d_{cs} \\ 0 & 1 \end{bmatrix} \cdot \begin{bmatrix} 1 & 0 \\ -1/f_c & 1 \end{bmatrix} \cdot \begin{bmatrix} 1 & d_{pc} \\ 0 & 1 \end{bmatrix} \cdot \begin{bmatrix} x_s \\ \theta_s \end{bmatrix} = \begin{bmatrix} A & B \\ C & D \end{bmatrix} \cdot \begin{bmatrix} x_s \\ \theta_s \end{bmatrix}. \tag{3.1}$$

To have an imaging system, B must be equal to zero. From now on, we restrict the setup to ensure the consistency of analysis and experimental results. The setup uses a single lens of the focal length $f = f_c = f_e$. Because there is a single lens in front of the SLM, the distance between the SLM and the lens is equal to $d = d_{cs} = d_{se}$. Using the $B = 0$ condition, we find a solution for f_H:

$$f_H = \frac{f}{d_o}\left(f - d_o + \frac{d_o d}{f}\right). \tag{3.2}$$

Substituting f_H in the matrix equation above, we find a relation between x_o and x_s. The $x_o = Ax_s + B\theta_s$ the equation implies that:

$$x_o/x_s = A = d_o\left(\frac{1}{f} - \frac{f}{d_o} - \frac{d}{f^2}\right). \tag{3.3}$$

Using the equation above and simple trigonometric relations, the angular resolution of the reconstructed virtual object point can be written in the form of

$$\alpha = \left|\frac{x_o}{d_o}\right| = \left|x_s\left(\frac{1}{f} - \frac{1}{d_o} - \frac{d}{f^2}\right)\right|. \tag{3.4}$$

We define source-size factor (SSF) as

$$\mathrm{SSF} = \left|\frac{x_o/d_o}{x_s/f}\right| = \left|1 - \frac{f}{d_o} - \frac{d}{f}\right|, \quad 0 < \mathrm{SSF} < 1. \tag{3.5}$$

SSF indicates the contrast and the quality of the images, where lower SSF values introduce reconstructions with higher resolution and quality. If SSF=0, the source size does not impact the resolution of the virtual image. The SSF=1 case implies that to display high-quality images, and the source must have zero extend, i.e., the source must have full spatial coherence.

3.2.2 Angular resolution simulations

The optical structure in Figure 3.1 can be considered as a near-to-eye display. Figure 3.2 shows the simulation results of the angular resolution in arcmin units with respect to the virtual object point distance d_o. For simulation purposes and consistency with the experiments, we set $f = 100mm$. Figure 3.2(a) to Figure 3.2(c) illustrate the results of the simulation for three light sources with sizes of $54\ \mu m$, $107\ \mu m$, and $205\ \mu m$, respectively.

We choose five values for the SLM to lens distance (d) of $20\ mm$, $40\ mm$, $60\ mm$, $80\ mm$, and $100\ mm$, differentiated with various line colors in each plot of Figure 3.2. The values for d_o vary between $250mm$ and $1000mm$, which is a logical range for a near-to-eye display. The results in Figure 3.2 indicate that using an extended light source with partial spatial coherence, the system can reconstruct high-quality virtual images by choosing the right distance between the SLM and lens. The acceptable value for the angular resolution is one arcmin, which is the human eye resolution limit.

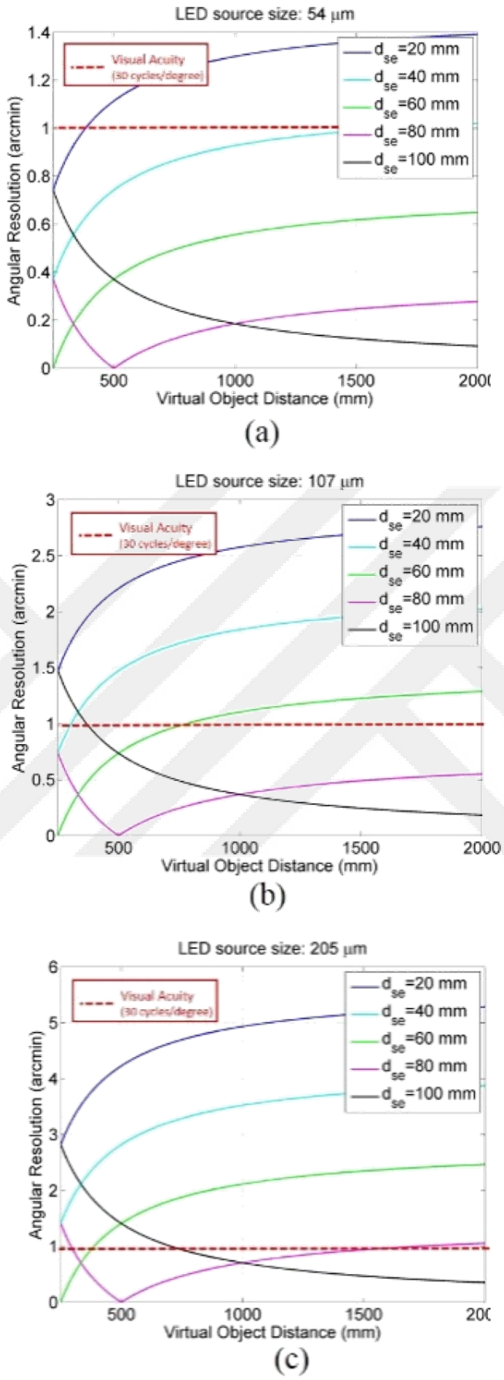

Figure 3.2 Simulation results of the angular resolution with respect to the virtual object point distance. Figures (a) to (c) illustrate the results of simulating for three light sources with sizes of $54\mu m$, $107\mu m$, *and* $205\mu m$, *respectively. In each plot, values for the SLM to lens distance of* $20mm$, $40mm$, $60mm$, $80mm$ *and* $100mm$ *are differentiated with different line colors. The red dashed line indicates the acceptable value for the angular resolution of the human's eye.*

3.2.3 SSF analysis

The SSF values are evaluated, assuming that $f = 100mm$. We choose three distances of $250mm$, $500mm$ and infinity for the virtual object distance d_o. For each d_o, we compute the SSF for five SLM-to-lens distances (d) of $20mm$, $40mm$, $60mm$, $80mm$ and $100mm$. We classified different configurations with the same SSF value into five groups, where group 1 corresponds to the SSF value of 0 and group 5 represents configuration with an SSF of 0.8. Configurations with lower SSF values provide high-quality reconstructions of holograms. These classifications are used in reporting the experimental results.

3.2.4 Temporal coherence analysis

We are using an LED source with a central wavelength of $632nm$. The bandwidth of the LED is $20nm$ FWHM. Figure 3.3 represents the spectrum of the LED.

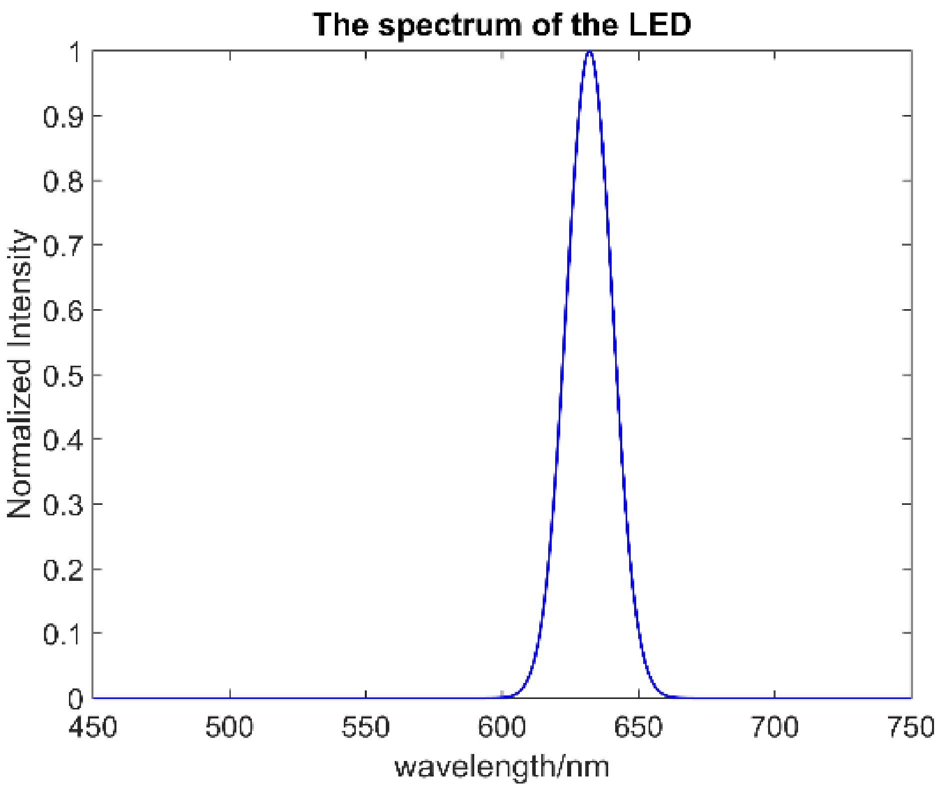

Figure 3.3 Spectrum of the LED source. The central wavelength of LED is $632nm$. The bandwidth of the LED is $20nm$ FWHM.

To analyze the effect of the temporal coherence on the image quality, we performed the following simulation: a CGH is computed for a central wavelength of $632nm$. The optical architecture for computing and reconstructing the hologram is chosen to have an SSF value of zero. The following simulations are performed assuming that the distance between the SLM and the lens is $100mm$ and the virtual object distance is $500mm$. The computational reconstruction of the CGH with a coherent light illumination is shown in Figure 3.4(a). This pre-computed CGH is illuminated with 41 different wavelengths ranging from $622nm$ to $642nm$, with a linear increment of step size $0.5nm$. The weighted average of reconstructed holograms (based on the intensities provided in Figure 3.4) results in Figure 3.4(b). As evident in Figure 3.4, reducing the temporal coherence of the light source distorts the reconstructed image. However, the loss of spatial coherence degrades the image sharpness and quality more severely.

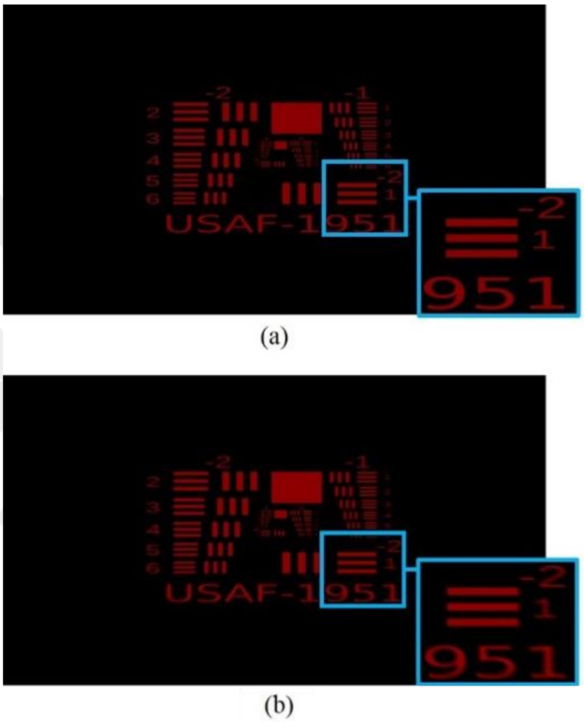

Figure 3.4 Simulation results of the temporal coherence effect on the image quality. (a) Simulation with temporally coherent light illumination. (b) Simulation result of an LED illumination for architecture with $d = 100\ mm$ and $d_o = 500\ mm$.

3.3 Experimental setup

The optical system is shown in Figure 3.5. A collimation lens collimates a point source. Rays hit the SLM surface and reflect and pass through the same lens. The rays reach a beam-splitter. We use an eye-piece lens and a CCD camera to capture the reconstructed holograms and model the human eye. In the experiments, we use HOLOEYE PLUTO SLM with a resolution of 1920×1080 pixels and $8\ \mu m$ pixel pitch. All results are monochrome, and we perform experiments with two different light sources. For the case of a coherent light source, we utilize a He-Ne red laser of wavelength $632.9\ nm$ coupled into a single-mode fiber. For the case of a partially coherent light source, we use a red LED source with a central wavelength at $632\ nm$ and a spectral width of $20\ nm$ FWHM combined with $54\ \mu m$, $107\ \mu m$, and $205\ \mu m$ pinholes.

We use phase-only CGHs to reconstruct the holograms optically. In this respect, the full-complex CGH should be encoded into a phase-only CGH. An option is to neglect the magnitude information of the full-complex hologram. However, this option will not produce a high-quality image. Therefore, we use the well-known iterative Fourier transform algorithm (IFTA) to compute phase-only CGHs.

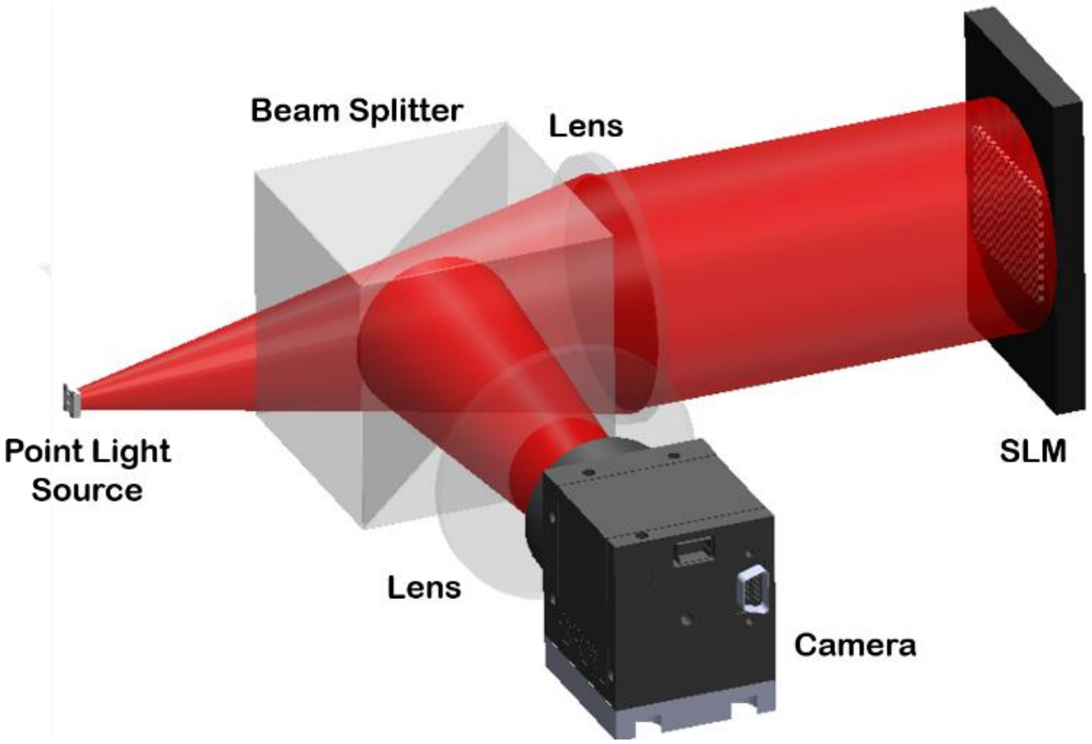

Figure 3.5 A point source is collimated by a collimation lens. Then rays hit the SLM surface and reflected, pass through the same lens (Fourier lens), and reaches a beam-splitter. After passing through the beam-splitter a diaphragm and an eyepiece, an image forms on a CCD camera.

3.4 Experimental results

We investigated the resolution of the reconstructed image using various sources. First, the image of the USAF resolution target is reconstructed by a He-Ne laser source of wavelength $632.9nm$. Then, LEDs combined with different pinholes are used to reconstruct the USAF resolution target images. Each light source is used in 15 different configurations of table 1, and we obtained 60 images. We classified the captured images into five groups based on SSF values of table 1. Figure 3.6 illustrates the experimental results for group 1 with an SSF value of 0. We can see that the LED source with different pinhole sizes and the laser source provide images of the same contrast. The captured holograms of configurations in group 2 are shown in Figure 3.7, where the SSF value is 0.2. Images in Figure 3.7 have a lower contrast compared to the ones from group 1. However, the reconstructed holograms of group 2 have better contrast than groups 3 to 5. The images related to group 3, with an SSF value of 0.4, are provided in Figure

3.8. As seen in Figure 3.9, the resolution of images of group 4 with an SSF value of 0.6 starts to decrease sharply. Finally, in Figure 3.10, the reconstructed holograms of group 5 with an SSF value of 0.8 are shown. As evident, the images' resolution in group 5 is getting worse than the previous configurations.

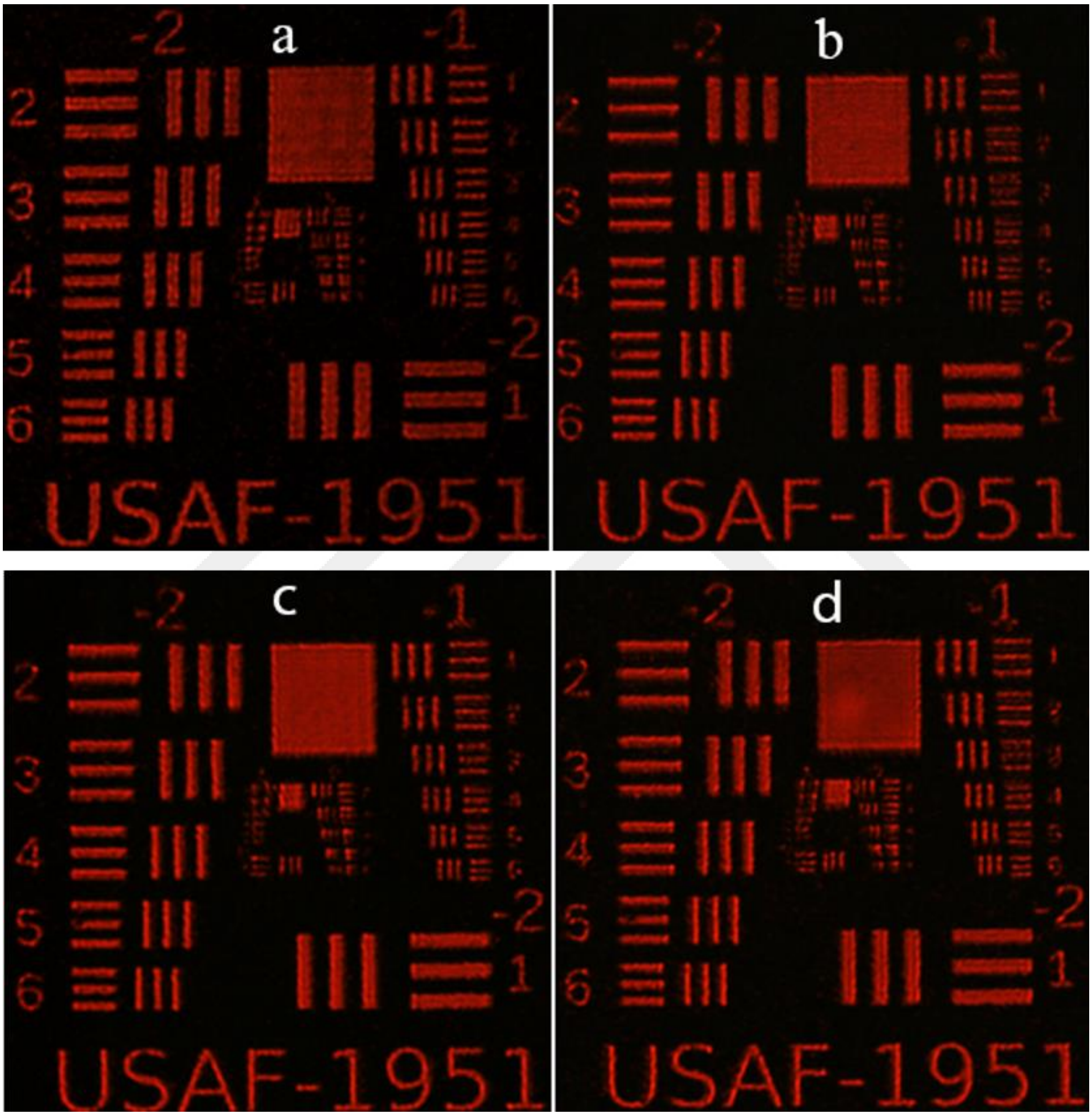

Figure 3.6 Group one ($SSF = 0$), SLM to lens distance is $100mm$, and the virtual object is at infinity for a) Single-mode coupled laser source b) LED with $54\mu m$ pinhole c) LED with $107\mu m$ pinhole d) LED with $205\mu m$ pinhole.

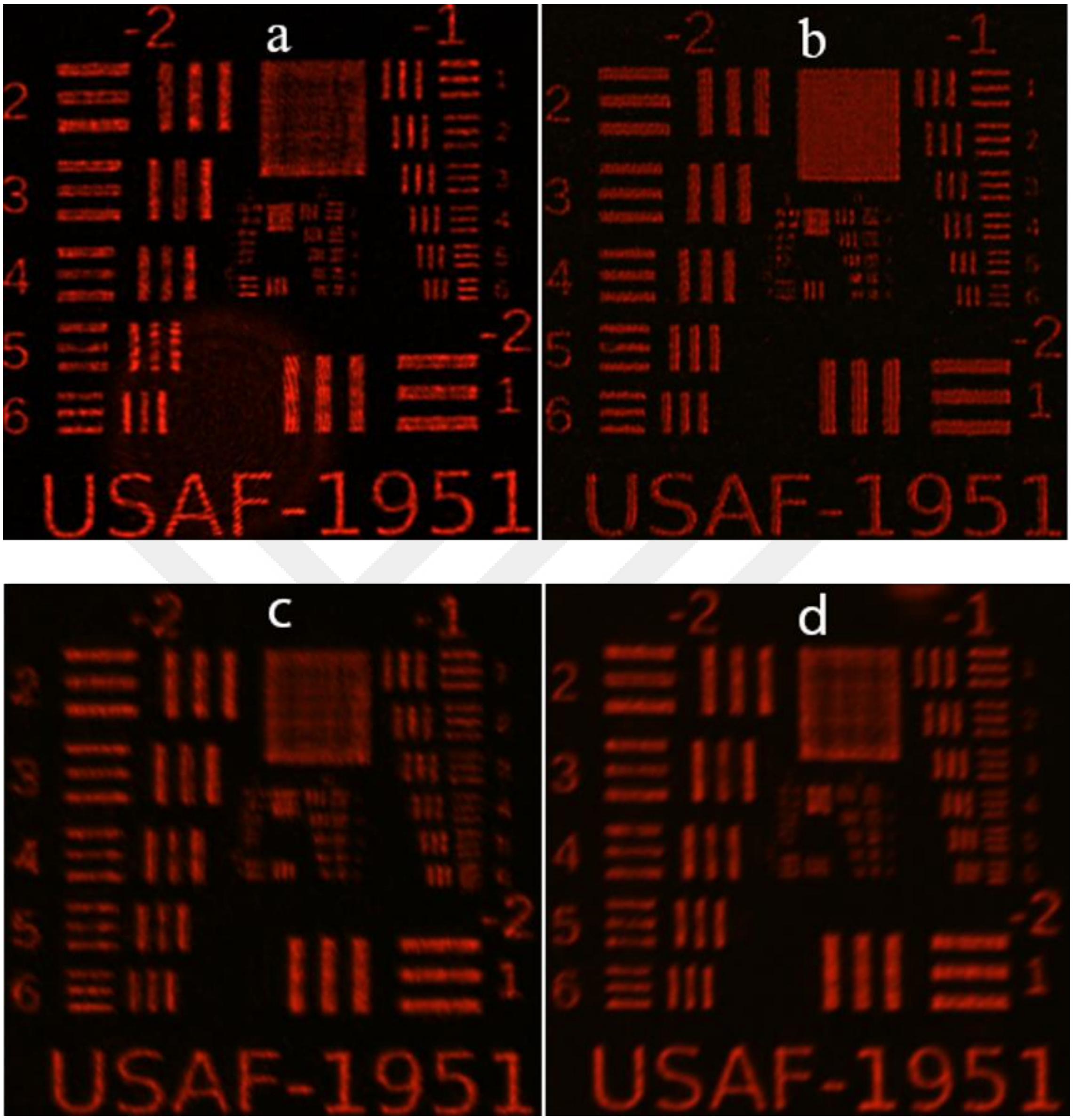

Figure 3.7 Group two (SSF $= 0.2$*), SLM to lens distance is* $80mm$*, and the virtual object is at* $500mm$ *for a) Single-mode coupled laser source b) LED with* $54\mu m$ *pinhole c) LED with* $107\mu m$ *pinhole d) LED with* $205\mu m$ *pinhole.*

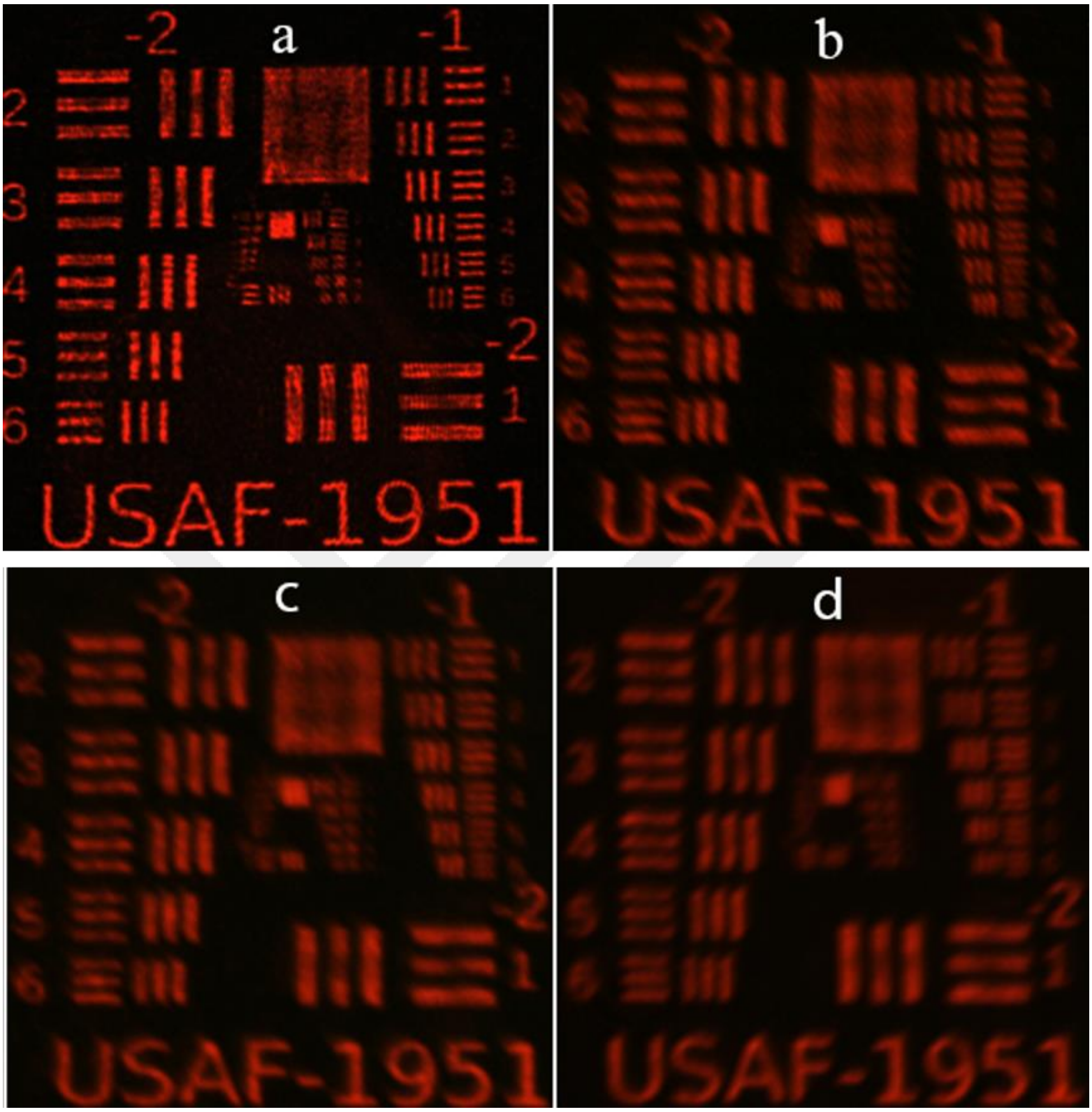

Figure 3.8 Group three (SSF $= 0.4$*), SLM to lens distance is* $60mm$*, and the virtual object is at infinity for a) Single-mode coupled laser source b) LED with* $54\mu m$ *pinhole c) LED with* $107\mu m$ *pinhole d) LED with* $205\mu m$ *pinhole.*

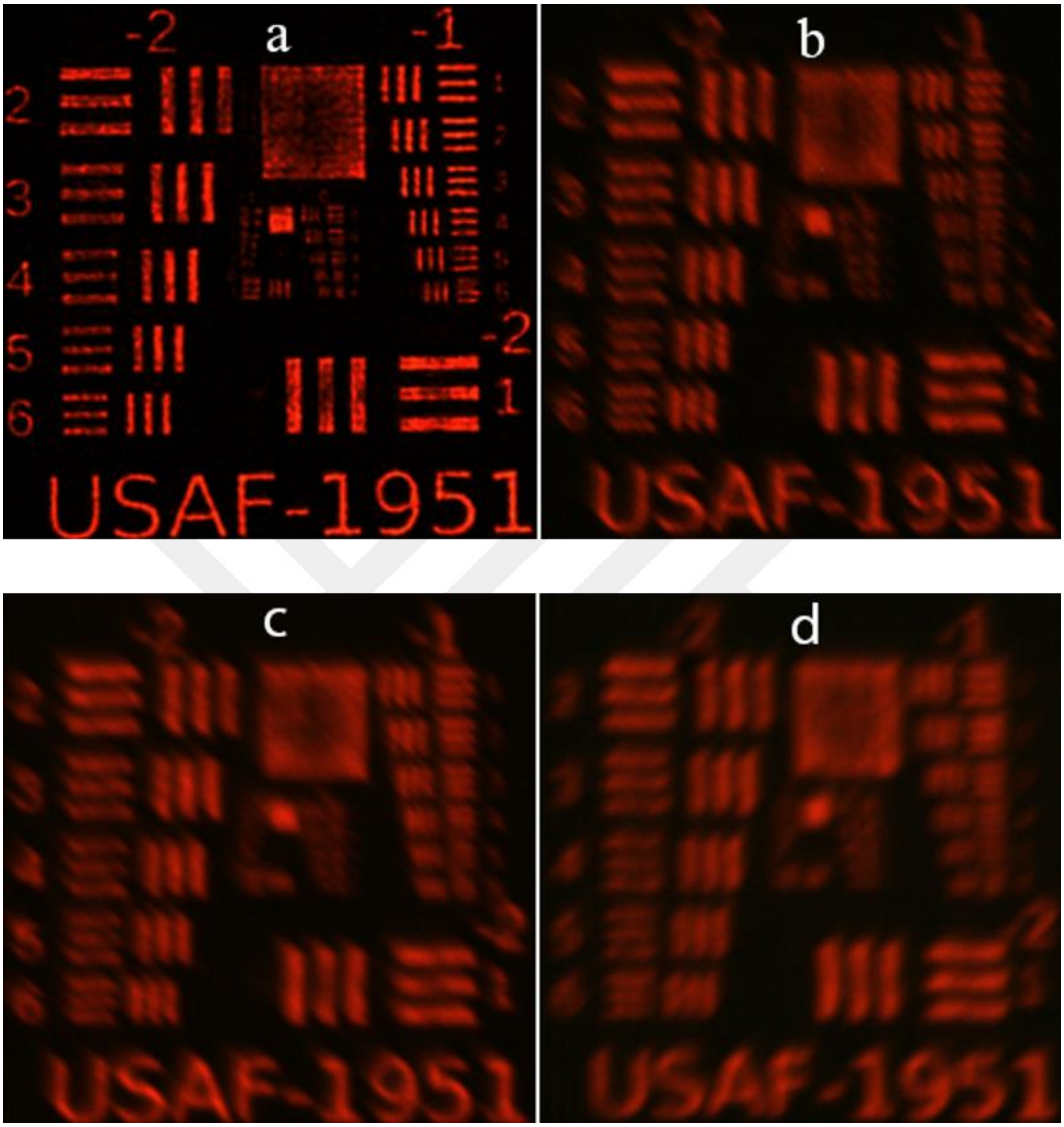

Figure 3.9 Group four ($SSF = 0.6$), SLM to lens distance is $40mm$, and the virtual object is at infinity for a) Single-mode coupled laser source b) LED with $54\mu m$ pinhole c) LED with $107\mu m$ pinhole d) LED with $205\mu m$ pinhole.

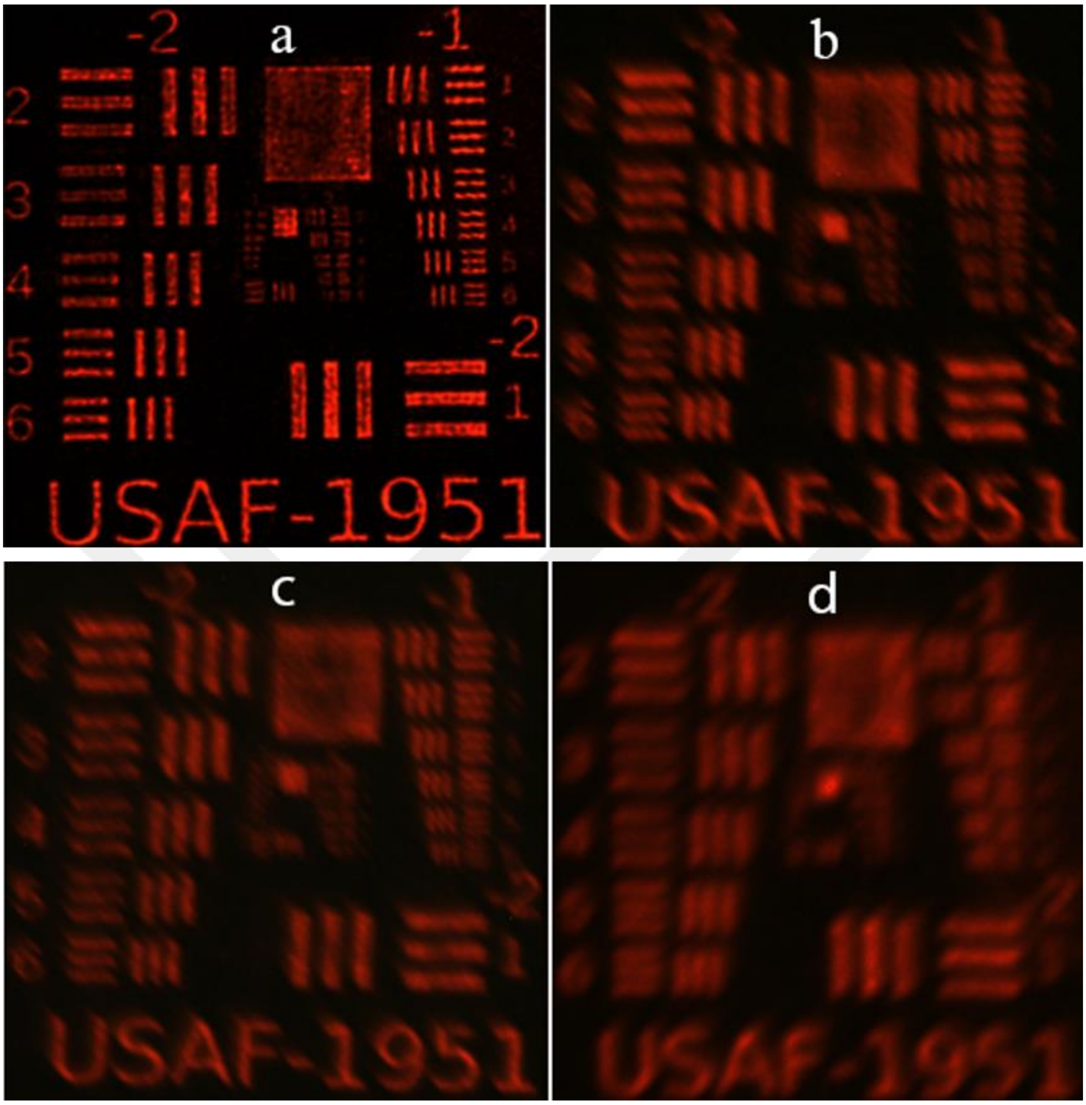

Figure 3.10 Group five ($SSF = 0.8$), SLM to lens distance is $20mm$, and the virtual object is at infinity for a) Single-mode coupled laser source b) LED with $54\mu m$ pinhole c) LED with $107\mu m$ pinhole d) LED with $205\mu m$ pinhole.

We plot the contrast transfer function (CTF) of six specified spatial frequencies on the USAF resolution target for each configuration, as shown in Figure 3.11. The CTF is computed by dividing the maximum and the minimum intensity values by their summation.

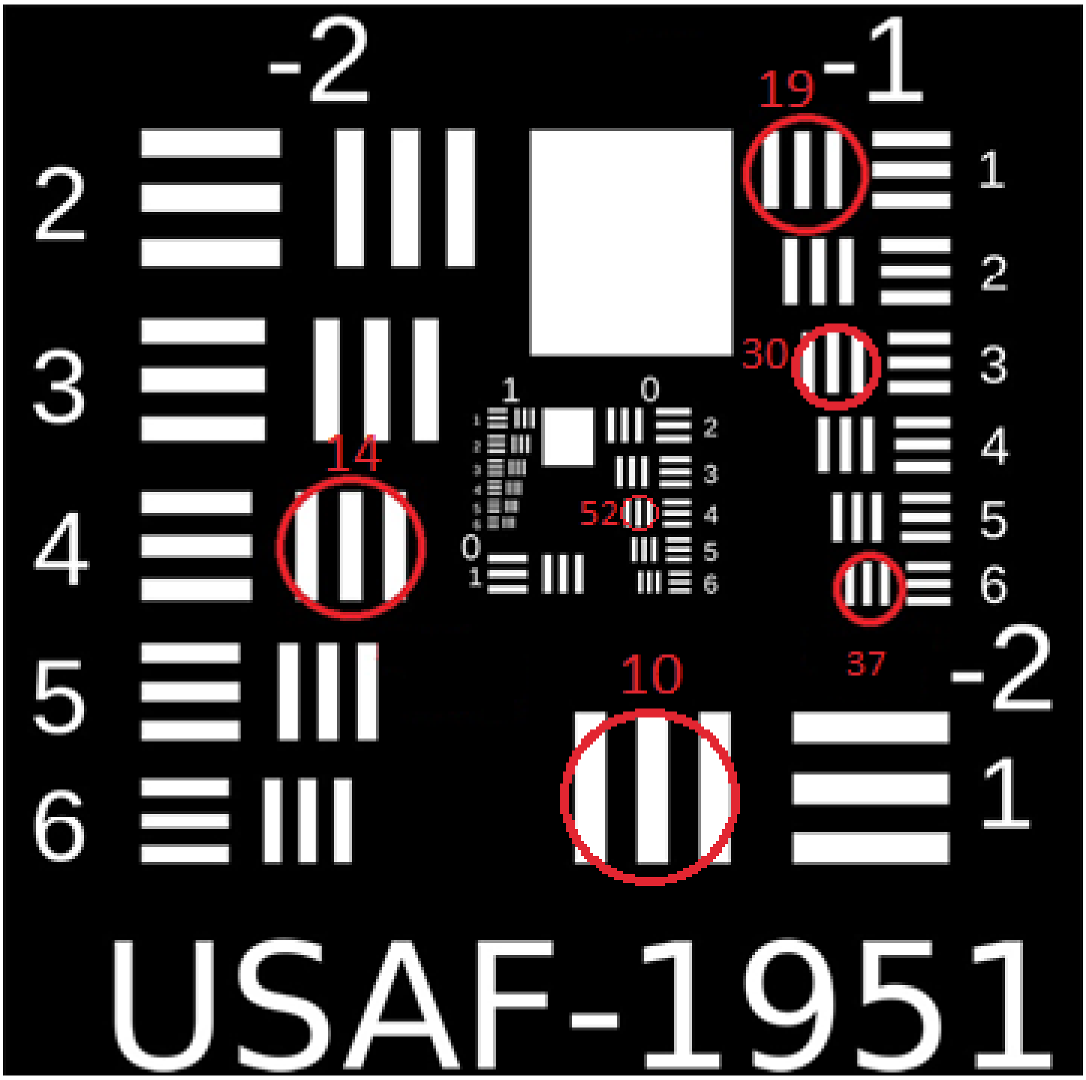

Figure 3.11 Different spatial frequencies on the USAF target. Red circles indicate spatial frequencies including 10, 14, 19, 30, 37, *and* 52 *cycles/degree.*

In each plot of Figure 3.12, the vertical axis shows the contrast, and the horizontal axis indicates the spatial frequency in cycles per degree unit. The contrast values for different groups are shown with different line colors. Figure 3.12(a) illustrates the contrast value for the case of laser illumination. As expected, even in high spatial frequencies, the contrast is high for all groups. We can deduct from Figure 3.12(b) to Figure 3.12(d) that in all LED sources, when the SSF value is equal to zero (corresponds to group 1), the contrast is as high as the laser case even in high spatial frequencies. The virtual object is placed at the SLM image plane in group 1. We observe that using configurations with SSF= 0 values (i.e., group 1 members), we can reconstruct sharp images regardless of the light source's spatial incoherence. For groups 2 to 4, the contrast decreases. In configurations that are categorized as group 5, the contrast is the worst. We expect this degradation in the image resolution because the distance of the reconstructed hologram plane and the SLM image plane are the largest in this case. Figure 3.12 shows that for SSF values of 0.2 to 0.8, increasing the LED emission area degrades the contrast. For a given configuration, larger source sizes lead to faster degradation in spatial resolution. These results are in agreement with the analysis.

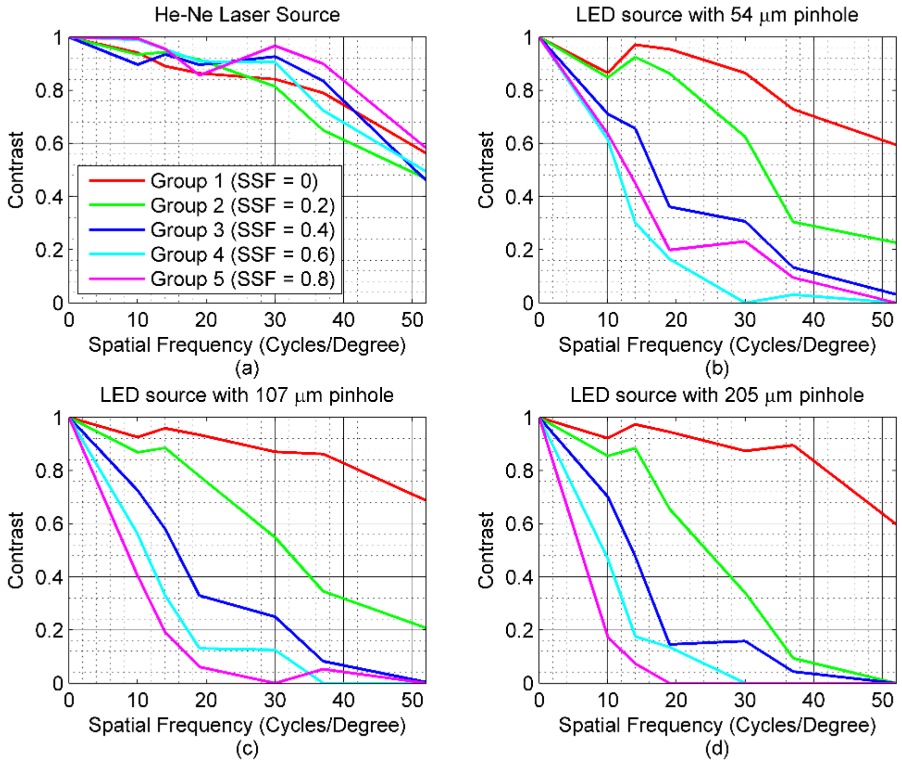

Figure 3.12 Spatial frequency versus contrast of different groups and light sources. We see that the contrast of images reconstructed using an LED source is comparable to a laser source when the SSF value is zero (group one). (a) The case of using the laser source. As we expected, the laser source provides the best contrast for various spatial frequencies in all groups. (b) The case of using an LED source with 54μm emission area. The contrast is the best when the SSF value is zero (group one). In the remaining groups, contrast decreases as the SSF value increases. (c) The case of using an LED source with 107μm emission area. The contrast is the best when the SSF value is zero (group one). In the remaining groups, contrast decreases as the SSF value increases. Contrast starts to drops down slowly in group two and significantly in the reaming groups. (d) The case of using an LED source with 205μm emission area. The contrast is the best when the SSF value is zero (group one). In the remaining groups, contrast decreases as the SSF value increases. Contrast starts to drops down slowly in group two and significantly in the reaming groups.

Figure 3.13 represents the effect of the temporal coherence on the image contrast. Based on our analysis, the effect of the light source's spatial coherence is negligible for configurations corresponding to group 1 (SSF=0). We average contrast values corresponding to group 1 (SSF = 0) of different LED sources. The average contrast values are considered an experimental metric of temporal coherence effect, as shown with a solid red line in Figure 3.13. We computed the average CTF of the simulated images in Figure 3.3(b) to Figure 3.3(d). The simulation results are reported with a solid blue line in Figure 3.13. We see that the simulation and experimental results provided in Figure 3.13 are in good agreement.

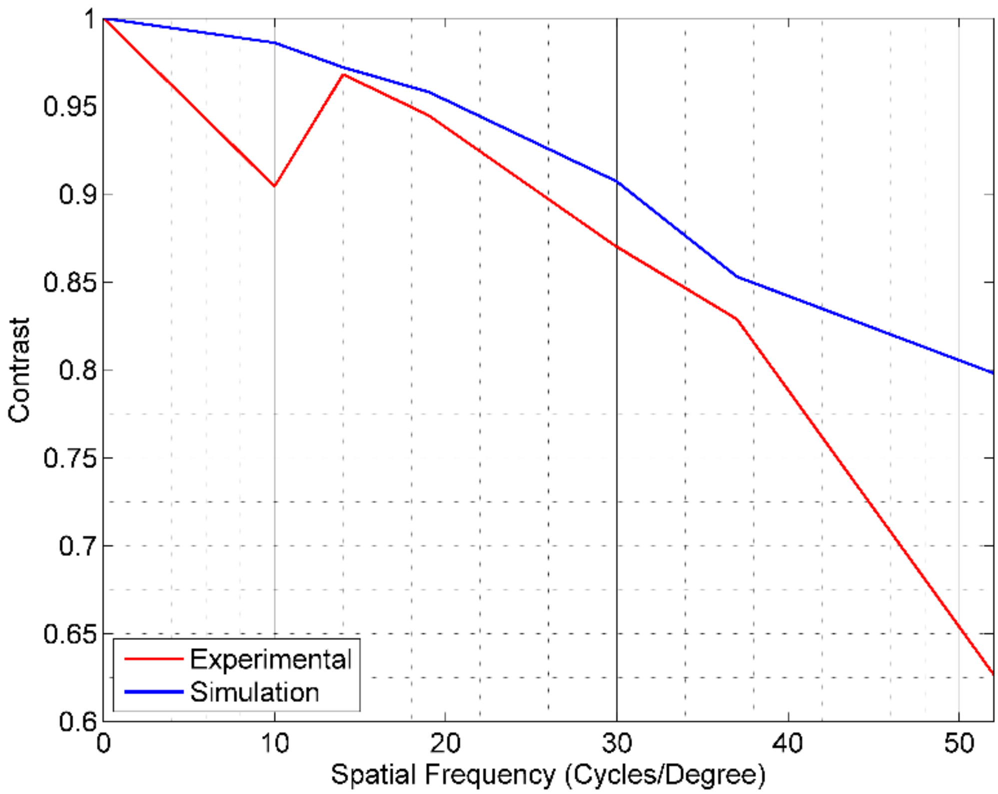

Figure 3.13 The experimental and simulated contrast values versus spatial frequency are illustrated. The solid red line corresponds to experimental results, where the solid blue line shows the simulation result.

Chapter 4

OFF-AXIS FLAT LENS FOR HOLOGRAPHIC NEAR-EYE DISPLAYS

A large FOV and small form factor are required in the design of AR head-worn displays. As relay elements, traditional AR head-worn displays with large FOV use bulky optical lenses and mirrors. In consumer applications, the low form factor of such displays adversely affects their adoption. Different solutions have been exploited by alternative techniques to reduce the size of the optics. Other methods to reducing the form factor in near-eye displays are unconventional relay optics, including holographic optical elements, waveguides, and diffractive optics. A micro-mirror array (MMA) is a type of DOE with a discrete pixelated structure. In this thesis, based on wave-optics simulations, an off-axis diffractive lens is designed with an MMA on a flat substrate surface. In a near-eye display system, the developed MMA is used to illuminate a computer-generated hologram. To minimize the focus spot's size, the normal directions, and center heights of each micro-mirror are optimized. To satisfy a phase-matching condition, where the fields interfere constructively at the focus spot location, each micro-mirrors center height has a nanometer-scale difference with respect to the neighboring micro-mirrors. The experimental results show that a bulky elliptical optical relay can be replaced by the developed and fabricated compact MMA. The MMA design process is discussed in Section 5.1. We chose a small section of the designed MMA is fabricated using gray-scale lithography, and the results are reported in this chapter.

4.1 Design process of MMA

The MMA discussed in this section comprises flat micro-mirrors and is intended for the optical configurations, as shown in Figure 4.1. Schematic perspective sketches of the imaging and near-eye layout are demonstrated in Figure 4.1(a) and Figure 4.1(c), respectively. We provide optical distances for the imaging and near-eye setups in Figure 4.1(b) and Figure 4.1(d), respectively. In these illustrations, the optical axis is parallel to the z-axis. The point light source in this design is placed at (3, 0, 3) cm from the MMA center. After hitting the MMA, the light emanating from the light source is reflected and is focused at (0, 0, 12) cm. A binary CGH is used to test the performance of the MMA. As shown in Figure 4.1(c) and Figure 4.1(d), the reflective binary CGH is placed at (0, 0, 6) cm. The rays reflect from the binary CGH mask, and after reflecting from a beam-splitter, the rays get focused on the pupil plane.

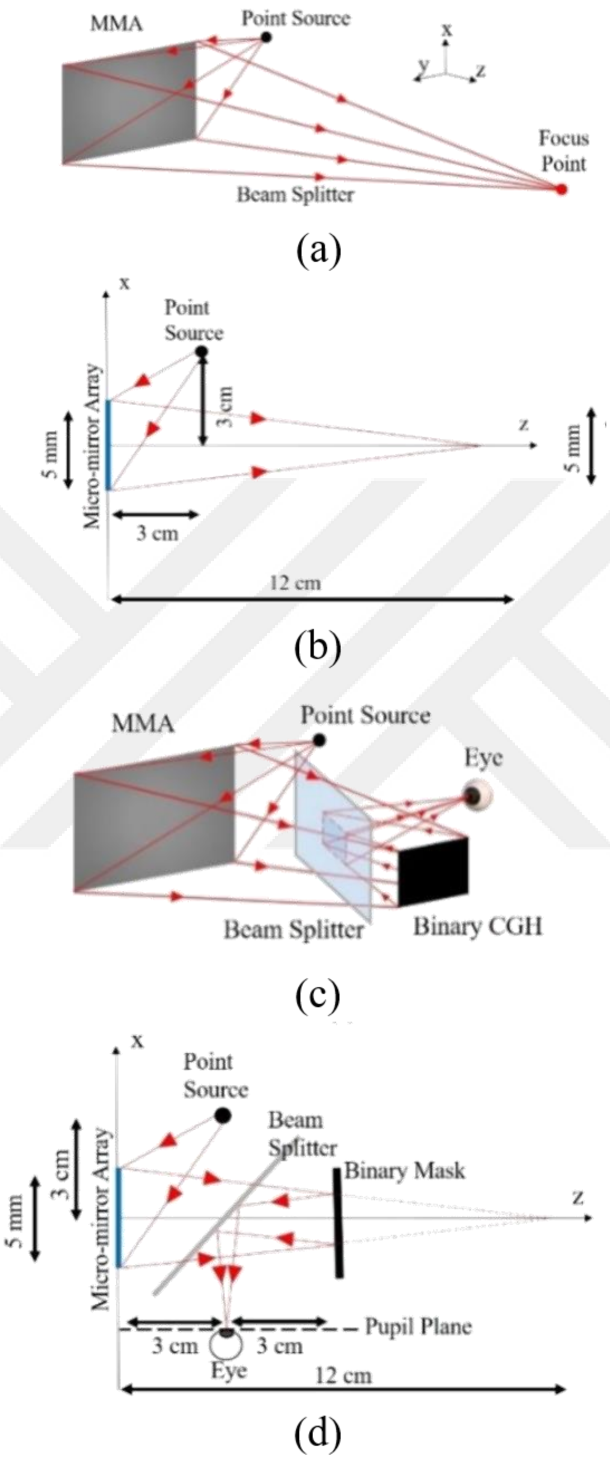

Figure 4.1 The optical designs and the corresponding distances to benefit the MMA. (a) A schematic drawing is provided in a perspective view and (b) top view of the imaging setup, including the distances. (c) Perspective schematic drawing of the near-eye setup using a binary mask and (d) top view of the near-eye setup using a binary CGH including the distances.

The normal direction and location of each micro-mirror must be adjusted through the design process of MMA to achieve the best output, taking into account wave optics and interference effects. Failure to do so results in shallow performance systems. We first go through an analysis where the interference is neglected or has a random nature after reflections from various micro-mirrors. We illustrate that the focal spot size obtained is unacceptably wide in that situation. Then, we demonstrate that once mirrors are configured to form a constructive interference in the focal plane with reflections, the achieved focal spot's size is dramatically reduced. The random interference of the reflections from the MMA's micro-mirrors introduces arbitrary phases at the focal plane. The focal spot size cannot be smaller than the spot generated by a single micro-mirror on the focal plane. Furthermore, with the tilt of mirrors towards the focus spot, the focus is achieved. We analyze the spot size produced by a single micro-mirror. In Figure 4.2, a drawing of a micro-mirror of the MMA can be seen. The dashed red line illustrates a chief ray emanating from the light source and reflects from the micro-mirror center, and follows the focal plane's path. The image of the illumination part because of the flat micro-mirror is illustrated with a dotted line. The distances used in the analysis are illustrated on top of the green arrows in Figure 4. 2. The aperture projection of each MMA with size Δ is referred to as Δ_N, where $\Delta_N = \Delta\cos\theta$.

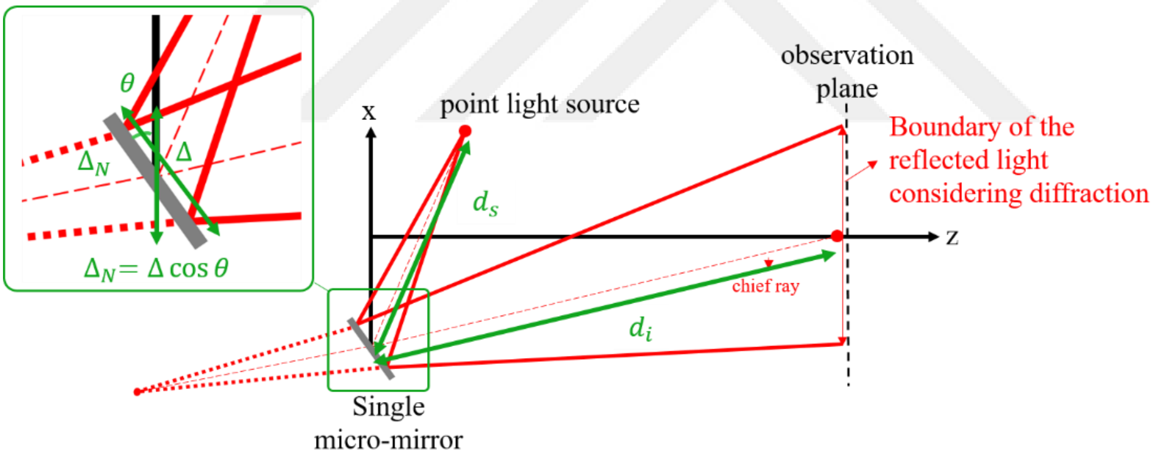

Figure 4.2 A schematic drawing of the corner micro-mirror of the desired MMA. The dashed red line illustrates the chief ray that reflects from the center of the micro-mirror.

The geometrical boundary of the focus spot (D_G) on the plane of observation can be found approximately using the following equation:

$$D_G = \Delta_N \frac{d_i + d_s}{d_s}, \tag{4.1}$$

where d_i indicates the image distance between the focus point and the micro-mirror center. The distance between the point light source and the center of the micro-mirror is denoted by d_s, as illustrated in Figure 4.2. For a square-shaped micro-mirror, the size of the reflected spot enlarges because of the diffraction effect (D_D) and can be computed using:

$$D_D = 2.44\,\lambda \frac{d_i}{\Delta_N} \tag{4.2}$$

where λ is the wavelength. Therefore, the size of the non-optimized focused spot on the observation plane is $D_D + D_G$. Using flat micro-mirrors with a 220 µm pitch scale, which is not suitable for near-eye applications, a minimum spot size of 1.68 mm can be achieved. Using the curved micro-mirrors with a zero geometric contribution to the focus spot size, an appropriate spot size would not be achieved due to diffraction and random interference of the fields reflecting from the micro-mirrors. Besides, curved profiles are much more difficult to manufacture with good optical power and efficiency. We focused primarily on micro-fabricated small and flat micro-mirrors with diffraction-limited performance. The micro-mirrors are positioned in our design such that the projection of the micro-mirror centers on the plane x-y is spaced evenly by an amount of Δ and has a square shape. Note that it is possible to use other standard tessellations (e.g., hexagons) instead. However, the rectangular shape is simpler to design and more comfortable to achieve in design. Besides, due to the pixelated nature of the MMA with square-shaped micro-mirrors, diffraction orders are positioned in a rectangular grid that is more suitable for close-eye application because it offers a rectangular eyebox that can be filtered out more conveniently. To define each micro-mirror's tilt, we can refer to the angle of the normal vector with the x, y, and z axes. Each micromirror has a tilt range in the final MMA between 20 degrees and 40 degrees. The schematic drawings in Figure 4.3(a) and Figure 4.3(b) illustrate the 3D MMA top view and the corner micro-mirrors' zoomed views.

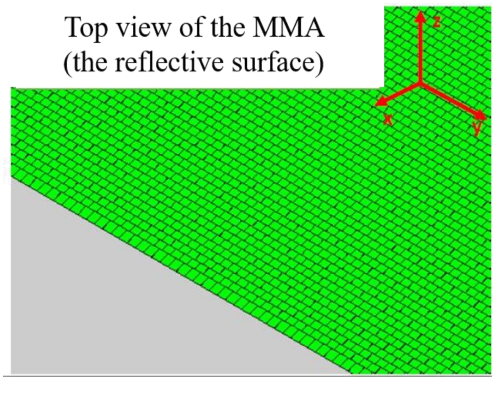

(a)

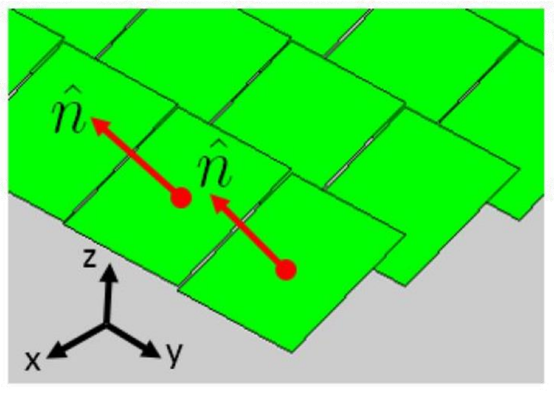

(b)

Figure 4.3 The schematic 3D illustration of the MMA. (a) The top 3D view of the reflective surface of MMA. (b) A zoomed view of several corner micro-mirrors with normal vectors.

The use of gray-scale lithography techniques is one practical way to manufacture MMA. The maximum limit for the micro-mirror size is ruled by the etch depth ($h_{\max}$), which is limited to less than 30 microns in the fabrication process. The corner micro-mirror's peak-to-peak height is illustrated with a solid blue line in Figure 4.4(a). The size of each micro-mirror in the array must not exceed 60 microns, as shown in Figure 4.4(a). The separation of the 0th and 1st diffraction orders (D_O) is a limiting factor in the design process and can be computed using:

$$D_O = \lambda \frac{d_i}{\Delta} \tag{4.3}$$

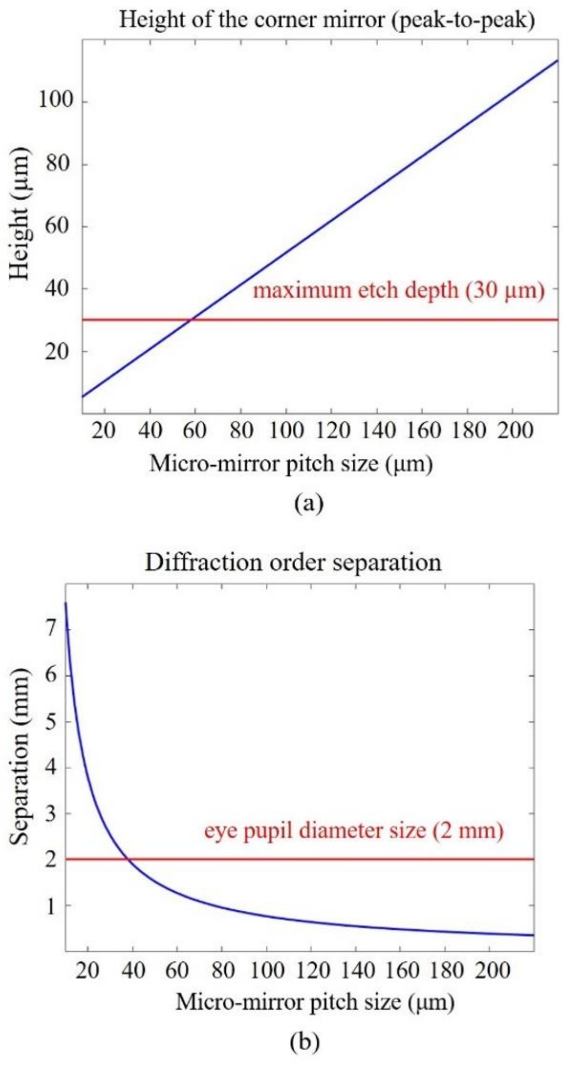

Figure 4.4 (a)The solid red line indicates the 30 microns limit of the fabrication process. It sets a maximum limit for the fabricable micro-mirror size. (b) The distance between diffraction orders with respect to the pitch size of micro-mirror. The separation between diffraction orders at the pupil plane must be greater than the size of the eye pupil diameter, taken as 2 mm for our design as we intend to use the MMA in a near-eye display and illustrated with a solid red line.

For near-eye display applications, the design of MMA must be such that the separation between diffraction orders at the pupil plane becomes more extensive than the eye pupil diameter size.

We consider the eye pupil diameter as 2 mm for our design, and this limit is indicated with a solid red line in Figure 4.4(b). The separation of diffraction orders with respect to the pitch-size of the micro-mirror is plotted with a solid blue color in Figure 4.4(b). The simulations in Figure 4.4 reveal that the size of each micro-mirror in the array must be less than 40 microns. To optimize several factors, we selected a micro-mirror size of 40 microns. The tilt of the mirror within the microfabrication limits is kept maximum. Furthermore, smaller mirrors are desired to provide enough space between diffraction orders at the desired distance. Due to microfabrication limits, larger mirrors up to 40 microns are better to minimize the edge effects and other tolerances. The generated total field by the MMA (considering scalar wave optics theory of light) can be shown as

$$U(\mathbf{r}) = \Sigma U_m(\overline{\mathbf{R}}_m \cdot \mathbf{r} + \mathbf{t}_m), \tag{4.4}$$

where $\mathbf{r} \in \mathbf{R}^{3\times1}$ are the coordinates of the observation point in the global coordinate system, $\overline{\mathbf{R}}_m \in \mathbf{R}^{3\times3}$ and $\mathbf{t}_m \in \mathbf{R}^{3\times1}$ are the rotation matrix and the translation vector to transform to the local coordinate system of the mth micro-mirror. The term U_m in the equation mentioned above is the function that defines the light generated by mth micro-mirror in the local coordinates of the mth micro-mirror. We assume that the x and y axes lie parallel to the mirror surface, and the z-axis is aligned in the mirror's normal direction. The center of the micro-mirror is considered as the origin. Using Rayleigh-Sommerfeld diffraction integral, the expression for U_m is

$$U_m(\mathbf{r}) = \frac{z}{j\lambda}\int \frac{e^{jk|\mathbf{r}'-\mathbf{r}_m^s|}}{|\mathbf{r}'-\mathbf{r}_m^s|}\cdot\frac{e^{jk|\mathbf{r}-\mathbf{r}'|}}{|\mathbf{r}-\mathbf{r}'|}\,\mathrm{d}\mathbf{r}', \tag{4.5}$$

where $\mathbf{r}_m^s$ denotes the position of the virtual image of the point light source that is formed by the mth micro-mirror in the local coordinates of the mth micro-mirror. In the design of MMA, we want to form a focal spot at $\mathbf{r}_f$, i.e., we want to ensure that $|U(\mathbf{r})|^2$ has a peak at $\mathbf{r} = \mathbf{r}_f$. We optimize the center heights and normal directions (tilt angles) of each micro-mirror to accomplish this objective. The changes in the center height and normal directions of each micro-mirror affects $U(\mathbf{r})$ through the $\overline{\mathbf{R}}_m$, $\mathbf{t}_m$ and $\mathbf{r}_m^s$ terms.

We adopt an intuitive approach, which is confirmed by our simulations and experimental results, instead of attempting an optimization based on the complicated formulas above. There are two assumptions in our approach. The first assumption is that all individual contributions $U_m(\overline{\mathbf{R}}_m \cdot \mathbf{r}_f + \mathbf{t}_m)$ have the same phase value at $\mathbf{r} = \mathbf{r}_f$, and $|U(\mathbf{r})|^2$ will have a peak value at $\mathbf{r} = \mathbf{r}_f$. This assumption leads to a full constructive interference. If this condition is satisfied at $\mathbf{r} = \mathbf{r}_f$, as $\mathbf{r}$ gets away from $\mathbf{r}_f$ the full constructive interference condition gets violated since phase values will change. This condition results in destructive interference and a fast decay in the intensity that ensures the peak at $\mathbf{r} = \mathbf{r}_f$. Second, we assume that phase of $U_m(\overline{\mathbf{R}}_m \cdot \mathbf{r}_f + \mathbf{t}_m)$ is equal to $2\pi/\lambda(|\mathbf{r}_s - \mathbf{r}_m| + |\mathbf{r}_m - \mathbf{r}_f|)$. In this case, the full constructive interference condition will be satisfied if $|\mathbf{r}_s - \mathbf{r}_m| + |\mathbf{r}_m - \mathbf{r}_f| = k\lambda$, $(k \in Z)$, where $\mathbf{r}_m$ is the global coordinate of the mth micro-mirrors center and $\mathbf{r}_s$ is the global coordinate of the point light source. The second statement holds if diffraction is ignored due to the mirror aperture, which is not possible in our case. Nevertheless, assuming that mirror tilt angles are modified to direct the light from the source to the focal spot, the approximation is accurate to a reasonable degree.

We used wave optics simulation to find the field distribution in the provided architecture's focus spot shown in Figure 4.1 using MATLAB. The MMA size is assumed to be 5 mm × 3 mm in these simulations and matches the fabricated part size. We assign an aperture for each micro-mirror to model the pitch size and shadow effects in these simulations. Furthermore, a virtual grating was added to each micro-mirror to handle the light's steering towards the focal point. The grating term introduces a phase offset to guarantee that we have a constructive interface at $\mathbf{r}_f$. Based on this model, we compute the field on the entire aperture of MMA. A free-space propagation of the field on MMA towards the focal spot is performed to find the field on the pupil plane.

The simulated far-field point spread function (PSF) of the MMA is illustrated in Figure 4.5. The intensity (I) of the signal U is $I = |U|^2$. The normalized intensity I_N is computed as $I_N = I/\max(I)$ and used in the following illustrations. Figure 4.5(a) shows the spot size where the phase-matching condition is not satisfied for the monochrome case ($\lambda = 632$ nm). The PSF is distributed with a diameter of almost 1.5 mm over the x-axis in Figure 4.5(a) since the fields from individual micro-mirrors randomly interfere at the focal point. It is possible to minimize the random interference issue by optimizing the normal directions and center heights of each micro-mirror. To satisfy the phase-matching condition, where the fields interact constructively at the pupil plane, each micro-mirror's center height has a nanometer-scale difference with respect to the neighboring micro-mirrors. Optimizing the center heights guarantees that the optical path from the light source to the pupil plane is an integer multiple of the design wavelength. The phase-matching condition is fulfilled. The spot size where the phase-matching condition is fulfilled for a single wavelength is shown in Figure 4.5(b) and Figure 4.5(c). The plots display the same normalized intensity plot with various horizontal axis (x-axis) scales in Figure 4.5(b) and Figure 4.5(c). After meeting the phase matching condition, the focused spot size is reduced to approximately 30 microns, as seen in Figure 45 (c). In Figure 4.5(c), the simulated focused spot's full-width half-maximum is 10.4 microns. For the monochrome MMA configuration, the maximum center height difference between two adjacent micro-mirrors after applying the phase-matching condition is 96 nm. We define a synthetic design wavelength as the least common multiple red, green, and blue wavelengths for full-color applications. The central heights of micro-mirrors are optimized based on the defined synthetic wavelength. Figure 4.5(d) shows the spot size without phase-matching condition for the full-color case. The red, green, and blue wavelengths are chosen as 632, 520, and 450 nm. Figure 4.5(e) and Figure 4.5(f) show the focused spot size where the phase-matching condition is met for the red, green, and blue wavelengths. The plots in Figure 4.5(e) and Figure 4.5(f) provide the same normalized intensity plot with different horizontal axis (x-axis) scales. The separation distance between the 0th and the 1st diffraction orders decreased in the full-color case because the blue color has a smaller wavelength than the red wavelength, as illustrated in Figure 4.5(f) and Figure 4.5(e). By reducing the micro-mirror pitch size from 40 microns to 20 microns, this problem can be solved. For the full-color MMA design, the maximum center height difference between two adjacent micro-mirrors after applying the phase-matching condition is 238 nm. Figure 4.6

shows the schematic drawing of center positions before applying the phase-matching condition (a). The schematic drawing of changed center positions after applying the phase-matching condition is shown in figure 4.6(b). For the monochrome case, the center locations' variation along the MMA aperture is shown in Figure 46 (c). As is evident in Figure 4.6(c), the maximum center height difference between two adjacent micro-mirrors after applying the phase-matching condition is 96 nm for the monochrome MMA configuration. Figure 4.6(d) shows the plot's cross-section given in Figure 4.6(c) with a vertical micro-mirror index of 55. Surface roughness should be less than $\lambda/20$ across any 2mm × 2mm area, which corresponds to the pupil area, to reach good optical performance. The total roughness across the whole part should be less than $\lambda/2$ to guarantee good flatness across the fabricated mirror.

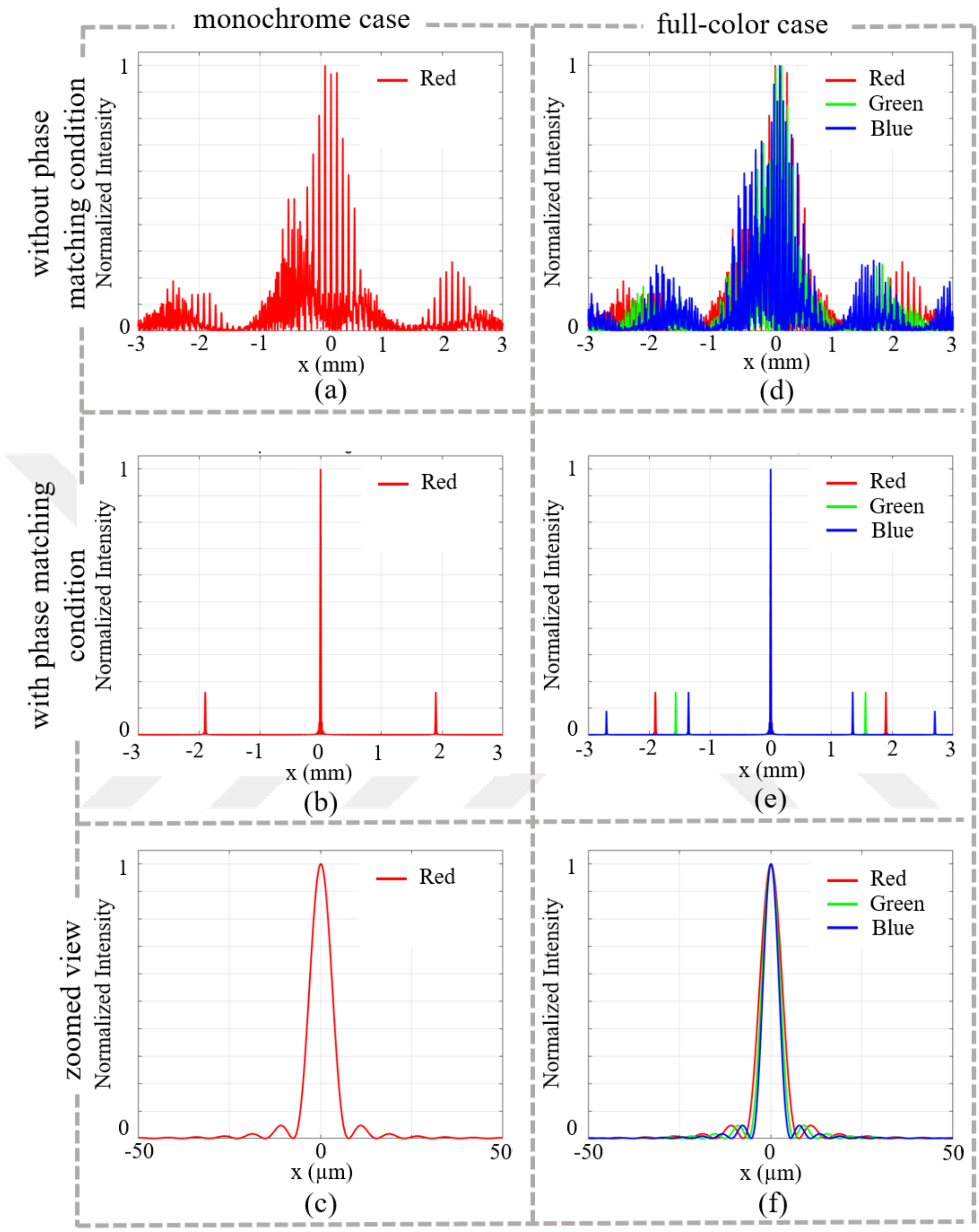

Figure 4.5 The far-field PSF of the MMA at the focal plane. (a) The spot size without phase-matching condition is plotted for the monochrome case with $\lambda = 632$ nm. (b) and (c) The spot size with the phase-matching condition for a single wavelength. The plots in (b) and (c) demonstrate the same normalized intensity information with different horizontal axis (x-axis) scales. (d) The spot size for the full-color case without phase-matching condition is provided (e) and (f) The spot size with the phase-matching condition. The plots (e) and (f) The similar normalized intensity plot with different horizontal axis (x-axis) scales.

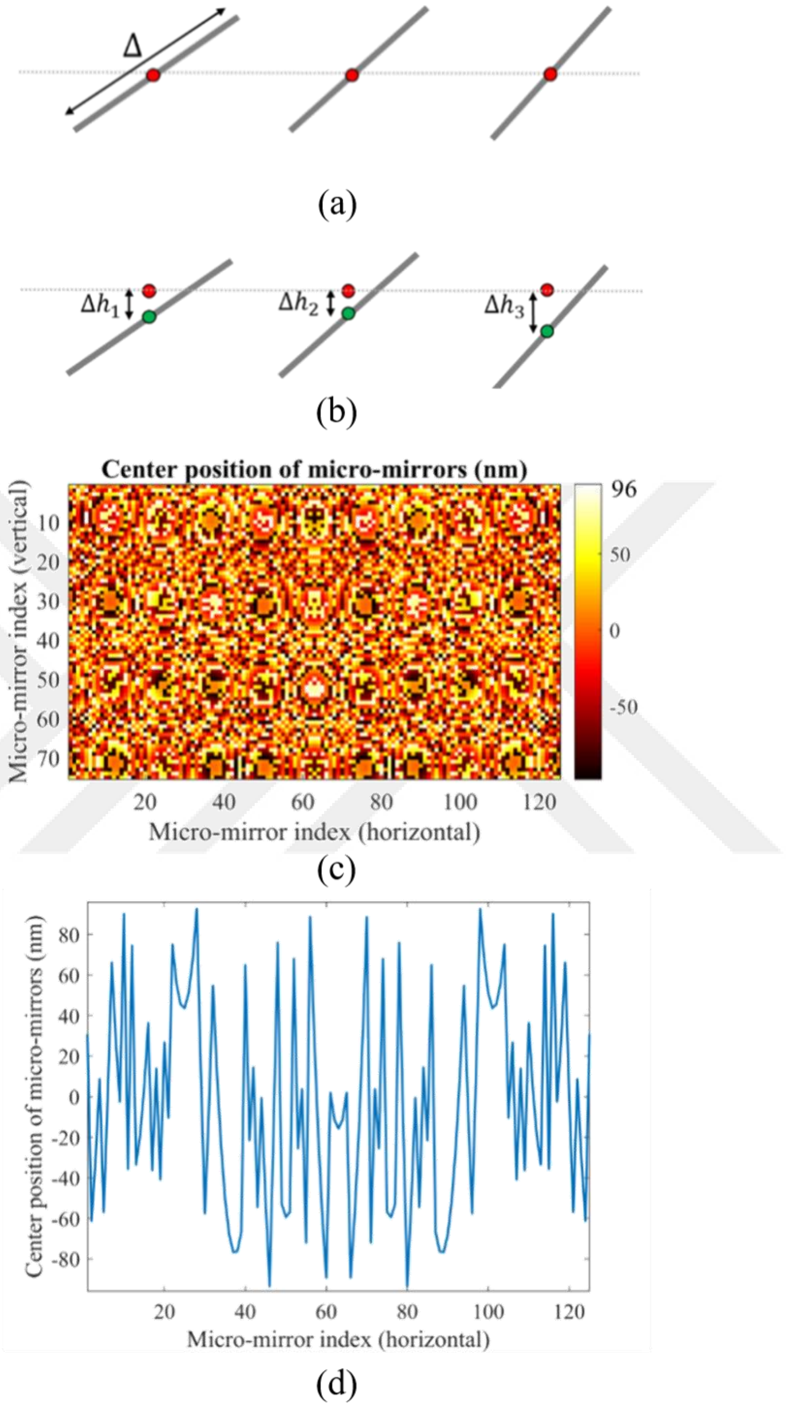

Figure 4.6 (a) The center positions of individual mirrors before considering the phase-matching condition. (b) The center positions of mirrors after satisfying the phase-matching condition. (c) The variation of the center positions along with the MMA aperture for the monochrome case. (d) The cross-section plot of the height variation of the micro-mirror centers.

As shown in Figure 4.7(a), MMA produces an on-axis converging beam from a 45 degree off-axis diverging illumination beam. By propagating a converging wave passing through a 5 mm single slit (as shown in Figure 4.7(b)), the size of the diffraction-limited focused spot on the focal plane is simulated. The logarithmic plot of the focused spot PSF is generated with the phase-matched MMA and shown with a solid red line in Figure 4.7(c). A solid blue line is plotted to indicate the size of the diffraction-limited focused spot on the focal plane. As evident in Figure 4.7, after satisfying the phase-matching condition, the MMA acts as a diffraction-limited component.

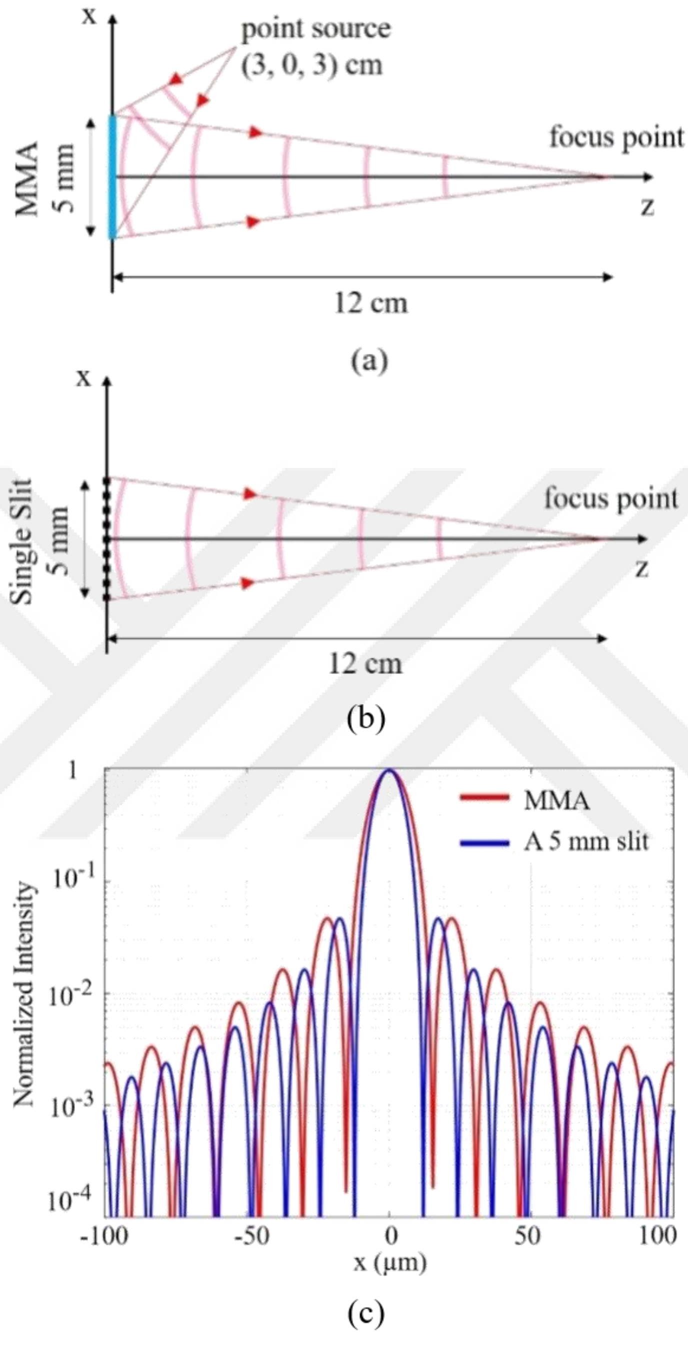

Figure 4.7 (a) MMA produces an on-axis converging wave from a 45 degrees off-axis diverging illumination wave. (b) The size of the diffraction-limited focused spot on the focal plane is simulated by propagating a converging wave passing through a 5 mm single slit. (c) The logarithmic plot of the focused spot PSF created with the phase-matched MMA is shown with a solid red line, and the size of the diffraction-limited focused spot on the focal plane is provided with a solid blue line.

4.2 Experimental results

Using gray-scale lithography on a photo-resistant polymer placed on a 1 mm thick N-BK7 glass substrate material, we built a sample component with a size of 3 mm by 5 mm to conduct the experiments. The primary limiting factor for the MMA size was the high cost of manufacturing a custom sample component. A 250 µm border that has no exposure surrounds the MMA area. Another border area with a trench is around this one. The trench is five µm deep and 100 µm long. For the square micro-mirrors, the side length is 40 microns. The height of each micro-core mirror is different, in the order of a few nanometers. Nickel-coated photoresist master with a thickness of 30 microns is the final part. The 50x measurement of the manufactured MMA is shown in Figure 4.8. (parts were fabricated and measured by Infinite Graphics Co, USA).

The tilt was removed, and the height difference was measured using the MicroSpy scanning chromatic confocal surface measuring instrument. As shown in Figure 4.8(a), the difference in height between the two corners at the micro-mirror is 29.2 µm. The height variance over a single micro-mirror is calculated to be 90 nm after eliminating tilt due to the gray-scale lithography process's step artifacts. It means that the root means square (RMS) surface roughness of the fabricated micro-mirrors meets optical quality requirements. A better representation of the fabricated component is given in Figure 4.8(b), where the height decreases as we pass from the blue parts to the red parts.

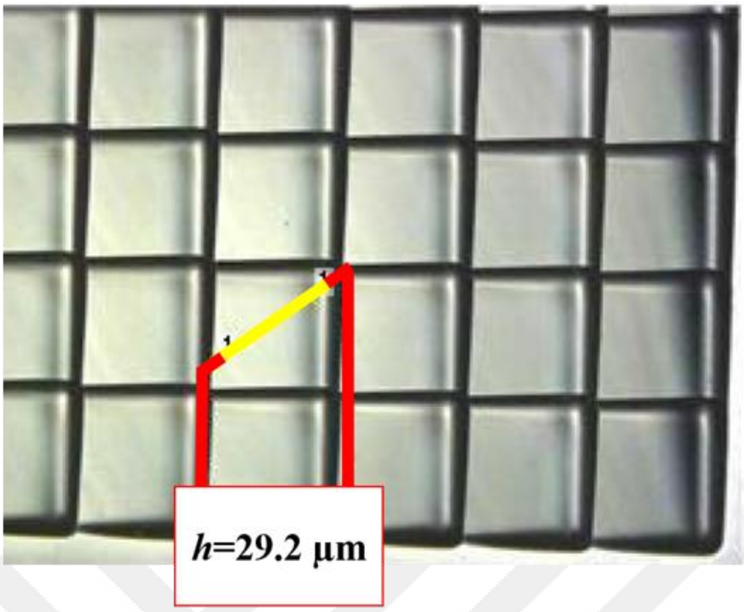

(a)

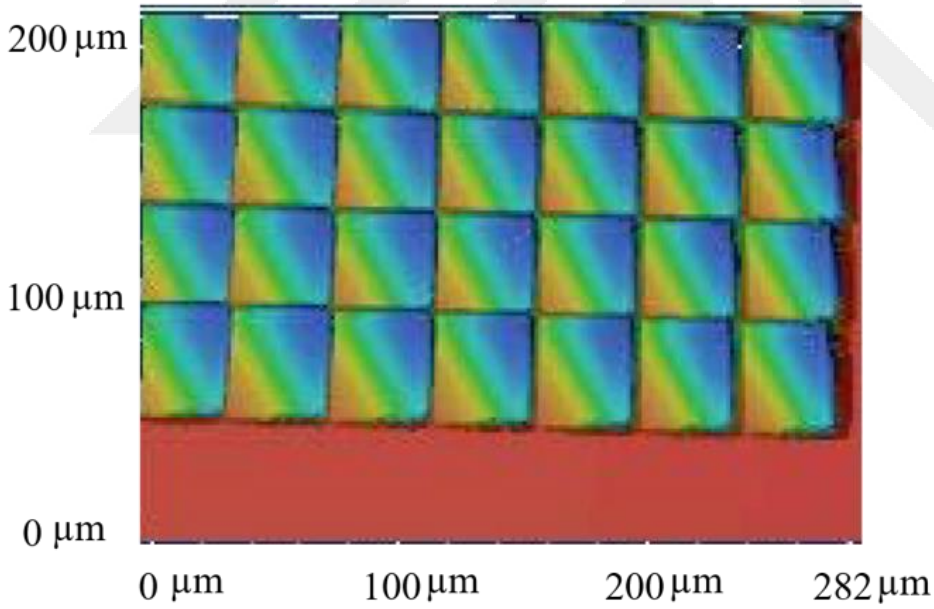

(b)

Figure 4.8 The 50x measurement of the fabricated MMA is provided. (a) The height variance over a single micro-mirror is estimated to be 90 nm after eliminating the tilt. Note that 29.2 µm is the difference in height between the two corners of a single micro-mirror. (b) A better representation of the produced part, where the height decreases as we step toward the red parts from the blue parts. (Fabricated and measured by Infinite Graphics Co., USA).

The focus spot produced by the manufactured MMA is shown in Figure 4.9 using the setup given in Figure 4.1(a) and Figure 4.1(b). Multiple replicas (diffraction orders) of the focal spot are observed on the focus plane, as predicted, due to the manufactured micro-mirrors' periodic structure, instead of a single focus point. If there were no phase matching condition, the diffracted waves reflected from each micro-mirror would not interfere constructively, and the focused spot would be as large as the space between the orders of diffraction (in millimeter range). The phase-matching condition is met as expected, as is evident from the focused spot images, and the spot size is much smaller than the separation of the diffraction order. As shown in Figure 4.9, full-width at half-maximum is calculated as 40 microns. Because of the lithography process's step artifacts, the value of the experimental PSF is greater than the simulated PSF. Because of the periodic structure of the design, diffraction orders appear, as expected. Techniques to remove diffraction orders at the cost of decreased contrast are Fourier filtering or using non-periodic designs.

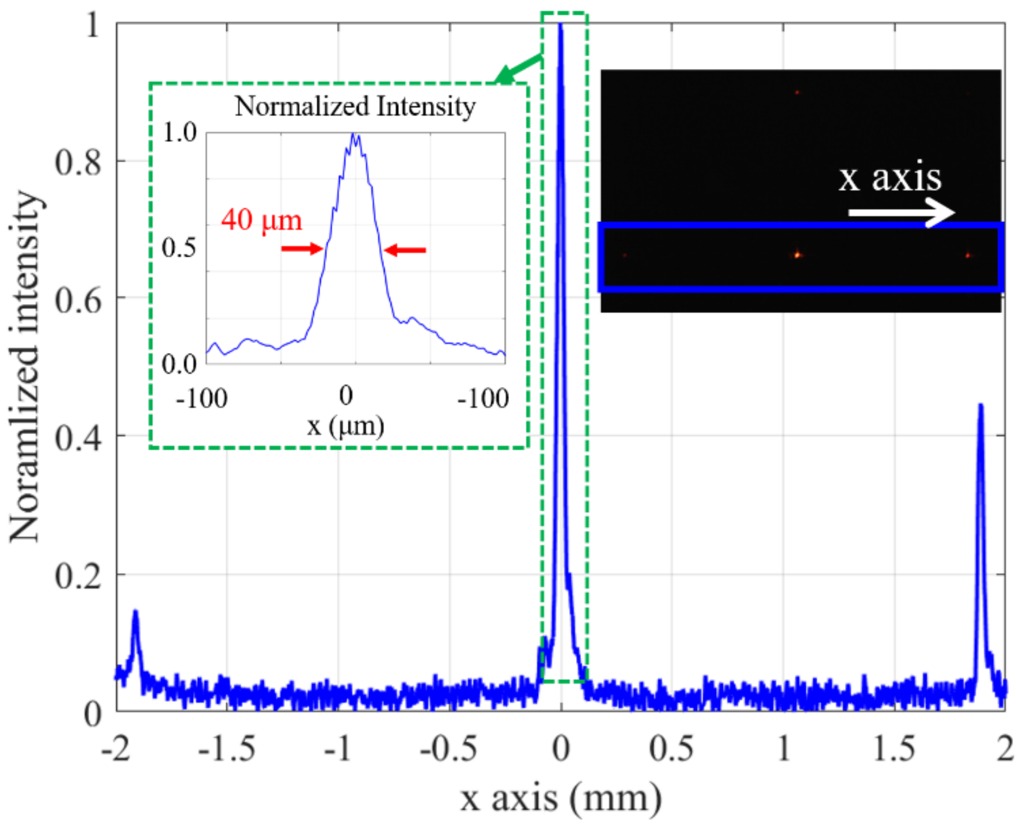

Figure 4.9 The measured, focused spot size created by the fabricated MMA. As plotted, the full-width at half-maximum is measured as 40 microns, which matches the simulation results.

The MMA is used in the layout shown in Figure 4.10(a). The fabricated MMA is used to illuminate a binary CGH mask. In this experiment, the static binary amplitude CGH used is computed using the method discussed in [Kazempourradi et. al., 2019], and the encoding is done using the error diffusion algorithm. It illuminates a 1.5 mm x 2.5 mm region of the mask and uses a CCD camera to capture the reconstructed image. The captured image of the reconstructed hologram is shown in Figure 4.10(b). The MMA has a limited view of 1.43 degrees by 2.38 degrees, and the distance between the eye and the reconstructed image is 500 mm. At a distance of 500 mm from the eye, the captured image scale is 12.5 mm by 20.8 mm. In a near-eye display system with coherent light illumination, such an MMA can be utilized.

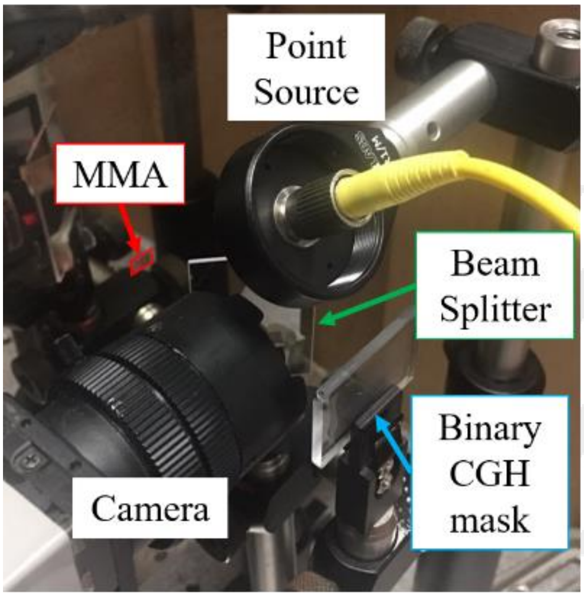

(a)

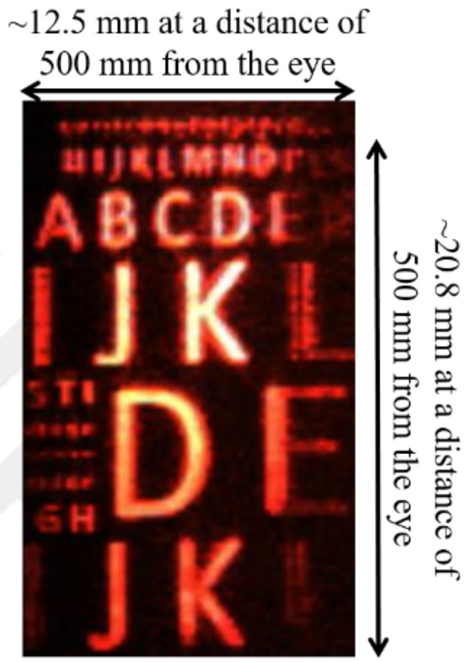

(b)

Figure 4.10 (a) The near-eye display architecture used in the experiment with 45 degrees off-axis beam. (b) Image of the captured hologram with a camera at the position of the eye. The captured image size is 12.5 mm × 20.8 mm at a distance of 500 mm from the eye.

Chapter 5

CONCLUSION

This thesis shows that the combination of the near-eye and holographic display realms can lead to groundbreaking achievements: on the one hand, NEDs that have suffered from bulkiness and produced visual discomfort can become impressively compact to accomplish eye-glass form factors while providing very large FOVs, retinal resolution, and realistic 3D. Holography supports the NED domain, thereby eliminating the need to use relay optics and providing natural accommodation. On the other hand, even with today's technology, holographic displays, which were thought to be a dream due to the immense space-bandwidth product requirements, are realizable. Here, by minimizing the eyebox size and parallax that needs to be delivered to a user at one time, the NED domain supports holography. The HNED setup also provides the pupil and head trackers with the most comfortable setting and greatly improves light efficiency and freedom of motion. The current state of SLM technology prevents holographic displays from enjoying their full potential. In augmented reality applications, the non-transparent nature of LCoS SLMs prevents the SLM from positioning directly in front of the eye. Unfortunately, transmissive SLMs currently available have pixel pitches of about 20-40 μm, too big for near-to-eye setups. Even if the transmissive SLMs pixel pitches shrink down to 5-10 microns, the real-world light will also get modulated by the CGH, producing visual artifacts. However, the above problem can be avoided if the SLM pixel pitch decreases to about one micron, perhaps through several newly emerging technologies. It is possible to help a large number of pixels, and a wider eyebox size of 10-15 mm, and stop pupil trackers. While such advances will take some time if the display industry focuses on small-pixel SLMs with low-pixel crosstalk, even faster progress might be possible.

The high computational cost of CGH computation poses yet another challenge, especially when pupil and head tracker integration is taken into account. However, we think that once the technological challenges are solved, the unification will realize the ultimate customized interactive display. In this thesis, the matrix-optics approach analyzes the FOV and the eyebox size of the HNED. The FOV of the HNED is determined, followed by a condition on the size of the eyebox using matrix-optics analysis. A fundamental relation between the product of the FOV and effective eyebox size is reported. Based on these fundamental results, the design procedure of the HNED is outlined. A clear method for computation of CGH using scalar wave optics and the matrix-optics analogy is reported. Our computation method is capable of reducing speckle noise and chromatic aberrations arising from optics and light sources. The proposed method is verified with various simulations and optical experiments. The simulation and experimental results for two optical architectures with the same optical components and different FOVs of 10 and 20 degrees are reported. These experimental results prove that the matrix-optics analogy is suitable for the design and fabrication of the HNED. The developed HNEDs provide high-quality holograms with high resolution and true per-pixel focal control in the fovea.

We have investigated the effect of spatial and temporal coherence of light-emitting diode (LED) sources in holographic displays on reconstructed holograms' resolution. We provide an analytical expression based on paraxial approximation and matrix optics. Based on these expressions, we define a source-size factor (SSF). If SSF=0, the source size does not impact the resolution of the virtual image. The SSF=1 case implies that to display a high-quality image, the source must have zero extend, i.e., the source must have full spatial coherence. The quality of a hologram degrades due to the lack of temporal coherence in LED light sources. However, based on our simulations, it is almost negligible. We performed several experiments to verify our theoretical analysis. We experimentally investigate various combinations of the distances in optical architecture and different virtual object distances. All configurations are categorized into five different groups based on their SSF value. We captured the reconstructed holograms. The contrast transfer function of each captured image is analyzed. The experimental results show that utilizing a finite-extent source does not degrade image quality in configurations with SSF=0. In this configuration, the main reason for the loss in the reconstructed hologram is the lack of temporal coherence. The theoretical analysis and experimental results prove that the amount of resolution loss is almost not perceivable with the human eye for a certain range in depth. Effects of the lack of temporal coherence are simulated. It is still possible to obtain a decent image quality using a source with a finite spectrum bandwidth. We endorse the latter case experimentally by constructing crisp holographic images with different virtual object depths.

Besides, for an AR holographic display application, a micro-mirror array is incorporated as an alternative thin and flat lens technology to reduce the relay optics' size and weight. An off-axis diffractive lens with several advantages over holographic optical elements is the MMA discussed in the thesis. For any wavelength desired, the MMA can be numerically developed. Along with gray-scale lithography techniques for manufacturing MMA, a computer-generated design procedure is developed. An initial MMA sample can be manufactured once with grayscale lithography and can then be used as a master shim to generate several MMA replicas easily. The proposed MMA consists of individual square micro-mirrors with different center heights and normal directions. To satisfy the phase-matching condition at the design wavelength, the micro-mirrors in the array need to have different center heights in the range of a couple of nanometers. A synthetic design wavelength is specified as the least common multiple red, green, and blue wavelengths for full-color applications. This synthetic wavelength can be used to refine micro-mirrors' center heights. MMA generates an on-axis converging beam from a 45 degree-off-axis diverging illumination wave in our implementation. Like a large and bulky elliptical mirror, the designed MMA can be used in a holographic setup. Thanks to its reflective nature, the MMA retains its light efficiency with small changes in the output focal spot and shape. Using diffraction simulations, the micro-mirror size is calibrated to fulfill the phase-matching requirement. A 3 mm by 5 mm sample component is fabricated using gray-scale lithography on a photo-resistant polymer mounted on a 1 mm thick N-BK7 glass substrate. The lateral length is 40 microns for each square micro-mirror. In a near-eye display architecture, the fabricated MMA is used. The field of view is reduced to 1.43 degrees by 2.38 degrees, limited by the MMA size. In a near-eye holographic display, the fabricated MMA has been tested successfully.

BIBLIOGRAPHY

[Jerald, 2016] Jerald, J. (2016). The VR Book: Human-Centered Design for Virtual Reality, ACM Books.

[Barfield, 2015] Barfield, W. (2015). Fundamentals of Wearable Computers and Augmented Reality, Second Edition, Taylor & Francis, Boca Raton, FL.

[Inzerillo, 2013] Inzerillo, L. (2013). Augmented reality: past, present, and future, Proc. SPIE 8649, 86490E.

[Azuma, 1997] Azuma, R. T. (1997). A Survey of Augmented Reality, Presence: Teleoperators and Virtual Environments 6(4), 355–385.

[Cakmakci and Rolland, 2006] Cakmakci, O. and Rolland, J. (2006). Head-worn displays: a review, J. of Disp. Tech. 2, 199–216.

[Rolland and Cakmakci, 2009] Rolland, J. and Cakmakci, O. (2009). Head-worn displays: The future through new eyes, Opt. and Photon. News 20, 20–27.

[Koulieris, et. al., 2019] Koulieris, G. A., Akşit, K., Stengel, M., Mantiuk, R. K., Mania, K., and Richardt, C. (2019, May). Near-Eye Display and Tracking Technologies for Virtual and Augmented Reality. In Computer Graphics Forum (Vol. 38, No. 2, pp. 493-519).

[Van Krevelen and Poelman, 2010] Van Krevelen, D. W. F. and Poelman, R. (2010). A survey of augmented reality technologies, applications, and limitations, International J. Virtual Reality 9, 1–20.

[Kress, 2020] Kress, B. C. (2020). Optical Architectures for Augmented-, Virtual-, and Mixed-reality Headsets, SPIE, US.

[Deering, 1998] Deering, M. F. (1998). The limits of human vision. In 2nd International Immersive Projection Technology Workshop (Vol. 2).

[Navarro et. al., 1993] Navarro, R., Artal, P., and Williams, D. R. (1993). Modulation transfer of the human eye as a function of retinal eccentricity. JOSA A, 10(2), 201-212.

[Guirao et. al., 1999] Guirao, A., Gonzalez, C., Redondo, M., Geraghty, E., Norrby, S., and Artal, P. (1999). Average optical performance of the human eye as a function of age in a normal population. Investigative Ophthalmology and Visual Science, 40(1), 203-213.

[Meister, 2013] Meister, D. (2013). Memorandum to Vision Council lens Technical committee, Carl Zeiss Vision GmbH.

[Peli, 1998] Peli, E. (1998). The visual effects of head-mounted display (HMD) are not distinguishable from those of desk-top computer display. Vision research, 38(13), 2053-2066.

[Turnbull and Philips, 2017] Turnbull, P. R., and Phillips, J. R. (2017). Ocular effects of virtual reality headset wear in young adults. Scientific reports, 7(1), 1-9.

[Patterson and Earl, 2015] Patterson, P. D., and Earl, R. (2015). Human factors of stereoscopic 3D displays. Springer London.

[Banks et. al., 2016] Banks, M. S., Hoffman, D. M., Kim, J., and Wetzstein, G. (2016). 3D Displays. Annual Review of Vision Science, 2, 397-435.

[Harding and Rash, 2017] Harding, T. H., and Rash, C. E. (2017). Daylight luminance requirements for full-color, see-through, helmet-mounted display systems. Optical Engineering, 56(5), 051404.

[Barten, 2003] Barten, P. G. (2003). Formula for the contrast sensitivity of the human eye. In Image Quality and System Performance (Vol. 5294, pp. 231-238). International Society for Optics and Photonics.

[Wheelwright et. al., 2018] Wheelwright, B., Sulai, Y., Geng, Y., Luanava, S., Choi, S., Gao, W., and Gollier, J. (2018). Field of view: not just a number. In Digital Optics for Immersive Displays (Vol. 10676, p. 1067604). International Society for Optics and Photonics.

[Hua and Liu, 2008] Hua, H., and Liu, S. (2008). Dual-sensor foveated imaging system. Applied optics, 47(3), 317-327.

[Ienaga et. al., 2001] Ienaga, T., Matsunaga, K., Shidoji, K., Goshi, K., Matsuki, Y., and Nagata, H. (2001). Stereoscopic video system with embedded high spatial resolution images using two channels for transmission. In Proceedings of the ACM symposium on Virtual reality software and technology (pp. 111-118).

[Patney et. al., 2016] Patney, A., Salvi, M., Kim, J., Kaplanyan, A., Wyman, C., Benty, and Lefohn, A. (2016). Towards foveated rendering for gaze-tracked virtual reality. ACM Transactions on Graphics (TOG), 35(6), 179.

[Chang et. al., 2020] Chang, C., Bang, K., Wetzstein, G., Lee, B., and Gao, L. (2020). Toward the next-generation VR/AR optics: a review of holographic near-eye displays from a human-centric perspective. Optica, 7(11), 1563-1578.

[Cem et. al., 2020] Cem, A., Hedili, M. K., Ulusoy, E., and Urey, H. (2020). Foveated near-eye display using computational holography. Scientific reports, 10(1), 1-9.

[Kim et. al., 2019] Kim, J., Jeong, Y., Stengel, M., Akşit, K., Albert, R., Boudaoud, B., and Shirley, P. (2019). Foveated AR: dynamically-foveated augmented reality display. ACM Transactions on Graphics (TOG), 38(4), 1-15.

[Akşit et. al., 2019] Akşit, K., Chakravarthula, P., Rathinavel, K., Jeong, Y., Albert, R., Fuchs, H., & Luebke, D. (2019). Manufacturing application-driven foveated near-eye displays. IEEE transactions on visualization and computer graphics, 25(5), 1928-1939.

[Schowengerdt et. al., 2010] Schowengerdt, B. T., Murari, M., and Seibel, E. J. (2010). 44.1: Volumetric Display using Scanned Fiber Array. In SID Symposium Digest of Technical Papers (Vol. 41, No. 1, pp. 653-656). Oxford, UK: Blackwell Publishing Ltd.

[Khayatzadeh et. al., 2018] Khayatzadeh, R., Civitci, F., Ferhanoglu, O., and Urey, H. (2018). Scanning fiber microdisplay: design, implementation, and comparison to MEMS mirror-based scanning displays. Optics express, 26(5), 5576-5590.

[Jolly et.al., 2017] Jolly, S., Savidis, N., Datta, B., Smalley, D., and Bove Jr, V. M. (2017). Near-to-eye electroholography via guided-wave acousto-optics for augmented reality. In Practical Holography XXXI: Materials and Applications (Vol. 10127, p. 101270J). International Society for Optics and Photonics.

[Baran et. al., 2012] Baran, U., Brown, D., Holmstrom, S., Balma, D., Davis, W. O., Muralt, P., and Urey, H. (2012). Resonant PZT MEMS scanner for high-resolution displays. Journal of microelectromechanical systems, 21(6), 1303-1310.

[Banks et. al., 2006] Banks, L., Birch, M., Krueerke, D., Buckley, E., Cable, A., Lawrence, N., & Mash, P. (2006). 73.4: Real-time Diffractive Video Projector Employing Ferroelectric LCOS SLM. In SID Symposium Digest of Technical Papers (Vol. 37, No. 1, pp. 2018-2021). Oxford, UK: Blackwell Publishing Ltd.

[Zschau et. al., 2010] Zschau, E., Missbach, R., Schwerdtner, A., and Stolle, H. (2010). Generation, encoding, and presentation of content on holographic displays in real time. In Three-Dimensional Imaging, Visualization, and Display 2010 and Display Technologies and Applications for Defense, Security, and Avionics IV (Vol. 7690, p. 76900E). International Society for Optics and Photonics.

[Maimone et. al., 2017] Maimone, A., Georgiou, A., and Kollin, J. S. (2017). Holographic near-eye displays for virtual and augmented reality. ACM Transactions on Graphics (TOG), 36(4), 1-16.

[Kazempourradi et. al., 2019] Kazempourradi, S., Ulusoy, E., and Urey, H. (2019). Full-color computational holographic near-eye display. Journal of Information Display, 20(2), 45-59.

[Low et. al., 2003] Low, K.-L., Ilie, A., Welch, G., and Lastra, A. (2003). Combining Head-Mounted and Projector-Based Displays for Surgical Training, Proc. IEEE 10.1109/VR.2003 (2003).

[Amitai et. al., 1989] Amitai, Y., Friesem, A. and Weiss, V. (1989). Holographic elements with high efficiency and low aberrations for helmet displays," Appl. Opt. 28, 3405–3416.

[Ahrenberg et. al., 2008] Ahrenberg, L., Benzie, P., Magnor, M., and Watson, J. (2008). Computer generated holograms from three-dimensional meshes using an analytic light transport model. Applied Optics, 47(10):1567-1574.

[Akşit et. al., 2015] Akşit, K., Kautz, J., and Luebke, D. (2015). Slim near-eye display using pinhole aperture arrays. Applied Optics, 54(11):3422-3427.

[Bleha and Lei, 2013] Bleha, W. and Lei, L. (2013). Advances in liquid crystal on silicon (LCOS) spatial light modulator technology. In SPIE Defense, Security, and Sensing, pages 87360A-87360A. SPIE.

[Brooker and Brooker, 2003] Brooker, G. A. and Brooker, G. (2003). Modern classical optics, volume 8. Oxford University Press.

[Chellappan et. al., 2010] Chellappan, K., Erden, E., and Urey, H. (2010). Laser-based displays: a review. Applied Optics, 49(25): F79-F98.

[Cheng et. al., 2009] Cheng, D., Wang, Y., Hua, H., and Talha, M. (2009). Design of an optical see-through head-mounted display with a low f-number and large field of view using a freeform prism. Applied Optics, 48(14):2655-2668.

[Collings et. al., 2011] Collings, N., Davey, T., Christmas, J., Chu, D., and Crossland, B. (2011). The applications and technology of phase-only liquid crystal on silicon devices. Journal of Display Technology, 7(3):112-119.

[Deng and Chu, 2017] Deng, Y. and Chu, D. (2017). Coherence properties of different light sources and their effect on the image sharpness and speckle of holographic displays. Scientific reports, 7(1):5893.

[Eschbach, 1991] Eschbach, R. (1991). Comparison of error diffusion methods for computer-generated holograms. Applied optics, 30(26):3702-3710.

[Fienup, 1980] Fienup, J. R. (1980). Iterative method applied to image reconstruction and to computer-generated holograms. Optical Engineering, 19(3):193-297.

[Gao et. al., 2017] Gao, Q., Liu, J., Duan, X., Zhao, T., Li, X., and Liu, P. (2017). Compact see-through 3d head-mounted display based on wavefront modulation with holographic grating filter. Optics express, 25(7):8412-8424.

[Ghoushchi et. al., 2017] Ghoushchi, V. P., Aas, M., Ulusoy, E., and Urey, H. (2017). Effect of spatial coherence of led sources on image resolution in holographic displays. In Advances in Display Technologies VII, volume 10126, page 101260A. International Society for Optics and Photonics.

[Haussler et. al., 2008] Haussler, R., Schwerdtner, A., and Leister, N. (2008). Large holographic displays as an alternative to stereoscopic displays. Electronic Imaging, 5(11):68030-68034.

[Hessler et. al., 1998] Hessler, T., Rossi, M., Kunz, R. E., and Gale, M. T. (1998). Analysis and optimization of fabrication of continuous-relief diffractive optical elements. Applied Optics, 37(19):4069-4079.

[Hilaire et. al., 1995] Hilaire, P., Lucente, M., Sutter, J., Pappu, R., Sparrell, C., and Benton, S. (1995). Scaling up the MIT holographic video system. In Proc. SPIE vol. 2333, pages 374-380. SPIE.

[Hua and Javidi, 2014] Hua, H. and Javidi, B. (2014). A 3d integral imaging optical see-through head-mounted display. Optics Express, 22(11):13484-13491.

[Hua and Javidi, 2015] Hua, H. and Javidi, B. (2015). Augmented reality: Easy on the eyes. Optics and Photonics News, 26(2):26-33.

[Jang et. al., 2018] Jang, C., Bang, K., Li, G., and Lee, B. (2018). Holographic near-eye display with expanded eyebox. In SIGGRAPH Asia 2018 Technical Papers, page 195. ACM.

[Jang et. al., 2017] Jang, C., Bang, K., Moon, S., Kim, J., Lee, S., and Lee, B. (2017). Retinal 3d: augmented reality near-eye display via pupil-tracked light field projection on retina. In ACM Trans. Graph, pages 190-196. ACM.

[Jang et. al., 2016] Jang, C., Lee, C., Jeong, J., Li, G., Lee, S., Yeom, J., Hong, K., and Lee, B. (2016). Recent progress in see-through three-dimensional displays using holographic optical elements. Applied Optics, 55(3): A71-A85.

[Kang and Onural, 2010] Kang, F. Y. H. and Onural, L. (2010). State of the art in holographic displays: a survey. Journal of display technology, 6(10):443-454.

[Kazempourradi et. al., 2017] Kazempourradi, S., Ulusoy, E., and Urey, H. (2017). Fast computer-generated hologram computation using rendered depth map image. In Practical Holography XXXI: Materials and Applications, volume 10127, page 101270Q. International Society for Optics and Photonics.

[Kim et. al., 2008] Kim, H., Hahn, J., and Lee, B. (2008). Mathematical modeling of triangle-mesh modeled three-dimensional surface objects for digital holography. Applied Optics, 47(19): D117-D127.

[Kim et. al., 2017] Kim, N., Piao, Y., and Wu, H. (2017). Holographic optical elements and application, volume 1. InTech.

[Kim and Kim, 2008] Kim, S. and Kim, E. (2008). Effective generation of digital holograms of three-dimensional objects using a novel look-up table method. Applied Optics, 47(19): D55-D62.

[Kim et. al., 2012] Kim, S., Kim, J., and Kim, E. (2012). effective memory reduction of the novel look-up table with one-dimensional sub-principle fringe patterns in computer-generated holograms. Optics Express, 20(11):12021-12034.

[Kress and Starner, 2013] Kress, B. and Starner, T. (2013). A review of head-mounted displays (HMD) technologies and applications for consumer electronics. In SPIE Defense, Security, and Sensing, pages 87200A-87200A. International Society for Optics and Photonics.

[Levola, 2006] Levola, T. (2006). Diffractive optics for virtual reality displays. J. Soc. Inf. Disp., 14(5):467-475.

[Liu and Hua, 2009] Liu, S. and Hua, H. (2009). Time-multiplexed dual-focal plane head-mounted display with a liquid lens. Optics Letters, 34(11):1642-1644.

[Liu, 2011] Liu, Y. (2011). Fraunhofer computer-generated hologram for diffused 3D scene in Fresnel region. Optics Letter, 36(11):2128-2130.

[Lohmann et. al., 1996] Lohmann, A. W., Dorsch, R. G., Mendlovic, D., Zalevsky, Z., and Ferreira, C. (1996). Space-bandwidth product of optical signals and systems. JOSA A, 13(3):470-473.

[Lucente, 1993] Lucente, M. (1993). Interactive computation of holograms using a look-up table. J. Electron. Imag., 2(1):28-34.

[Maimone and Fuchs, 2013] Maimone, A. and Fuchs, H. (2013). Computational augmented reality eyeglasses. In Mixed and Augmented Reality (ISMAR), pages 29-38. IEEE.

[Maimone et. al., 2014] Maimone, A., Lanman, D., Rathinavel, K., Keller, K., Luebke, D., and Fuchs, H. (2014). Pinlight displays: wide _eld of view augmented reality eyeglasses using defocused point light sources. In ACM SIGGRAPH Emerging Technologies, page 20. ACM.

[Matsushima, 2005] Matsushima, K. (2005). Computer-generated holograms for three-dimensional surface objects with shade and texture. Applied Optics, 44(22):4607-4614.

[Matsushima et. al., 2003] Matsushima, K., Schimmel, H., and Wyrowski, F. (2003). Fast calculation method for optical diffraction on tilted planes by use of the angular spectrum of plane waves. J. Opt. Soc. Amer. A, 20(9):1755-1762.

[Matsushima and Takai, 2000] Matsushima, K. and Takai, M. (2000). Recurrence formulas for fast creation of synthetic three-dimensional holograms. Applied Optics, 39(35):6587-6594.

[Mengu et. al., 2016] Mengu, D., Ulusoy, E., and Urey, H. (2016). Non-iterative phase hologram computation for low speckle holographic image projection. Optics express, 24(5):4462-4476.

[Moon et. al., 2014] Moon, E., Myeongjae, K., Jinyoung, R., Kim, H., and Hahn, J. (2014). Holographic head-mounted display with RGB light emitting diode light source. Optics express, 22(6):6526-6534.

[Mori et. al., 2014] Mori, Y., Fukuoka, T., and Nomura, T. (2014). Speckle reduction in holographic projection by random pixel separation with time multiplexing. Applied optics, 53(35):8182-8188.

[Mukawa et. al., 2009] Mukawa, H., Akutsu, K., Matsumura, I., Nakano, S., Yoshida, T., Kuwahara, M., and Aiki, K. (2009). A full-color eyewear display using planar waveguides with reflection volume holograms. J. Soc. Inf. Disp., 17(3):185-193.

[Wang et. al., 2011] and Y. Wang, D. C., Hua, H., and Sasian, J. (2011). Design of a wide-angle, lightweight head-mounted display using free-form optics tiling. Optics Letters, 36(11):2098-2100.

[Ochiai et. al., 2017] Ochiai, Y., Otao, K., and Osone, H. (2017). Air mounted eyepiece: design methods for aerial optical functions of near-eye and see-through display using transmissive mirror device. arXiv preprint, page 1710.03889.

[Onural et. al., 1994] Onural, L., Bozdagi, G., and Atalar, A. (1994). New high-resolution display device for holographic three-dimensional video: Principles and simulations. Opt. Eng., 33(3):835-844.

[Pan, 2016] Pan, Y. (2016). A review of dynamic holographic three-dimensional display: Algorithms, devices, and systems. IEEE Transactions on Industrial Informatics, 12(4):1599-1610.

[Pan et. al., 2009] Pan, Y., Xu, X., Solanki, S., Liang, X., Tanjung, R. B. A., Tan, C., and Chong, T. C. (2009). Fast CGH computation using S-LUT on GPU. Optics Express, 17(21):18543-18555.

[Park, 2017] Park, J. H. (2017). Recent progress in computer-generated holography for three-dimensional scenes. Journal of Information Display, 18(1):1-12.

[Pedrotti et. al., 2017] Pedrotti, F., Pedrotti, L., and Pedrotti, L. (2017). Introduction to optics, volume 1. Cambridge University Press.

[Rolland et. al., 2016] Rolland, J. P., Thompson, K. P., Bauer, A., Urey, H., and Thomas, M. (2016). See-through head-worn display (HWD) architectures. Handbook of Visual Display Technology, pages 2929-2961.

[Sasaki et. al., 2014] Sasaki, H., Yamamoto, K., Wakunami, K., Ichihashi, Y., Oi, R., and Senoh, T. (2014). Large size three-dimensional video by electronic holography using multiple spatial light modulators. Scienti_c Reports, 4:30-35.

[Shi et. al., 2017] Shi, L., Huang, F.-C., Lopes, W., Matusik, W., and Luebke, D. (2017). Near-eye light field holographic rendering with spherical waves for wide field of view interactive 3d computer graphics. ACM Transactions on Graphics (TOG), 36(6):236.

[Shimobaba et. al., 2002] Shimobaba, T., Hishinuma, S., and Ito, T. (2002). Special purpose

computer for holography horn-4 with recurrence algorithm. Comput. Phys. Comm., 148(2):160-170.

[Smalley, 2006] Smalley, D. (2006). Integrated optics for holographic video, volume 1. M.S. thesis, Elect. Eng. Comput. Sci., Mass. Inst. Tech., Cambridge, MA, USA.

[Song et. al., 2018] Song, Y., Panas, R., and Hopkins, J. (2018). A review of micromirror arrays. Precis Eng., 51(1):729-761.

[Sweatt, 1977] Sweatt, W. (1977). Describing holographic optical elements as lenses. JOSA A, 67(6):803-808.

[Takaki and Yokouchi, 2011] Takaki, Y. and Yokouchi, M. (2011). Speckle-free and grayscale hologram reconstruction using time-multiplexing technique. Optics express, 19(8):7567-7579.

[Testorf and Lohmann, 2008] Testorf, M. and Lohmann, A. W. (2008). Holography in phase space. Applied optics, 47(4): A70-A77.

[Kuo et. al., 2020] Kuo, G., Waller, L., Ng, R., and Maimone, A. (2020). High resolution etendue expansion for holographic displays. ACM Transactions on Graphics (TOG), 39(4), 66.

[Thompson and Rolland, 2012] Thompson, K. and Rolland, J. (2012). Freeform optical surfaces: a revolution in imaging optical design. Optics and Photonics News, 23(6):30-35.

[Urey et. al., 2011] Urey, H., Chellappan, K., Erden, E., and Surman, P. (2011). State of the art in stereoscopic and autostereoscopic displays. Proceedings of the IEEE, 99(4):540-555.

[Wyrowski and Bryngdahl, 1988] Wyrowski, F. and Bryngdahl, O. (1988). Iterative Fourier-transform algorithm applied to computer holography. JOSA A, 5(7):1058-1065.

[Wyrowski and Bryngdahl, 1989] Wyrowski, F. and Bryngdahl, O. (1989). Speckle-free reconstruction in digital holography. JOSA A, 6(8):1171-1174.

[Yan et. al., 2004] Yan, J., Kowel, S., Cho, H., Ahn, C., Nordin, G., and Kulick, J. (2004). Autostereoscopic three-dimensional display based on a micromirror array. Applied Optics, 48(18):3686-3696.

[Yaras et. al., 2009] Yaras, F., Kang, H., and Onural, L. (2009). Real-time phase-only color holographic video display system using led illumination. Applied optics, 48(34): H48-H53.

[Yaras et. al., 2011] Yaras, F., Kang, H., and Onural, L. (2011). Circular holographic video display system. Optics Express, 19(10):9147-9156.

[Yeom et. al., 2015] Yeom, H., Kim, H., Kim, S., Zhang, H., Li, B., Ji, Y., Kim, S., and Park, J. (2015). 3D holographic head-mounted display using holographic optical elements with astigmatism aberration compensation. Optics Express, 23(35):32025-32034.

[Yoshikawa, 2001] Yoshikawa, H. (2001). Fast computation of Fresnel holograms employing difference. Opt. Rev., 8(5):331-335.

[Zhang et. al., 2014] Zhang, Z., Yu, Z., and Chu, D. (2014). Fundamentals of phase-only liquid crystal on silicon (lLCOS) devices. Light: Science & Applications, 3(10): e213.

[Zhou et. al., 2018] Zhou, P., Li, Y., Liu, S., and Su, Y. (2018). Compact design for optical-see-through holographic displays employing holographic optical elements. Optics Express, 26(3):22866-22876.

[Yaras et. al., 2010] Yaraş, F., Kang, H., and Onural, L. (2010). State of the art in holographic displays: a survey. Journal of display technology, 6(10), 443-454.

[Kazempourradi and Yaras et. al., 2019] Kazempourradi, S., Yaras, Y. S., Ulusoy, E., and Urey, H. (2019). Micro-mirror-array based off-axis flat lens for near-eye displays. Optics express, 27(11), 15172-15183.

[Takaki, 2011] Takaki, Y., and Yokouchi, M. (2011). Speckle-free and grayscale hologram reconstruction using time-multiplexing technique. Optics express, 19(8), 7567-7579.

[Horisaki et. al., 2018] Horisaki, R., Takagi, R., and Tanida, J. (2018). Deep-learning-generated holography. Applied optics, 57(14), 3859-3863.

[Peng et. al., 2020] Peng, Y., Choi, S., Padmanaban, N., Kim, J., and Wetzstein, G. (2020). Neural holography. In ACM SIGGRAPH 2020 Emerging Technologies (pp. 1-2).

[Eybposh et. al., 2020] Eybposh, M. H., Caira, N. W., Atisa, M., Chakravarthula, P., and Pégard, N. C. (2020). DeepCGH: 3D computer-generated holography using deep learning. Optics Express, 28(18), 26636-26650.

[Jiang et. al., 2019] Jiang, Q., Jin, G., and Cao, L. (2019). When metasurface meets hologram:

principle and advances. Advances in Optics and Photonics, 11(3), 518-576.

[Reichelt et. al., 2008] Reichelt, S., Haussler, R., Leister, N., Futterer, G., and Schwerdtner, A. (2008). Large holographic 3D displays for tomorrow's TV and monitors-solutions, challenges, and prospects. In LEOS 2008-21st Annual Meeting of the IEEE Lasers and Electro-Optics Society (pp. 194-195). IEEE.

[Stanley et. al., 2004] Stanley, M., Smith, M. A., Smith, A. P., Watson, P. J., Coomber, S. D., Cameron, C. D., ... and Wood, A. (2004). 3D electronic holography display system using a 100 mega-pixel spatial light modulator. In Optical Design and Engineering (Vol. 5249, pp. 297-308). International Society for Optics and Photonics.

[Kozacki et. al., 2012] Kozacki, T., Kujawińska, M., Finke, G., Hennelly, B., and Pandey, N. (2012). Extended viewing angle holographic display system with tilted SLMs in a circular configuration. Applied optics, 51(11), 1771-1780.

[Reicherter et. al., 1999] Reicherter, M., Haist, T., Wagemann, E. U., and Tiziani, H. J. (1999). Optical particle trapping with computer-generated holograms written on a liquid-crystal display. Optics Letters, 24(9), 608-610.

[Marquet et. al., 2005] Marquet, P., Rappaz, B., Magistretti, P. J., Cuche, E., Emery, Y., Colomb, T., and Depeursinge, C. (2005). Digital holographic microscopy: a noninvasive contrast imaging technique allowing quantitative visualization of living cells with subwavelength axial accuracy. Optics Letters, 30(5), 468-470.

[Sang et. al., 2011] Sang, X., Yu, C., Yu, M., and Hsu, D. (2011). Applications of digital holography to measurements and optical characterization. Optical Engineering, 50(9), 091311.

[Nobukawa et. al., 2015] Nobukawa, T., Wani, Y., and Nomura, T. (2015). Multiplexed recording with uncorrelated computer-generated reference patterns in coaxial holographic data storage. Optics Letters, 40(10), 2161-2164.

[Makowski et. al., 2009] Makowski, M., Sypek, M., Ducin, I., Fajst, A., Siemion, A., Suszek, J., and Kolodziejczyk, A. (2009). Experimental evaluation of a full-color compact lensless holographic display. Optics Express, 17(23), 20840-20846.

[Buckley, 2011] Buckley, E. (2011). Holographic laser projection. Journal of display technology, 7(3), 135-140.

[Buckley, 2010] Buckley, E. (2010). Holographic projector using one lens. Optics Letters, 35(20), 3399-3401.

[Slinger et. al., 2005] Slinger, C., Cameron, C., and Stanley, M. (2005). Computer-generated holography as a generic display technology. Computer, 38(8), 46-53.

[Dainty, 2013] Dainty, J. C. (Ed.). (2013). Laser speckle and related phenomena (Vol. 9). Springer Science and Business Media.

[Garcia et. al., 2005] Garcia, S. J., Ramírez, J. A. H., and Prieto, D. V. (2005). Reduction of speckle noise in digital holography by using digital image processing. Optik, 116(1), 44-48.

[Tziraki et. al., 2000] Tziraki, M., Jones, R., French, P. M. W., Melloch, M. R., and Nolte, D. D. (2000). Photorefractive holography for imaging through turbid media using low coherence light. Applied Physics B, 70(1), 151-154.

[Takano et. al., 2007] Takano, K., and Sato, K. (2007). Full-color electroholographic three-dimensional display system employing light emitting diodes in virtual image reconstruction. Optical Engineering, 46(9), 095801.